UC Berkeley
UC Berkeley Electronic Theses and Dissertations

Title
Molecular Simulations of Microporous Materials for Energy and Environmental Applications

Permalink
https://escholarship.org/uc/item/47j369w1

Author
Liu, Yifei

Publication Date
2019

Peer reviewed|Thesis/dissertation

eScholarship.org Powered by the California Digital Library
University of California

Molecular Simulations of Microporous Materials for Energy and Environmental Applications

by

Yifei Liu

A dissertation submitted in partial satisfaction of the

requirements for the degree of

Doctor of Philosophy

in

Chemical Engineering

in the

Graduate Division

of the

University of California, Berkeley

Committee in charge:

Professor Berend Smit, Chair
Professor Alexis T. Bell
Professor Phillip L. Geissler

Summer 2019

Molecular Simulations of Microporous Materials for Energy and Environmental Applications

Copyright 2019
by
Yifei Liu

Abstract

Molecular Simulations of Microporous Materials for Energy and Environmental Applications

by

Yifei Liu

Doctor of Philosophy in Chemical Engineering

University of California, Berkeley

Professor Berend Smit, Chair

Microporous materials are a diverse class of materials that includes porous carbons, zeolites, metal-organic frameworks (MOFs), and zeolite-templated carbons (ZTCs). These materials are characterized by a high surface area and diversity of pore geometry, as well as chemical tunability in MOFs, which provides a large design space for applications in gas storage and separations, catalysis, energy storage, sensing, and medicine.

The first chapter of this dissertation introduces microporous materials, their applications, and methods for studying them. In Chapter 2, I discuss a study that investigated the potential to tune the product distribution of the propene dimerization reaction via shape selectivity in MOFs and zeolites. We showed that the shape of the pore indeed exerts a large influence on the distribution of branched and linear products from propene dimerization. We demonstrated, moreover, that it is possible to predict the experimental linear conversion through the use of Monte Carlo simulations to compute the contribution of the heat of adsorption of the different products to their free energies of formation. Using this approach, we screened a library of MOFs and zeolites and identified materials which could further increase the linear conversion of propene dimerization beyond the highest-performing materials identified in the literature.

In the next chapter, Chapter 3, I detail our investigation into the adsorption of Δ^9-tetrahydrocannabinol (THC) in MOFs, in order to find a material that can be used in a THC breathalyzer. We tested two models of THC, one with only the bulky, rigid head group, and another describing the full molecule, including the flexible alkyl tail; we found that the simplified THC-head model is sufficient in most cases to rank the adsorption energy and Henry coefficient of materials. We also compare NVT and Widom insertion methods for computing the heat of adsorption of the materials, finding that in general the NVT method provides more statistically reliable values from shorter simulation times than Widom insertions. We introduced a novel method to evaluate the pore accessibility to nonspherical adsorbates, based on calculating the overlap area between the pore and an ellipsoidal probe molecule, and used this criterion to further narrow the pool of promising candidates. From

our screening, we identified three motifs promoting high THC adsorption, and highlight the highest-performing MOFs exhibiting these motifs. Finally, we computed the Henry coefficients of water in our materials and determined a selectivity threshold that would enable the detection of THC from humid breath.

In Chapter 4, I present results from reactive force field simulations of a set of amine-appended Mg_2(dobpdc) MOFs, which have shown promising performance for carbon capture. We studied the mobility of the the amine functional groups in the MOFs, and found that they undergo a hopping motion in which the ends of the amine swap their coordination bond with the metal center of the MOF. We computed the rates of amine hopping and the activation enthalpies and entropies of the transition, and found that it is possible to tune them by using functional groups with more or less steric hindrance at the amine ends, giving us insight into how different functional groups affect the step temperature and pressure of CO_2 adsorption.

In Chapter 5, I discuss the performance of ZTCs as the electrode material in an electrical-double layer capacitor (EDLC). We built EDLC simulation cells from a library of ZTC materials and investigated multiple equilibration protocols, determining that equilibrating with a constant-potential simulation is the most suitable choice. We then showed that the charging rate is strongly correlated with the pore size of the materials, which suggests that ion diffusion within the pores is the limiting process for electrode charging. Unlike the charging rate, the equilibrium capacitance of the materials was not clearly correlated to common geometric descriptors, but we found that it was strongly correlated to the charge compensation per carbon (CCpC), which indicates the efficiency of charge storage in the materials. In order to better understand the charge storage mechanisms in ZTCs, we examined the local charges and ion adsorption sites of individual pores in the materials, and identified characteristics of pores with higher and lower than average CCpC. We found that the CCpC is enhanced for adsorption sites near pockets with a small radius of curvature, and suggest this as a guideline for the design of improved EDLC electrode materials.

The final chapter concludes the dissertation and presents some perspectives on the outlook of these results.

To my parents,

Who have always encouraged me to ask questions.

Contents

Acknowledgments

I would like to express my gratitude to the people who mentored, supported, taught, inspired, and in every way bolstered me throughout the journey culminating in this thesis.

Above all, to my adviser, Berend Smit, thank you for expressing confidence in me from my first day in the group, for giving me the space and support to pursue my ideas, and for pushing me to do the best research I could do. I appreciate our honest conversations over the years, which have helped me tremendously to reflect and grow. Thank you also for fostering a supportive group environment and for providing the opportunity to experience doing research at both UC Berkeley and EPFL.

Thank you to the people with whom I collaborated during my PhD: Céline Merlet on supercapacitors, Daniele Ongari on THC sensing, and many people on CO_2 capture, including Jun Xu, Jeff Reimer, Jeff Long, and members of the Long and Reimer groups at Berkeley. I enjoyed and learned a great deal from the projects we worked on together.

To the members of my lab throughout the years, which includes Efrem Braun, Sudi Jawahery, Rocío Mercado, Katie Deeg, Matt Witman, Johanna Huck, Cory Simon, Sondre Schnell, Bess Vlaisavljevich, Yongjin Lee, Pete Boyd, Shachi Katira, Daniele Ongari, Mohamad Moosavi, Gloria Capano, Amber Mace, Senja Barthel, Leopold Talirz, Sasha Yakutovich, Özge Kadıoğlu, Andrés Ortega, Henglu Xu, Daiane Damasceno, and Zhi Li: It was a pleasure to have scientific discussions, go on hikes, have conversations both silly and serious, and generally share time together in Gilman Hall in Berkeley, at Energypolis in Sion, and all our travels in between.

A huge thank-you goes to Carlet Altamirano, Evelyn Ludi, Kim Eastman, and Kristin Stangl, without whose expert administrative abilities none of the past six years would have been possible. Thanks to Kelley McDonald and the whole team at NERSC for keeping the computers running smoothly.

Many people contributed indirectly to my progress in the PhD by helping me stay happy, healthy, and motivated. I want to express thanks to Alejandra and Yuram for helping me rediscover a love of music, and to Billy and Robbie for balancing research with trail runs and gym sessions. I would also like to thank Hilary Hahn, whose solo Bach records were an oft relied-upon source of inspiration and focus.

To my dear friends, Eudes, Sarah, Amaresh, Julia Y., Julia P., and Eric, thank you for being there to lend an ear, helping me put things in perspective, and lifting me up. Thanks also to my roommate and CBE cohort-mate Meron, for being someone I could always count on to help process the ups and downs of research.

To 妈妈, 爸爸, and Alex, thank you for your constant love, for making me laugh, for reminding me to rest, and for making sure my freezer is stocked with dumplings and 酱油肉 even when I live 5,000 miles away.

Finally, to Dirk, the best surprise of my PhD, thank you for teaching me to live in the moment and for making every day interesting. And especially for getting me outside on weekends so I wouldn't waste away during the final stretch of this PhD.

Chapter 1

Introduction

1.1 Microporous Materials

Microporous materials, which are defined by a pore size of less than 2 nm, are used in both research and industrial applications in chemical separations,[1–4] catalysis,[5,6] and energy storage.[7–12] They comprise a diverse group of materials, including zeolites, metal-organic frameworks, covalent organic frameworks, and porous carbons. These classes of materials are distinct in their synthesis methods and compositions, but are united by their small pore sizes, which are on the scale of many chemically and industrially important molecules, as well as their potential for large accessible surface areas.

Zeolites are naturally occuring aluminosilicate materials that were discovered in 1756.[13,14] Today, they are produced on an industrial scale, and are ubiquitous in catalysis and other industrial applications due to their chemical and thermal stability.[15] 234 distinct zeolite framework types have been classified as of 2019,[16] and the potential for chemical modifications such as ion exchange further increases the design space of such materials.

Metal-organic frameworks (MOFs) are a newer class of materials, first synthesized a few decades ago,[17,18] and comprise a three-dimensional network of metal centers (nodes) connected to organic linkers by coordination bonds. They are synthesized using reticular chemistry, in which molecular building blocks are assembled to form extended crystalline structures. Like other microporous materials, MOFs also have very high surface areas, with record Brunauer-Emmett-Teller (BET) surface areas of about $7000\,\mathrm{m\,g^{-2}}$ reported to date and hypothetical maximum surface areas predicted to be up to two times larger.[19] The design and synthesis of new MOFs has been a flourishing research area in the past few decades, and the development of more chemically stable MOFs has led to their increasingly widespread use in organic catalysis, gas separations, imaging, sensing, and proton, electron, and ion conduction.[20]

Zeolites and MOFs are both crystalline materials, which is a desirable characteristic as it means that composition and pore geometry are well-defined on a large scale. Other microporous materials which have short-range order but can be disordered on longer scales

include covalent organic frameworks (COFs),[21] which are also synthesized using reticular chemistry but are composed of organic nodes and linkers and are therefore fully covalently bonded, as well as zeolite-templated carbons (ZTCs).[22]

Reticular synthesis is modular in nature[17], yielding a virtually limitless design space for MOFs as different combinations of nodes and linkers can be used, which assemble in different topological nets. *Ca.* 70 000 MOFs have been synthesized to date, as reported on the Cambridge Crystallographic Structure Database (CCSD),[23] and thousands of new structures are reported each year. To add to this abundance of experimental structures, there exist libraries of hypothetical MOFs[24,25] which bring the total number of experimentally synthesized and hypothetical structures into the hundreds of thousands. In order to make this design space tractable, computational chemistry, and in particular molecular simulations, can be used to predict the properties of structures even before synthesis and identify promising structures for a particular application.[1,4,24,26] In this way, computation and experiment can work in tandem, with simulations "discovering" hypothetical materials *in silico* to inform and inspire experimental synthesis, and experimental results demonstrating new structures and unexpected properties to direct computational study. Achieving correspondence between experimental and theoretical results is not always straightforward, but has led to breakthroughs in material design and elucidation of mechanisms toward better understanding of material properties.

1.2 Energy and Environmental Applications

Microporous materials have great potential in technologies to decrease the energy needed for existing industrial processes, to mitigate the effects of increased anthropogenic emissions to the atmosphere through carbon capture and sequestration (CCS), and to provide more sustainable energy storage solutions.

For example, the amine-appended MOF *N,N'*-dimethylethylenediamine-Mg_2(dobpdc), was shown to exhibit a step-shaped CO_2 adsorption isotherm, which indicates potential for high deliverable capacity in a temperature- or pressure-swing adsorption process, with lower energy requirements than the currently used amine scrubbing technologies for CCS.[27] This step-shaped adsorption isotherm was shown to be due to a phase-change adsorption mechanism involving the amine functional groups.[28]

Another study synthesized a library of COFs *in silico* and screened them for methane storage applications, finding that one of the materials had better predicted methane deliverable capacity than any other reported structures.[29] Similarly, a screening study of the materials in the Nanoporous Materials Genome identified promising materials for hydrogen storage.[30]

Microporous materials are also used extensively in electrochemical energy storage applications as the electrode material for batteries and supercapacitors.[31] The field is dominated by carbon-based materials due to their affordability and conductivity,[32] though recently a

supercapacitor with electrodes made from a neat MOF (without the addition of conductive binders or additives) was demonstrated.[33]

1.3 Methods Used to Study Microporous Materials

This section describes the methods used in this dissertation to study microporous materials. The materials studied are all crystalline, and as such can be fully represented by three-dimensionally periodic unit cell containing the atom identities and positions. Interactions between the microporous material (often referred to as the "host") and additional adsorbate molecules (referred to as "guest" molecules) are described by a *force field*, and the phase space of such a system is explored using *molecular simulation methods*. I primarily discuss results of classical molecular simulation methods, in which chemical models describe systems at the resolution of atoms and molecules. This is in contrast to electronic structure methods such as density functional theory (DFT) or larger-scale continuum simulation methods.

1.3.1 Models and Force Fields

Classical models describe systems as a collection of sites interacting with each other through chemical bonds and non-bonded interactions. These interaction sites can either represent individual atoms, or a coarse-grained collection of atoms, such as an alkyl group. The sum of these interactions constitute the total energy of a system, which can be written generally as:

$$U_{total} = U_{bonded} + U_{nonbonded}\,, \tag{1.1}$$

where $U_{bonded} = U_{bonds} + U_{angles} + U_{torsions}$ and $U_{nonbonded} = U_{dispersion} + U_{electrostatics}$. A force field defines the potential energy of a system as a function of its atomic configuration by using a system of equations to define the contributions to U_{total}, and a set of constants, usually empirically derived, to parameterize these equations.

Considering first the bonded potentials, the energy of a bond with length r is typically described using a harmonic functional form:

$$U_r = \frac{k}{2}(r - r_0)^2\,, \tag{1.2}$$

with the Hookean spring constant k and equilibrium bond length r_0. Both k and r_0 are parameterized to a particular bond type. Similarly, angles can also be described using a harmonic potential, using a spring constant and equilibrium angle. More complicated functional forms for bonds and angles exist, and are sometimes more accurate for selected systems, but the versatility and computational efficiency of the harmonic bond and angle potential has made them the a common choice for many force fields. One notable exception is the Universal Force Field (UFF),[34] in which angle potentials are represented using the

general Fourier expansion,

$$U_\theta = K \sum_{n=0}^{m} C_n \cos n\theta \,, \tag{1.3}$$

which is often truncated as

$$U_\theta = K[1 + \cos(p\theta + \Psi)] \,, \tag{1.4}$$

where $p = \pi/(\pi - \theta_0)$ and $\Psi = \pi - p\theta_0$. Here θ_0 is the equilibrium angle.[34,35]

Torsional or dihedral angles are often described using a similar Fourier expansion truncation (with torsional barrier denoted V_ϕ and equilibrium torsional angle ϕ_0), yielding for example

$$U_\phi = \frac{1}{2} V_\phi [1 - \cos n\phi_0 \cos n\phi] \,. \tag{1.5}$$

We turn now to nonbonded potentials, which have contributions from van der Waals (dispersion) interactions and from electrostatics. The van der Waals interaction between two non-bonded atoms is usually described as the sum of a repulsive and an attractive term. The most common functional form is the Lennard-Jones potential,[36] which defines the interaction between two atoms i and j at a distance r_{ij} from each other as

$$U_{r_{ij}} = 4\epsilon \left[\left(\frac{\sigma_{ij}}{r_{ij}} \right)^{12} - \left(\frac{\sigma_{ij}}{r_{ij}} \right)^{6} \right] , \tag{1.6}$$

where the r^{-12} term represents short-range Pauli repulsion due to overlap of electron orbitals, and the r^{-6} term describes long-range dispersive attraction due to mutual induced dipole interactions. In the Lennard-Jones equation, ϵ_{ij} represents the "well depth" of the potential at the most favorable interatomic distance r_{ij}. Like the bonded terms, the Lennard-Jones functional form is semi-empirical, and while more complicated functional forms (such as the Buckingham potential) exist, they are not necessarily more accurate and are more computationally expensive.

Electrostatic interactions are the interactions between electric charges, and are described using Coulomb's law,

$$U_{r_{ij}} = \frac{q_i q_j}{4\pi\epsilon_0 r_{ij}} \,, \tag{1.7}$$

where q_i and q_j are the atomic partial charges and ϵ_0 is the dielectric constant in vacuum. Partial atomic charges of atoms are usually computed using higher-order accuracy electronic structure methods.

Though the equations that describe force fields are simple, when combined they represent a powerful tool that allows for simulation of large systems (up to tens of thousands of atoms) with relatively high accuracy. Several features of force fields lend themselves to computational efficiency: the first is that nonbonded interactions are pairwise, meaning that the nonbonded potential of a configuration of atoms can be computed by summing interactions between pairs of atoms. In addition, while the electronic density of atoms is spread over a nonzero volume, in classical force fields the electron density is usually treated as

a point charge. These features lead to several computational algorithms that allow for short-range cutoffs coupled with long-range corrections (tail corrections for dispersion interactions, and Ewald summation for electrostatics).

As mentioned throughout this overview of force fields, there are myriad ways to increase the complexity of classical force fields, for example by describing bonding implicitly using "reactive" force field methods that calculate bond order on the fly, or by using functional forms that involve more parameters to fit to a class of systems. With the increase of computational power in the last few decades, it is also possible to compute the potential energy of increasingly large configurations of atoms using electronic structure methods. However, due to the computational efficiency of classical simulations, it is likely that they will always enable simulations of larger and more complex systems compared to quantum mechanical methods, and thus classical force fields will remain relevant for a long time.

1.3.2 Molecular Simulation Methods*

With a force field in hand, we next want to calculate properties of interest for the system that we are studying. In the context of porous materials, these could be thermodynamic properties such as a heat of adsorption or the guest loading at a constant partial pressure, or dynamic properties such as a diffusion coefficient. We are usually interested in the average values of such properties at equilibrium, since these are the properties that are relevant in a bulk physical system. Thus we need a way to simulate these materials, in order to sample the phase space of the system in the ensemble of interest.

The points in this phase state are referred to as microscopic states, or microstates: the instantaneous configurations of a system. In order to fully define the microstate of a classical system, we would need to know the position and momenta of all of the particles in the system:

$$(r^N, p^N) = (\mathbf{r}_1, \mathbf{r}_2, ...\mathbf{r}_N; \mathbf{p}_1, \mathbf{p}_2, ...\mathbf{p}_N)\,, \tag{1.8}$$

When visiting these microstates, we constrain a select number of macroscopic variables. Macroscopic variables include the total number of molecules N, pressure p, volume V, energy E, and temperature T of a system. The collection of microscopic states corresponding to a set of constraints is referred to as an ensemble, and in a simulation we seek to compute *ensemble averages* of properties of interest. In order for this to work, we must ensure that our simulation, given enough time, will visit a representative sample of microscopic states in this ensemble.

We use two classes of simulation methods, *molecular dynamics* and *Monte Carlo*, which are summarized below.

*This section is based on Chapters 4, 5, and 6 of Frenkel, D. & Smit, B. *Understanding Molecular Simulation: From Algorithms to Applications* 2nd ed. (eds Frenkel, D., Klein, M., Parrinello, M. & Smit, B.) 280–282 (Academic Press: San Diego, 2001)

1.3.2.1 Molecular Dynamics

In molecular dynamics (MD) simulations, phase space is explored by numerically integrating Newton's second law of motion, using force fields to compute the forces acting on each atom. For a given particle i in a system, having position $\mathbf{r}_i$ and momentum $\mathbf{p}_i = m_i \times \mathbf{v}_i$, Newton's equation of motion for the force on the particle, F_i, can be written as:

$$F_i = m_i \frac{d^2\mathbf{r}_i}{dt^2} = \frac{d\mathbf{p}_i}{dt} \,. \tag{1.9}$$

F_i is computed as the sum of the pairwise forces f_{ij} exerted on particle i by all other particles j:

$$F_i = \sum_j f_{ij} = -\sum_j \nabla_i u_{ij} \,, \tag{1.10}$$

where u_{ij} is the contribution to the potential energy from the interaction between particles i and j and are computed using the force field.

Equations 1.9 and 1.10 are sufficient to describe the time-evolution of a closed system where the N, V, and E are fixed. In order to allow for exchange of either energy or volume (fixing T or p, rather than E or V), additional equations are needed.

Algorithms used to enforce temperature in a MD simulation are called *thermostats*. In a microscopic system, each degree of freedom α contributes to the average total kinetic energy of the system as

$$\left\langle \frac{1}{2} m v_\alpha^2 \right\rangle = \frac{1}{2} k_B T \,. \tag{1.11}$$

This serves as a definition of temperature in a MD simulation. The total number of degrees of freedom of a system is $N_f = 3N - 3$. Thus the instantaneous temperature of a system is defined as

$$T(t) = \sum_{i=1}^{N} \frac{m_i v_i^2(t)}{k_B N_f} \,. \tag{1.12}$$

Many thermostat schemes exist, such as velocity rescaling by a multiplicative factor to scale the total kinetic energy corresponding to the fixed temperature, coupling to a stochastic heat bath (the Andersen thermostat), and the most commonly used Nosé-Hoover thermostat, which uses an extended Lagrangian method to run deterministic MD at a constant temperature. Analogous methods for maintaining constant pressure, often also using extended Lagrangians, are referred to as barostats.

The accuracy of a MD simulation depends on judicious choice of algorithms and parameters for time integration and thermostatting and/or barostatting (when applicable). When computing properties from the simulation, care must also be taken to ensure that the simulation is fully equilibrated and that the production run is long enough to converge the quantities of interest.

The general algorithm of an MD simulation is as follows:

1. Generate a system and a starting configuration.
2. For each time step:
   a) Compute forces on the atoms in the system.
   b) numerically integrate the system forward in time.
   c) If the system is equilibrated, sample averages.

MD is useful for studying dynamic properties of systems, such as relaxation times and diffusion rates, as well as equilibrium thermodynamic properties such as the folded state of a protein or the average energy of a system. For example, in this dissertation, we use MD simulations in conjunction with a constant-potential method to compute the average charge stored by an EDLC at an applied voltage.

1.3.2.2 Monte Carlo

Like molecular dynamics, Monte Carlo (MC) methods provide a way to sample phase space in a given ensemble, by using a random walk to generate configurations within the ensemble, more heavily weighting the regions of phase space that contribute the most to the ensemble average. We ensure that we sample phase space with the appropriate probability distribution by choosing the acceptance criteria based on the potential energy surface of the system and the constrained macroscopic properties of the system.

Suppose that the probability of being in a particular state o is $\mathcal{N}(o)$. Then, the flow of states from state o to a new state n is this probability of being in state o, multiplied by the probability of generating the trial move $o \to n$ and the probability of accepting the trial move:

$$\mathcal{K}(o \to n) = \mathcal{N}(o) \times \alpha(o \to n) \times \mathrm{acc}(o \to n)\,. \tag{1.13}$$

While we do not know *a priori* the probabilities of being in a particular state of the system, we can compute the relative probabilities between states and use this to generate the correct acceptance criteria. This is done by imposing the condition of detailed balance, which specifies that the flow from one state to another must be equal to the flow in the opposite direction,

$$\mathcal{K}(o \to n) = \mathcal{K}(n \to o)\,. \tag{1.14}$$

By substituting Equation 1.13 and rearranging, we find:

$$\mathcal{N}(o) \times \alpha(o \to n) \times \mathrm{acc}(o \to n) = \mathcal{N}(n) \times \alpha(n \to o) \times \mathrm{acc}(n \to o) \tag{1.15}$$

$$\frac{\mathcal{N}(n)}{\mathcal{N}(o)} = \frac{\alpha(o \to n) \times \mathrm{acc}(o \to n)}{\alpha(n \to o) \times \mathrm{acc}(n \to o)} \tag{1.16}$$

In the canonical ensemble, the partition function is

$$Q(N,V,T) \equiv \frac{1}{\Lambda^{3N} N!} \int d\mathbf{r}^N \exp[-\beta \mathcal{U}(\mathbf{r}^N)] \,, \tag{1.17}$$

where Λ is the thermal de Broglie wavelength, and $\beta = 1/k_B T$. The probability of finding a configuration $\mathbf{r^N}$ is

$$\mathcal{N}(\mathbf{r}^N) = \frac{\exp[-\beta \mathcal{U}(\mathbf{r}^N)]}{Q} \,. \tag{1.18}$$

Combining this with Equation 1.16, we see that the relative probability of being in state o over state n is

$$\frac{\mathcal{N}(n)}{\mathcal{N}(o)} = \frac{\exp[-\beta \mathcal{U}(n)]}{\exp[-\beta \mathcal{U}(o)]} \,. \tag{1.19}$$

If we make the probability of generating a particular configuration constant, this means that the ratio of acceptance rules is

$$\frac{\mathrm{acc}(o \to n)}{\mathrm{acc}(n \to o)} = \exp -\beta[\mathcal{U}(n) - \mathcal{U}(o)] \tag{1.20}$$

This condition is satisfied by choosing the acceptance rule

$$\mathrm{acc}(o \to n) = \min(1, \exp -\beta[\mathcal{U}(n) - \mathcal{U}(o)]) \,. \tag{1.21}$$

In general, a statistical mechanical ensemble can be sampled by deriving the acceptance rules according to the correct partition function, and by specifying appropriate trial moves, for example, displacement moves for the canonical ensemble, and volume change moves for the NpT ensemble.

The Monte Carlo simulation therefore runs as follows:

1. Set up system and starting configuration
2. For each Monte Carlo cycle:
    a) Calculate the energy of the current configuration.
    b) Select a particle and apply a trial move.
    c) Accept or reject the move according to the acceptance criteria.
    d) Sample ensemble averages.

Ensemble averages can be sampled similarly to MD, with average values of adsorption energy or intermolecular distances computed over the course of a MC simulation. MC also provides a useful method to sample the density fluctuations of a system under a constant chemical potential, using the Widom particle insertion method. In this method, a "ghost" particle is inserted at a random position in the system, and the Boltzmann factor due to the additional interactions between this ghost particle and the system is used to calculate the excess chemical potential.

MC simulations are used in this dissertation to calculate adsorption energies and chemical potentials of adsorbate molecules.

1.4 Outline of Dissertation

This dissertation is organized into the following chapters:

Chapter 2 demonstrates the use of molecular simulations to predict the distribution of products arising from a propene dimerization reaction catalyzed in MOFs and zeolites, which yields both linear and branched C_6 isomers. We compute the contribution of the pore to the free energy of reaction using Monte Carlo simulations, and calculate the probability of formation of each of the products based on this free energy. The theoretical results are consistent with experimentally available data of rates of dimer branching in the zeolite Ni-Na-X and the MOFs Ni-MOF-74 and Ni-MOF-274. We then present the results of a screening to compute product distribution for the MOF-74 analogs and a database of experimental and hypothetical zeolites, showing how the concept of "shape selectivity" influences product distribution.

Chapter 3 presents a screening of MOFs from the computation-ready, experimental (CoRE) MOF database and MOF-74 analog library to find a material that can adsorb Δ^9-tetrahydrocannabinol (THC) for sensing by a breathalyzer. We use Monte Carlo simulations to compute the adsorption energy of THC using NVT ensemble simulations and Widom insertions, and show that, especially for a bulky molecule such as THC, average adsorption energies from NVT simulations are more statistically reliable than average properties from Widom insertions, for the same number of Monte Carlo cycles. We identify promising adsorption motifs for selective and favorable THC adsorption and compute adsorption selectivity with water.

Chapter 4 describes the use of reactive force fields for molecular simulation of the amine-appended Mg_2(dobpdc), a promising MOF for carbon capture. We use molecular dynamics simulations to study the dynamics of the amine functional groups, and identify the mechanism by which these functional groups break and re-form coordination bonds with the metal centers. By computing the rates of exchange at different temperatures we calculate the activation energies and enthalpies for a series of amine analogs, showing that the dynamics can be influenced by changing the amount of steric hindrance experienced by the amine due to its end groups. These insights can be used to tune the step temperature or pressure of CO_2 adsorption.

Chapter 5 presents simulations of electrical double-layer capacitors (EDLCs) that use zeolite-templated carbons (ZTCs) as the electrode material. We describe a procedure to build a two-electrode EDLC simulation cell from a given ZTC structure, solvate the electrodes with [BMI^+][BF_4^-]/[ACN] electrolyte, and equilibrate the EDLC at constant potential. We show that the charging dynamics of the electrodes are correlated with the pore sizes of the ZTCs. Comparing the equilibrium capacitances of the ZTCs, we elucidate how certain pore characteristics affect charge storage efficiency, using the descriptor charge compensation per carbon (CCpC) introduced in our work. We find

that the radius of curvature of a pore strongly influences its local charge storage efficiency, with smaller curvature radii corresponding to more charge stored and therefore higher capacitance.

Chapter 6 concludes the dissertation with a summary and outlook.

Chapter 2

Product Distribution of Propene Dimerization*

2.1 Shape Selectivity for Propene Dimerization Catalysis

The vast design space of MOFs has attracted attention from the catalysis community, where the tunability of pore shape and chemical functionality enables the design of new and improved catalysts. Though MOFs are not guaranteed the stability afforded by zeolites, the industrial standard for catalysis applications, recent years have seen the synthesis of frameworks which have high chemical and thermal stability and accessible metal sites that can serve as highly selective active sites for reactions.[5,39–41]

For example, the MOF-74 class of materials, which features coordinatively unsaturated metal sites, has shown promise in catalyzing the dimerization of propene to C_6 olefins with relatively high selectivity and activity for valuable linear products: 1-hexene is a feedstock for polyethylene and its linear regioisomers are used to produce lubricants and detergents.[42] Supported nickel catalysts are typically preferred for propene dimerization and other olefin oligomerization reactions,[42–44] but there is often a tradeoff between catalytic activity and selectivity for the desired products: Mlinar *et al.* showed via tuning the free volume of a Ni-Na-X zeolite that the most constricted pores had the highest fraction of linear isomer products, but the lowest catalytic activity. Correspondingly, increasing the pore space led to higher activity but loss of selectivity toward linear isomers.[45] Subsequent work has shown that Ni_2(dobdc) (Ni-MOF-74) and and its expanded-linker analog Ni_2(dobpdc) (Ni-MOF-274) can achieve high linear selectivity while maintaining high catalytic activity.[46] By analyzing the product distribution of propene oligomerization in the MOFs, Ni-Na-X, and Ni-loaded MCM-31, Mlinar *et al.* showed that both MOF-74 materials had approximately 10% less

*This chapter is based on Liu, Y. M. & Smit, B. Predicting Product Distribution of Propene Dimerization in Nanoporous Materials. *ACS Catal.* **7,** 3940–3948. http://pubs.acs.org/doi/abs/10.1021/acscatal.7b00712 (June 2017).

dimer branching than the zeolite and mesoporous materials. The lower dimer branching and corresponding higher linear selectivity in MOFs was hypothesized to be due to increased steric hindrance around the Ni^{2+} active sites in the MOFs, which favors the transition state for the linear dimer.[46]

The phenomena governing reaction product distributions encompass a wide range of time and length scales, from the localized and short-lived transition state, to adsorption inside an individual pore and product diffusion out of the porous material. An important difference of reactions in nanopores is that, unlike reactions in liquid or gas phase, the thermodynamics of the reaction is not known. In particular, we lack information on the contribution of the MOF or zeolite to the free energy of formation. Molecular simulations can compensate for this missing information and can help us, for example, quantify the extent to which the pores favor or disfavor the products that can form. Insights gained from molecular simulations can also provide an atomistic perspective on features such as pore shape and composition in order to better understand how these descriptors influence product distribution and possibly even predict higher-performing candidate materials for propene dimerization and other oligomerization reactions.[47,48]

Expanding on the foundational ideas of shape selectivity, we show in this work how the product distribution can be tuned as a function of pore size, shape, and composition. We used molecular simulations to compute the contribution of different porous materials to the free energy of formation of the C_6 olefin isomers. We consider the MOF Ni-MOF-74 and the zeolite Ni-Na-X in the Mlinar study,[46] as well as synthesized and hypothetical zeolites and hypothetical MOF-74 analogs, for a total of 118 materials. Where experimental results are available, we show that our computational predictions for linear selectivity agree well with experiment. One of the questions we sought to address, for example, is how the linker structure in Ni-MOF-74 influences the free energy of formation, prompting us to study the MOF-74 analog materials generated by Witman *et al.*[25] Similar considerations motivated our choice of additional existing and hypothetical zeolite materials.[16,49] Of particular importance in this work is the presence of coordinatively unsaturated metal sites in the MOF-74 analogs. These "open" metal sites can engage in π complexation with the double bond of the olefins, causing enrichment of olefin adsorption.[50] We demonstrate that the presence of open metal sites complements the shape-selective effects of pore geometry in determining reaction product distribution.

2.2 Methods for Simulation of Product Distribution

2.2.1 Adsorbate and Adsorbent Models

To compute the free energy of formation of the different isomers in each porous material we used models that describe the equilibrium interactions between the adsorbates and the adsorbent materials. Parameters for both bonded and van der Waals interactions for the dimer

isomers were taken from the TraPPE united atom force field, which has been demonstrated to reproduce well experimental hydrocarbon isotherms in porous materials.[51]

Nonbonded parameters for Ni_2(dobdc) and Ni_2(dobpdc) were taken from the Dreiding force field,[52] with the exception of the metal atoms for which parameters were taken from UFF.[53] Charges for these MOFs were calculated using the REPEAT method[54] with electrostatic potentials computed using DFT.[55] MOF-74 analog nonbonded parameters and charges were calculated by Witman *et al.*[25]

Zeolite-adsorbate interactions were described using modified alkene-zeolite parameters in Liu *et al.*[56] In order to capture the preferential interaction between the MOF open metal sites and the olefin double bonds, the double bond was described by a three-point charge model ($q_{CHx} = 0.85\ e$ and $q_{COM} = -1.70\ e$)[57] which has been shown to reproduce the experimental adsorption isotherm for ethene in an open-metal site MOF.[58] For all other guest-adsorbate interactions, Lorentz-Berthelot mixing rules were used to compute Lennard-Jones interaction parameters.

2.2.2 Computing Product Distribution

We consider the product distribution to comprise the 12 experimentally detected isomers shown in Table 2.1.[46] We are interested in predicting the fraction of linear isomers x_l in the product distribution arising from the different porous materials. The first step in any study of product distribution is normally the free energy of formation. As this free energy is not known experimentally, we use molecular simulations to gain insight to how the pores influence the product distribution by considering the pore's contribution to the free energy of formation. Each product isomer, once formed, must spend time adsorbed inside the material before diffusing out. Therefore the free energy of formation inside the pore can be expressed for product isomer i as:

$$\Delta G_{form,i} = \Delta G_{form,gas,i} + \Delta G_{ads,i} - \Delta G_{ads,reac}\,. \tag{2.1}$$

Note that for all product isomers, $\Delta G_{ads,reac}$ is the same as it refers to adsorption of two reactant propene molecules, so the dominant influence of the pore on the product distribution is captured by the free energies of adsorption of the product isomers, $\Delta G_{ads,i}$.

At this point it is important to note that thermodynamics is not the only factor that determines product distribution. Kinetics can also play a role, but even in a kinetically controlled reaction, if the transition state resembles the product state then the contribution of the pores to the free energy of formation can be of use, *i.e.*, assuming that for this system the Brønsted-Evans-Polanyi relation holds.[59] Without knowing the precise mechanism of reaction, we can quantify the probability of formation of a particular isomer i as

$$p_i \propto \exp\left(-\beta \Delta G_{ads,i}\right) \tag{2.2}$$

Table 2.1: Propene dimer isomers considered in this work

Isomer	Abbreviation	Structure
1-hexene	1h	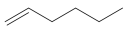
trans-2-hexene	t2h	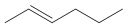
cis-2-hexene	c2h	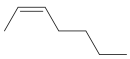
trans-3-hexene	t3h	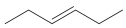
cis-3-hexene	c3h	
2-methyl-2-pentene	2m2p	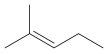
cis-3-methyl-2-pentene	c3m2p	
4-methyl-1-pentene	4m1p	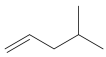
cis-4-methyl-2-pentene	c4m2p	
trans-4-methyl-2-pentene	t4m2p	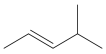
2,3-methyl-1-butene	23m1b	
2-methyl-1-pentene	2m1p	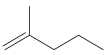

by assuming that the reaction is rate-limited, which is likely given the small reactor size,[46] and that the transition state resembles the product molecule.

The standard free energy of adsorption, ΔG_{ads} was calculated as

$$\Delta G_{ads} = G_{ex} - G_{ex}^{gas}\,, \tag{2.3}$$

where excess free energies of the dimer isomers at infinite dilution inside the frameworks were computed via Widom insertions to get the Henry coefficient:[37]

$$k_H = \beta \frac{\langle W_H \rangle}{\langle W_{IG} \rangle}\,, \tag{2.4}$$

where $\langle W_{IG} \rangle$ is the ideal-gas Widom Rosenbluth weight, computed via a separate simulation in an empty box. From the Henry coefficient, the excess chemical potential μ_{ex} was calculated using

$$k_H = \beta \exp\left(-\beta \mu_{ex}\right). \tag{2.5}$$

For a single molecule at infinite dilution $\mu_{ex} = G_{ex}$. $\mu_{ex}^{gas} = G_{ex}^{gas}$ was also computed via Widom insertions in the gas phase.

Internal energies of adsorption were computed by using the Boltzmann-weighted average energy from Widom insertion, $\langle U \rangle_W$, and then subtracting the ideal gas intra-molecular energy calculated from NVT simulation:

$$\Delta U_{ads} = \langle U \rangle_W - \langle U_{IG} \rangle. \tag{2.6}$$

From these values the enthalpy and entropy of adsorption could be calculated using relations from classical thermodynamics.

Monte Carlo simulations were conducted with the RASPA molecular simulation package.[60] Simulations were conducted at 450 K, the operating temperature of the propene dimerization reaction. At least 1 000 000 MC cycles were used to ensure convergence of the Henry coefficients. Adsorption sites were visualized using the VisIt package.[61]

2.3 Structure Database for Product Distribution Screening

Since our simulations are at equilibrium conditions, we chose chemical structures which would be representative of the equilibrium environment felt by the product olefin isomers. Zeolite structures are therefore represented in our simulations without Ni sites, as the loading of Ni in Ni-Na-X is less than 0.6 wt%, compared with 37.7 wt% in Ni-MOF-74.[46] In addition, with the exception of Ni-MOF-74, metal-organic frameworks containing Mg rather than Ni as the metal site are used since structures and parameters have been generated for a large set of Mg-based MOF-74 isostructural analogs,[25] and we find that changing the metal has little effect on the equilibrium properties of the material (Figure 2.2). The 118 total porous materials considered in this study are summarized in Table 2.2 and Figures 2.1.

2.4 Thermodynamic Factors Influencing Product Distribution

2.4.1 Free Energy Profiles

The striking observation that motivated this work is the enhanced linear conversion of Ni-MOF-74 and Ni-MOF-274 compared to Ni-Na-X in the work of Mlinar *et al.* They showed via fixed-bed reactor experiments that Ni-MOF-74 and Ni-MOF-274 had a lower degree of

Table 2.2: Materials Screened

Material class	Count
MOF-74	3[a]
Hypothetical MOF-74 analogs	63[b]
Zeolites	23[c]
Hypothetical zeolites	29[d]

[a] M_2(dobdc) [M=Ni,Mg],[62] Mg_2(dobpdc)[63]; [b] MOF-74 analogs assembled by Witman *et al.*[25,64]; [c] selected from IZA database with range of pore sizes[16]; [d] all 1D channel topology.[49]

dimer branching than the zeolite Ni-Na-X, while Ni-MOF-74 and Ni-MOF-274 had a similar degree of dimer branching of approximately 38%.[46] In a homogeneous reaction, one would begin a study of the product distribution by comparing the free energies of formation of the products. For a reaction in a porous material, however, this thermodynamic information is not known. The product distribution may be influenced by many mechanisms, including thermodynamics, kinetics, and diffusive processes. However, if the enhancement of linear conversion in the MOFs is governed by free energy of formation, then we should be able to see a more favorable free energy of linear isomers in the MOFs reflected in our calculations.

The ΔG_{ads} computed for the five linear and seven branched olefin isomers (Table 2.1) are shown in Figure 2.2 for Ni-MOF-74, Mg-MOF-74, Mg-MOF-274, and FAU zeolite, relative to the ΔG_{ads} of 1-hexene. This "free energy profile" represents the degree to which the porous material stabilizes the formation of each isomer. An important result is that this figure shows the free energy profiles are qualitatively different between the three MOF structures and FAU zeolite. In the MOFs, the linear isomers are, on the whole, more stabilized than the branched isomers, with the exception of cis-3-hexene in Mg-MOF-274. The free energy profile of the MOFs is virtually the inverse of that of FAU, where, with the exception of trans-2-hexene and trans-3-hexene, the linear isomers have much higher ΔG_{ads} than the branched isomers. The free energy profiles MOFs in Figure 2.2 look similar to each other, indeed the root-mean-square error between the Ni-MOF-74 and Mg-MOF-74 (Mg-MOF-274) is only 0.12 (0.28) kJ mol^{-1}, compared to 2.22 kJ mol^{-1} between Ni-MOF-74 and FAU, indicating that the identity of the metal does not influence the equilibrium free energy of the isomers. Overall, these findings are consistent with the results of the experimental study of Mlinar *et al.*, giving us confidence that our approach is reasonable and can be applied to other materials that may be promising for this reaction.

The contrast in free energy landscapes of the metal-organic and zeolitic materials has its source primarily in differences in the enthalpy of adsorption. Figure 2.3 shows ΔH_{ads} and ΔS_{ads} of FAU and Ni-MOF-74. The enthalpy profile of FAU looks qualitatively similar to its free energy profile; branched products have, on average, more favorable enthalpies of adsorption compared to linear products. The same qualitative agreement holds for Ni-MOF-74. However, for the entropic contribution, the qualitative trends are different. Adsorption

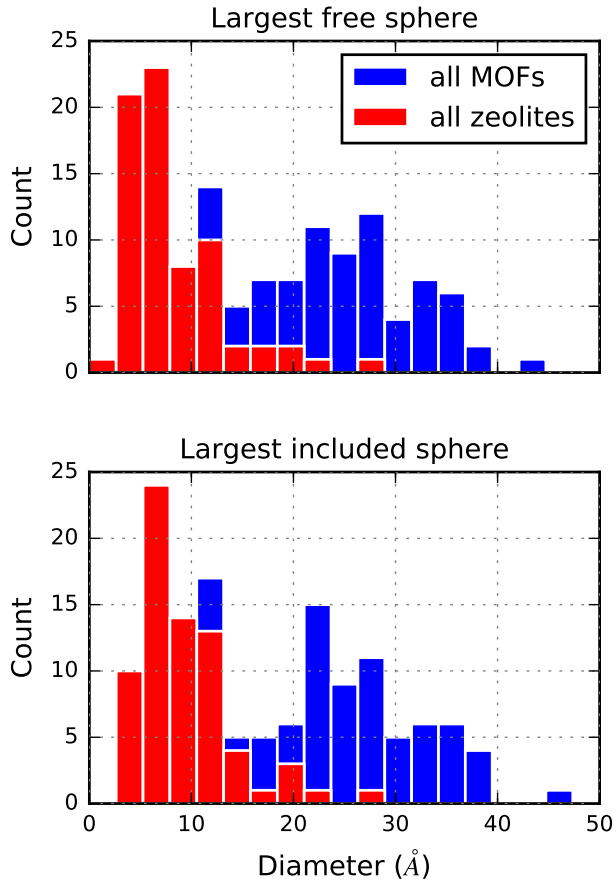

Figure 2.1: Geometric pore descriptors summary. Channel diameter is gauged by the largest free sphere diameter, d_{free}, the size of the largest probe sphere able to freely percolate through the material.

of branched products is more entropically favored in Ni-MOF-74 and FAU does not display a clear entropic preference toward adsorption of either group. The trends in entropy of adsorption can be attributed to the larger configurational space of the linear molecules in the gas phase, which means that, once adsorbed, they lose more entropy than their branched, more rigid, counterparts. Enthalpically, the flexiblity of the linear isomers allows them to adopt an energetically favorable configuration with the π bond closer to the open metal sites in the MOF, whereas FAU has no such favorable adsorption sites.

2.4.2 Linear Conversion: Comparison of Selected Materials with Experimental Results

We wish to identify materials which can selectively convert propene to linear C_6 olefins. We quantify this selectivity by calculating the total fraction of linear isomers in the product

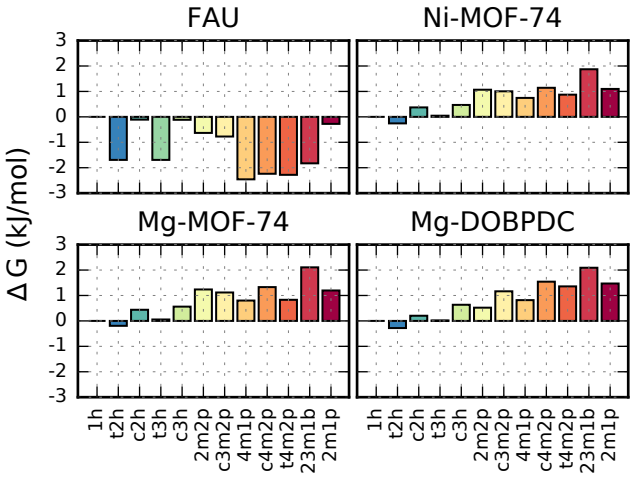

Figure 2.2: Free energy profile of adsorbates in porous frameworks, relative to 1-hexene.

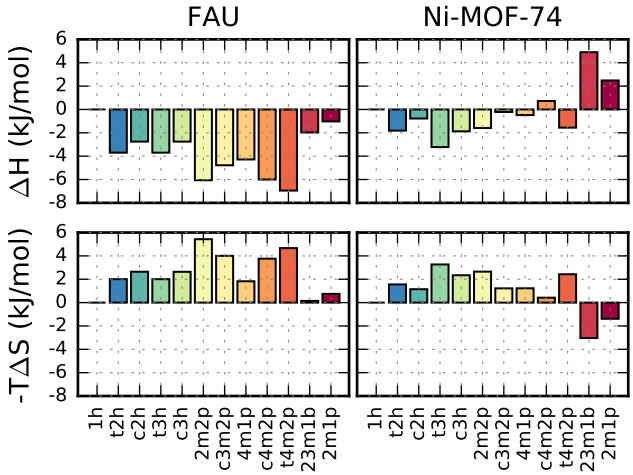

Figure 2.3: Enthalpic (ΔH) and entropic (-TΔS) contributions to the free energy profile, relative to 1-hexene.

mixture predicted by molecular simulation. Making use of Equation 2.2 for the probability of formation of a particular isomer p_i, we define the linear conversion $x_L = \sum_{linear} p_i$. Therefore,

$$x_L = \frac{\sum_{linear} \exp\left(-\beta \Delta G_{i,ads}\right)}{\sum_{all} \exp\left(-\beta \Delta G_{i,ads}\right)} . \tag{2.7}$$

Linear conversion x_L thus calculated is shown for Ni-MOF-74, Mg-MOF-74, Mg-MOF-274, and FAU in Figure 2.4. The linear conversions for the MOF materials are close in

value, while the linear conversion of FAU is approximately 10.0% lower. This agrees with the observation from the previously calculated free energy profiles that the MOFs favor adsorption of linear isomers to a larger degree than branched isomers.

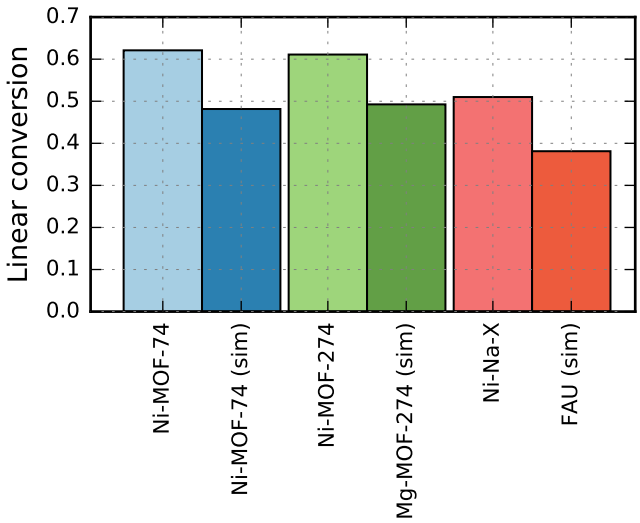

Figure 2.4: Fraction of linear dimer isomers in product distribution, experimental and simulated. Experimental values are taken from Mlinar *et al.*[46]

The 10.0% enhancement in linear conversion of Ni-MOF-74 relative to FAU is in good agreement with the 11.1% enhancement observed experimentally by Mlinar *et al.*,[46] suggesting that our model and theoretical framework capture quantitatively the influence of the adsorbent material on product distribution. Interestingly, the absolute predicted linear conversions are 13.0% lower than their respective experimental values. This means the experimental materials are consistently more selective towards linear isomers than their simulated counterparts. This could be due to diffusive barriers not accounted for by our simulations, which would favor the less-bulky linear isomers. We also want to emphasize that these calculations rely on equilibrium thermodynamics, and thus presume that Brønsted-Evans-Polanyi conditions are met.

From this comparison with the experimental results of Mlinar *et al.*, we can conclude that the contribution of the pores to the free energy of formation is indeed a useful indicator of how the product distribution varies with the catalyst material. It is therefore interesting to explore how this distribution can be further changed by using a different zeolite MOF structure. Expanding the database of structures allows us to better understand how molecular descriptors correlate with product distribution, and further elucidate design principles of materials for propene dimerization.

2.4.3 Extension to Other Frameworks and Understanding Thermodynamic Factors Influencing Linear Selectivity

A wide variety of pore geometries exists among crystalline, microporous materials. Differences in local structure around a particular adsorption site, as well as the global topology of the material, influence the relative adsorption free energies within a set of adsorbate molecules. Most of the frameworks in this study have one-dimensional channel topologies so that we could use the channel diameter as a quantitative metric for comparison between materials, and compare these materials to the MOF-74 class of materials, which have high experimentally observed linear selectivity.

The linear conversions computed for these materials in this study are shown in Figure 2.5 plotted against largest free sphere diameter (d_{free}). The zeolite materials, both hypothetical and synthesized, show sensitivity to d_{free} below 10 Å, and above this threshold diameter the linear conversion remains virtually constant. Below $d_{free} = 10$ Å the linear conversion varies non-monotonically with pore size. At intermediate diameters the materials favor branched dimer isomers, and there is a local minimum in linear conversion at a diamter of roughly 7.5 Å. From diameters of 7.5 Å decreasing to 5 Å the linear conversion increases, reaching almost 80%. Below 5 Å there is no clear correlation between linear conversion and pore size; instead there is a wide spread in predicted product distributions, likely because these small pore diameters approach the average size of a C_6 olefin isomer and small changes in local pore geometry can cause some C_6 olefin isomers to be extremely disfavored.

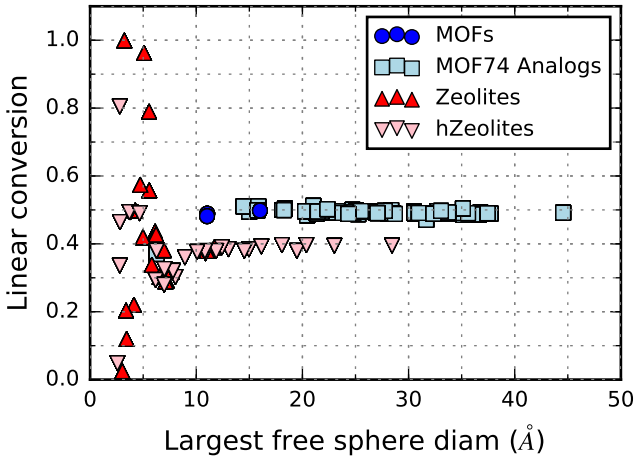

Figure 2.5: Fraction of linear dimer isomers in product distribution vs. largest free sphere diameter for zeolites and MOFs.

There are a few zeolites which achieve close to full conversion (APD, 99%, and ATO, 96%) and zero linear conversion (EDI, 2.5%, and h8186492, 4.8%). Their structures shown in Figure 2.6. Their pores provide particularly favorable adsorption sites for 1-hexene, cis-2-hexene, and cis-3-hexene, which are able to coil into the small channels without incurring

too much steric penalty, in order to take advantage of the enthalpic reward of binding in a tight pocket. In APD (ATO), ΔH_{ads} of these three linear isomers is on average 19 kJ mol^{-1} (5.5 kJ mol^{-1}) more favorable than the next closest isomer's ΔH_{ads}.

For EDI and h8186492 zeolites the product distributions are heavily dominated by a single branched isomer: 2,3-methyl-1-butene in EDI and cis-4-methyl-2-pentene in h8186492, which respectively account for 87% and 88% of total product distribution. These branched isomers are inherently more configurationally constrained, so we attribute their comparatively low ΔH_{ads} to a fortuitous binding pocket that complements the isomer structure. These examples demonstrate that frameworks whose pore sizes approach the size of the product molecules can be highly selective toward a particular product or group of products, with very different selectivities even among structures with comparable geometric descriptors.

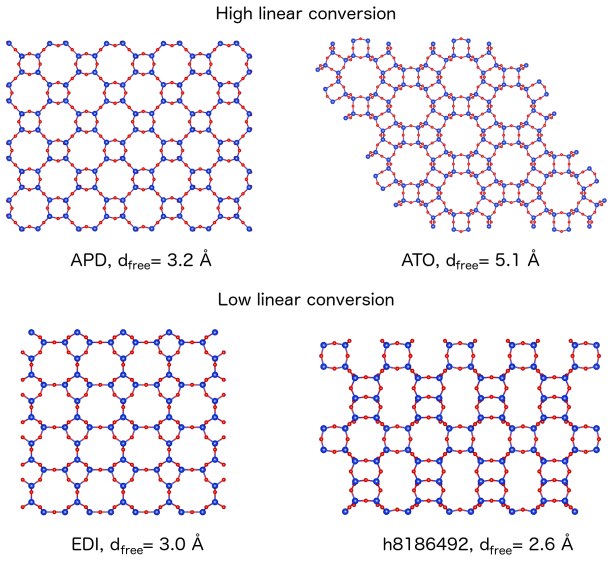

Figure 2.6: Zeolites achieving close to 100% and 0% linear conversion.

Like the zeolites, Ni-MOF-74 and its isostructural analogs also have approximately constant linear conversion above 10 Å. Surprisingly, however, the linear conversion is shifted 10–13% higher, resulting in all of the MOFs with $d_{free} > 10$ Å having significantly enhanced linear conversion compared to the zeolites within the same range. 11 of the MOF-74 analogs have equal or higher linear conversion than Mg-MOF-274, the highest-performing previously synthesized MOF, with the best analog having a predicted 1.5% increase in linear conversion over Mg-MOF-274 (Figure 2.7). As there is only one published MOF-74 analog structure smaller than 10 Å, Mg_2(DHFUMA),[64] it is not possible to determine the composition-independent effect of pore diameter below 10 Å. However, the linear conversion of Mg_2(DHFUMA) falls within the range of the linear conversion among zeolites of the same pore size, suggesting that for small pore sizes, the physical amount of pore space available to adsorbates dominates their relative free energies of adsorption.

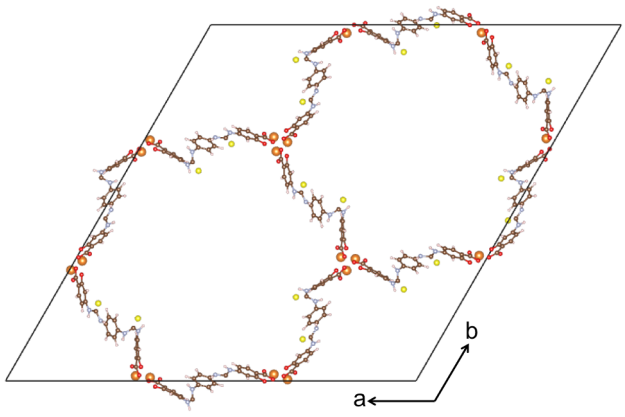

Figure 2.7: MOF-74 analog (structure name: 184x1_all_conf_10850_1,[25] $d_{free} = 21.0\,\text{Å}$) with 1.5% higher linear conversion than Mg-MOF-274, the best-performing previously synthesized MOF.

Since the linear conversion is a function of the relative free energies of adsorption of linear and branched isomers, further insights can be gleaned by examining the enthalpic and entropic contributions to these free energies in Figure 2.8. Both ΔH_{ads} and ΔS_{ads} for each isomer depend very strongly on pore size, with a range of ΔH_{ads} and ΔS_{ads} for different isomers inside the same material. ΔH_{ads} is very repulsive for small pore sizes, reaches a minimum around $d_{free} = 5\,\text{Å}$, the median end-to-end distance of the product isomers, and levels off for larger pore sizes. ΔS_{ads} is more monotonic, decreasing sharply for decreasing $d_{free} < 7.5\,\text{Å}$ but also remaining relatively constant for larger pore sizes.

While all of the materials appear to have the same average dependence of ΔH_{ads} and ΔS_{ads} on pore size, the difference between the highest and lowest ΔH_{ads} and ΔS_{ads} within a single material appears to be slightly larger for the MOFs than for the zeolites, indicating that the MOFs differentiate more between the product isomers than do the zeolites. To investigate this spread, we define the properties $\Delta\Delta H_{ads}$ and $\Delta\Delta S_{ads}$, where $\Delta\Delta M_{ads} \equiv \langle \Delta M_{ads} \rangle_{linear} - \langle \Delta M_{ads} \rangle_{branched}$ for $M = \{S, H\}$. More negative $\Delta\Delta H_{ads}$ indicates enthalpic preference for linear isomers to adsorb in MOFs than in zeolites, while entropic preference is greater for more positive $\Delta\Delta S_{ads}$. In Figure 2.8, $\Delta\Delta H_{ads}$ shows large variations for small pore sizes, indicating that the relative binding energies of linear and branched isomers is very sensitive to pore shape for small pores. For larger pore sizes of $d_{free} > 10\,\text{Å}$, the $\Delta\Delta H_{ads}$ of the MOFs and MOF-74 analogs are consistently $3\,\text{kJ mol}^{-1}$–$5\,\text{kJ mol}^{-1}$ lower than that of zeolite materials, indicating that MOFs enthalpically favor linear isomers. By contrast, from the analogous $\Delta\Delta S_{ads}$ plot the MOFs appear to entropically favor the branched isomers. Overall, the $\Delta\Delta H_{ads}$ exerts the dominant influence on linear conversion (Figure 2.9), and the enhanced linear conversion of MOFs can be attributed to enthalpic effects that selectively favor adsorption of linear isomers.

This suggests that specific chemical interactions can enhance the influence of pore shape

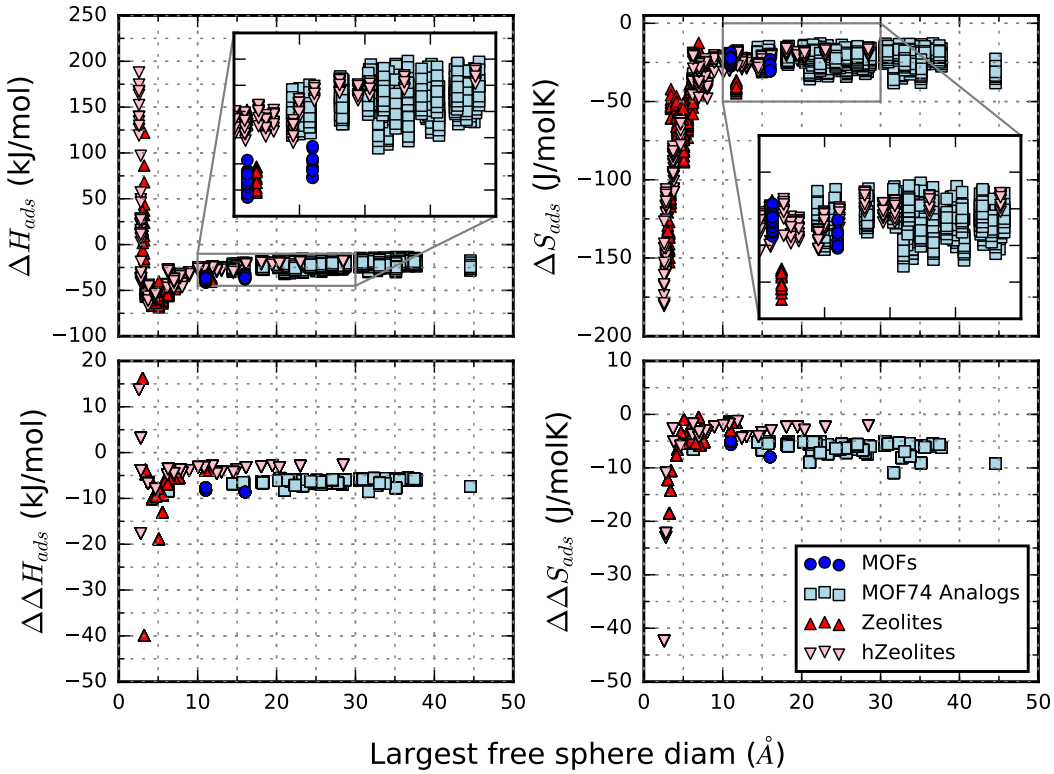

Figure 2.8: ΔH_{ads} and ΔS_{ads} of all components (upper); $\Delta\Delta H_{ads}$ and $\Delta\Delta S_{ads}$ (lower). $\Delta\Delta M_{ads} \equiv \langle \Delta M_{ads} \rangle_{linear} - \langle \Delta M_{ads} \rangle_{branched}$ for $M = \{S, H\}$. In the upper two plots, the indicated property is plotted for all 12 product isomers for each of the frameworks considered, with insets for clarity, while in the lower two plots there is one point per material which describes the extent to which each material favors the linear product isomers.

on product distribution, adding layer of complexity to traditional shape selectivity theory which uses purely geometric considerations to explain differences in product distributions between chemically similar zeolites.[47] The strong π-orbital interactions between the double bonds of the olefin isomers and the open metal site in the MOF-74 series enthalpically favors the linear isomers, for which the double bond is more accessible. For the same reason, since linear product isomers have a stronger tendency to adsorb with their π bonds facing the open metal site, they lose more configurational entropy upon adsorption compared to branched isomers.

The effect of these π-orbital interactions can be seen in the comparison of the binding sites of the double bond in metal-organic and zeolite frameworks (Figure 2.10). In the Ni-MOF-74 the 1-hexene double bond tends to adsorb closer to open metal sites than the less-accessible double bond in cis-2-hexene, which in turn is still more localized near the metal sites than cis-3-methyl-2-pentene. In these sites, 1-hexene, cis-2-hexene, and cis-3-methyl-2-pentene

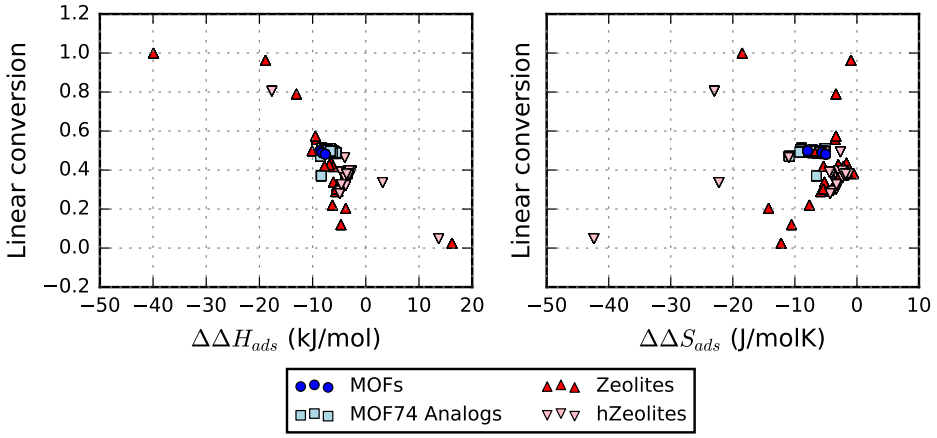

Figure 2.9: Linear conversion of all frameworks vs $\Delta(\Delta H_{ads})$ (left) and $\Delta(\Delta S_{ads})$ (right). The correlation between linear conversion and $\Delta\Delta H_{ads}$ of the porous materials indicates that enthalpy of adsorption is the dominant contributor to differences in linear conversion between materials. By contrast, there is little correlation between linear conversion and $\Delta\Delta S_{ads}$.

have $\Delta H_{ads} = -38.8\,\mathrm{kJ\,mol^{-1}}$, $-38.7\,\mathrm{kJ\,mol^{-1}}$, and $-36.5\,\mathrm{kJ\,mol^{-1}}$, respectively. The same pattern of adsorption site localization, coupled with more favorable ΔH_{ads} for the linear isomers, is visible in Mg-MOF-74 and Mg-MOF-274 (Supporting Information).

In FAU, since there are no specific framework-π bond interactions, there is little difference between the adsorption sites of the three isomers. 1-hexene, cis-2-hexene, and cis-3-methyl-2-pentene have $\Delta H_{ads} = -28.8\,\mathrm{kJ\,mol^{-1}}$, $-30.6\,\mathrm{kJ\,mol^{-1}}$, and $-30.8\,\mathrm{kJ\,mol^{-1}}$, opposite the order of adsorption strength in Ni-MOF-74. As a result the zeolite disfavors the linear isomers compared to the MOF. Probability density plots for other frameworks are provided i the Supporting Information. In some of the probability density plots for other zeolites, the difference between adsorption sites of the branched and linear isomers than in FAU. There are regions with higher probability of 1-hexene adsorption in AET and hypothetical zeolite h8160847, for example, which are closer to the pore walls and extend into more constrained pockets in the frameworks. However, they do not coincide with a more favorable ΔH_{ads} for linear molecules compared to the branched ones, as is the case in Ni-MOF-74.

From these observations we can infer a few design rules to guide the synthesis of new materials for propene dimerization and other olefin oligomerization reactions. To increase the linear conversion of a zeolite material, a smaller framework size of 5 Å to 7 Å can be used. Alternatively, one can also tune the pore chemistry by taking advantage of the large chemical design space of MOFs. A significant enhancement in linear conversion can be achieved by introducing a high density of open metal sites to preferentially bind the double bond of the olefins. $Ni_3(BTC)_2$ also has open metal sites[65] and could be used as a candidate for this reaction and a template upon which to base analogous structures.

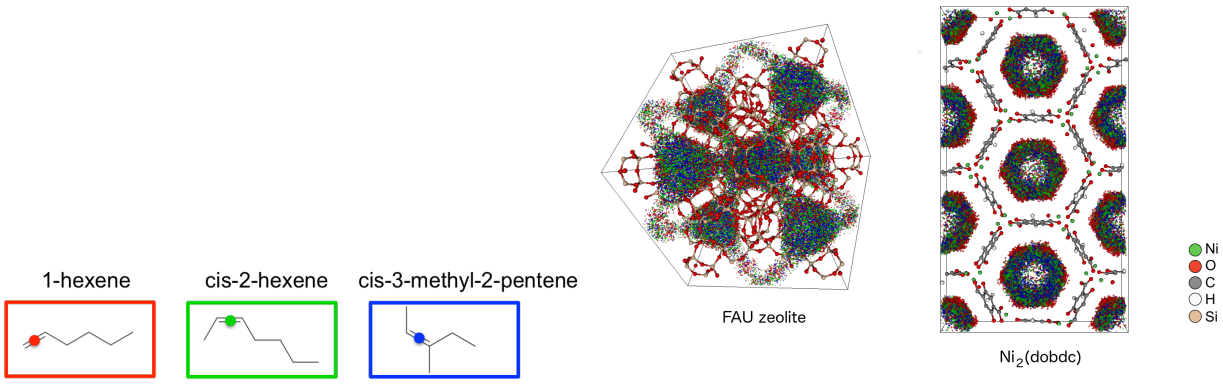

Figure 2.10: Probability density plots of C_6 olefin isomer adsorption sites inside FAU zeolite and Ni-MOF-74. The probability densities correspond to the indicated points marking the geometric center of the π bond on the three product isomers shown at top.

2.5 Conclusions

In conclusion, we have shown that the product distribution of the propene dimerization reaction in different porous materials can be modeled computationally using equilibrium simulations and a three-point charge description of the π bond of the olefin double bond. From the free energy profiles computed for the different materials, we predicted a trend of increased linear conversion in open metal site MOFs compared to zeolites that is in good agreement with the linear conversion observed in experiments.

We extended our study to other zeolitic and metal-organic frameworks, both synthesized and hypothetical, in order to better understand the material properties which influence dimerization product distribution. We found that for frameworks with a pore diameter under 10 Å, selectivity toward linear isomers is a sensitive function of pore size, with very high linear conversion around 5 Å. In this regime the effect of pore size on the product distribution can be attributed to changes in the enthalpy of adsorption. It is important to note that in industrial applications, a framework with such a small pore size might be disadvantageous due to diffusive barriers that would result.

Above 10 Å pore diameter, the linear conversion for the zeolite materials plateaus at around 40%, while the linear conversion for the MOFs increases and remains steady at approximately 50%, with a few frameworks even predicted to have higher linear selectivity than the experimentally high-performing Ni-MOF-74. This striking enhancement in linear conversion for MOFs is due to preferential adsorption of π bonds at open metal sites.

These results elucidate some of the mechanisms governing product distribution in the propene dimerization reaction, and suggest promising not-yet-synthesized frameworks that could deliver higher linear conversion than the existing catalysts. Further work is needed to investigate the product distribution over different classes of open metal sites, for example copper paddlewheel-type structures, to see whether the linear enhancement effect is specific

to the open metal site motif in the MOF-74 family. In addition, in this study we only accounted for thermodynamic considerations in predicting the linear conversion in different materials. For practical applications there are many other factors such as framework stability and diffusion limitations which we did not address. Additional theoretical and experimental studies could clarify the influence of these phenomena on the product distribution.

Chapter 3

Metal-Organic Frameworks for THC Sensing*

3.1 Introduction

Cannabis has in recent years seen increasing decriminalization for both recreational and medical use under some local and state jurisdictions. Since 2012, 10 U.S. states have legalized recreational use of cannabis and 33 states medical use of the drug, coinciding with a shift in societal attitudes regarding cannabis use.[67,68] Immoderate cannabis use has been shown to have public health and safety implications, for example a moderate increase in risk of injury or fatality while driving under intoxication.[67,69] As a result, increasing use of cannabis requires improved methods, similar to alcohol, for portable detection of cannabis intoxication in order to promote more consistent cannabis regulation and safer cannabis use.

The pharmacological effects of cannabis result from a variety of chemical compounds, including several hundred types of cannabinoid which can be found in the plant. The principal psychoactive component of cannabis is Δ^9-tetrahydrocannabinol (THC), which affects motor and cognitive function and has been linked to increased risk of motor vehicle crashes.[69–71] For roadside testing applications, breath-based testing of THC has the greatest potential as it is less invasive than testing of urine or blood.

Breath detection has other advantages as well. The window of detection of THC in breath (from 0.5 to up to 2 h after cannabis use) coincides with the period of peak impairment.[72,73] THC and its metabolites can also be detected in blood and urine, but as cannabinoid compounds persist for several times longer in these bodily fluids they are not a reliable indicator of intoxication.[68,74] Though the full window of driving impairment may extend longer than 2 h,[71] the short detection window in breath may be able to be extended using methods that have increased sensitivity.

*This chapter is based on Ongari, D., Liu, Y. M. & Smit, B. Can MOFs Be Used for THC Breathalyzers? *Submitted* (2019), to which the two first authors are equally contributing.

THC sensing from breath is challenging because it is present in a very small concentration in vapor phase (the vapor pressure of THC at 40 °C is $1.15 \cdot 10^{-4}$ Pa, *i.e.*, 10^8 times lower than the vapor pressure of ethanol at the same temperature, 17.877 kPa)[75–77]. Successful breath assays of THC have required that picogram amounts of THC be collected from aerosol droplets in the breath that are expelled when the subject breathes out.[73,78] Other complicating factors of THC detection include its fast metabolism in the body and the other chemically similar compounds that are present in cannabis, such as cannabinodiol (CBD) and tetrahydrocannabinolic acid (THCA), a metabolyte of THC. Efforts to detect THC from breath have largely relied on mass spectrometry[71,78] and, more recently, a fluorescence-based assay.[79]

In this work we propose using metal-organic frameworks (MOFs) to adsorb THC prior to detection, which can be carried out using existing optical,[80–82] electrochemical[83], or fluorescence-based[79] sensing methods. MOFs are porous, crystalline materials composed of metal nodes linked by organic ligands in a three-dimensional network.[20,84–86] They have a high surface area for adsorption and a high degree of chemical tunability that makes possible the synthesis of a framework with ideal properties for a given application. The huge design space of MOFs is reflected in the large and growing number of experimentally synthesized MOFs that have been reported to date, nearing 100 000 structures.[23] With this chemical diversity of structures, MOFs have exhibited unmatched performance in applications such as adsorption, catalysis, and sensing.[20,84]

MOFs have been used as a detection medium for biologically relevant molecules such as chemical warfare agents and toxic industrial chemicals.[87,88] Sensing in biological systems poses particular challenges for MOFs, including interference of water with the adsorbate of interest, and the thermal and chemical stability of MOFs in the presence of bodily fluids such as blood or saliva. One solution is to use hydrophobic materials that would minimize adsorption of water in order to detect the analyte or to adsorb water from the sample before it comes in contact with the MOF.

More generally, detection of larger biologically-relevant molecules in MOFs is interesting because the adsorption energy of larger molecules may be more dependent on pore shape than adsorption of small gas molecules such as N_2 and CO_2. This allows for potentially higher selectivity when the pore shape can be optimized for an adsorbate molecule. Simulation of larger molecules can also pose computational challenges. Properties such as diffusion and adsorption become more expensive to compute, and the difference in computational time can be significant, especially when screening a library of structures for a particular application. Strategies to reduce computational cost while still capturing the decisive properties for an application can be useful. Toward this end, we tested two models of THC of different complexity.

With these adsorbate models, we investigated 645 MOF structures that have been filtered from a large set 5171 materials, that combine the CoRE MOF database[89] and the MOF-74 analog database.[25] Geometric analysis of the the porous frameworks was carried out with the existing Zeo++ package[90] and a novel method using 2D projections of the adsorbate and pores to analyze pore accessibility toward asymmetric probe molecules. We used NVT and

Widom insertion simulations to compute the adsorption energy and Henry coefficient of THC in these structures, and to determine whether using a simplified model (representing only the rigid aromatic head) would be an appropriate screening strategy for THC. We identified motifs of adsorption in the most promising structures. Finally we computed the THC/H_2O selectivity in these materials and determined which might be suitable for THC detection in the presence of water.

3.2 Computational Methods

The atomic positions of the THC molecule were optimized with the CP2K package[91] using PBE functional[92] with Goedecker-Teter-Hutter (GTH) pseudopotentials,[93] DZVP-MOLOPT-GTH Gaussian basis set[94] and an auxiliary plane wave basis set with cutoff at 700 Ry. A 30 Å × 30 Å × 30 Å box was adopted with a wavelet-based Poisson solver to exclude periodic boundary conditions. The energy density from the converged calculation was used to compute DDEC-06 point charges, using the software Chargemol.[95]

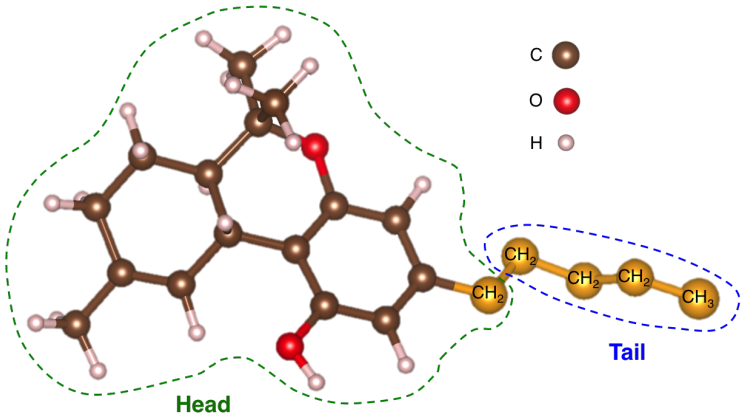

Figure 3.1: Model of THC used in this work. The structure of the molecule was optimized using DFT, and the molecule is divided into a rigid "head" and a flexible "tail" section. The united-atom beads are shown in yellow, while the rest of the molecule is described with all atoms.

The model we used for THC is shown in Figure 3.1. We divided the THC structure in two sections: an n-pentyl group, which we refer to hereafter as the "tail," and the remaining aromatic terpenoid group, which we refer to as the "head." Note that the α-carbon of the 6-carbon alkyl chain of THC is considered to be part of the head group, since the planar structure of the aromatic ring constrains the position of the α-carbon with respect to the aromatic group. We employed a united-atom description of the flexible tail, treating it as a chain of four CH_2 sites and a final CH_3 site. For the head group we used an all-atom description. The head group was kept rigid due to its constrained geometry.

We utilized a Lennard-Jones 12-6 potential with Lorenz-Berthelot mixing rules to model the dispersion interactions between THC and the framework. For the framework atoms and the all-atom head group, the Lennard-Jones ε and σ parameters were taken from the Universal Force Field (UFF).[34] For the coarse-grained tail group, TraPPE force field parameters were used.[96] Intramolecular interaction of the tail (bond, angle, and dihedral interactions) were also taken from the TraPPE force field. The carbon-carbon bonds of the hydrocarbon tail were kept rigid, with a bond length of 1.54 Å. The angles were described with a harmonic potential with an equilibrium angle of 114° and a spring constant of 62 500 K rad^{-2}, and the dihedrals with the TraPPE dihedral form

$$U = p_0 + p_1[1 + \cos\phi_{ijkl}] + p_2[1 - \cos 2\phi_{ijkl}] + p_3[1 + \cos 3\phi_{ijkl}]\,, \tag{3.1}$$

where p_0/k_B, p_1/k_B, p_2/k_B, and p_3/k_B were 0 K, 335.03 K, −68.19 K, and 791.32 K, respectively. These parameters are consistent with the TraPPE united-atom model of n-alkanes.[96]

Short-range dispersion interactions had a cutoff distance of 12 Å without applying tail corrections. The unit cells of all frameworks were replicated so that perpendicular widths between opposite faces were larger than twice the cutoff distance. The positions of the framework atoms were kept fixed for all simulations.

In this study, two models of THC are used: the THC-FULL model and the THC-HEAD model. The THC-HEAD model includes only the bulky head group of the THC molecule, and is fully rigid. The THC-full model treats the aromatic head of the THC molecule as rigid, but also includes the hydrocarbon tail, which is flexible.

We used Monte Carlo (MC) methods to screen adsorption of THC in our materials library using both THC-HEAD and THC-FULL models. The tail of the THC-FULL model was simulated using configurational-bias Monte Carlo (CBMC).[97] We ran Widom insertion simulations in the desolvated framework and NVT simulations with a loading of 1 molecule per simulation cell. In NVT simulations we chose moves with equal probability of translation, rotation, reinsertion, and reinsertion-in-place, where the last is a CBMC move that applies to the THC-FULL model. For THC, we used blocking spheres generated in Zeo++ with a probe radius of 2.5 Å. This is smaller than the size of the THC molecule, and was chosen conservatively in order not to exclude pores which might be accessible to THC considering a minimal vibration of the crystal. A more detailed method to determine pore accessibility is detailed in the following section. MC simulations were run in the RASPA package,[98] considering a temperature of 309 K, the human body temperature.

Our models and simulations were first tested in depth on a single framework, the well-studied Mg-MOF-74[62,99–101]. This preliminary analysis led to the conclusions that Coulombic interactions can be neglected for the investigation of THC adsorption, and the need of 10 times more MC Widom insertions ($2 \cdot 10^7$ insertions) than MC NVT steps ($2 \cdot 10^6$ steps)to achieve a comparable convergence. We report the full analysis on Mg-MOF-74 in the Supporting Information.

To check for selectivity of THC adsorption in the presence of water vapor, we computed the Henry coefficient of water using MC Widom insertions following the protocol of

Moghadam *et al.*[102] Point charges for these materials were derived using the EQeq method,[24] that we recently benchmarked.[103] To model water, we used the TIP4P model[104] with a united-atom Lennard-Jones interaction site. We computed K_H for water in these materials using 1 000 000 Widom insertion steps and blocking spheres computed for a probe radius of 1.5 Å. Since we are including MOFs which have a coordinatively unsaturated metal site (also referred to as open metal site, or OMS) one has to consider that modelling interactions using only Coulombic and dispersion interactions often leads to an underestimation of the binding of polar gas molecules at these sites. Our group spent a considerable effort to address this issue, by proposing tailor made corrections to tune the force field for some specific gas-OMS interactions.[99,105,106] However, a reliable and systematic correction for all the combinations of polar molecules (such as water) and OMSs has not yet been proposed, and therefore it is of common practice to take the results from standard interactions (e.g, using point charges and off-the-shelf Lennard-Jones parameters) with a grain of salt and analyze overall trends over a large set of structures.[102,107,108]

3.2.1 Geometric Pore Analysis

Zeo++[90] was used to compute the most common geometric pore descriptors, including geometric void fraction, accessible surface area, pore limiting diameter (PLD), largest included sphere (LIS), and blocking spheres.

Zeo++ assumes idealized spherical probe molecules for its analysis. This is useful for adsorbates which are approximately spherical or at least have a circular cross-section, however, THC is asymmetric from all view points and a spherical probe is not sufficiently representative of its structure. Here we introduce another method for determining framework accessibility, applicable to THC (see Figure 3.2) and similarly asymmetric adsorbates.

Our algorithm utilizes 2-D projections of both the THC molecule and the limiting-diameter pore to calculate the overlap in their cross-sectional areas. The cross section of the probe molecule was represented as an ellipse of 3.5 Å × 5 Å, which we determined to best match the 2-D projection of THC down its longest axis (Figure 3.3).

In order to compute an equivalent 2-D projection of the pore geometry, we modified the Zeo++ code in a local version[109] to not only print the PLD but also the coordinates of the Voronoi edge associated with that PLD, $\vec{E}_{PLD}$. We define at the midpoint of $\vec{E}_{PLD}$ a plane perpendicular to $\vec{E}_{PLD}$, denoted $P_\perp$. The edges of the Voronoi network define the paths along which an adsorbate can travel in a material, and we thus consider $P_\perp$ the cross-sectional plane where the adsorbate encounters the material's PLD. We next project onto this plane all the atoms of the framework that the probe would "feel" if it were to pass through. Since the rigid head of THC is approximately 10 Å in diameter (Figure 3.2 bottom), we include in the projection all framework atoms within 5 Å distance from $P_\perp$ and within 8 Å radially from the line defined by $\vec{E}_\perp$. All atoms within this cylindrical cutoff are projected onto $P_\perp$. We evaluate the fit of the elliptical probe in the pore projection, by varying the angle and position of the probe in the middle of the pore and minimizing the area of overlap.[110]

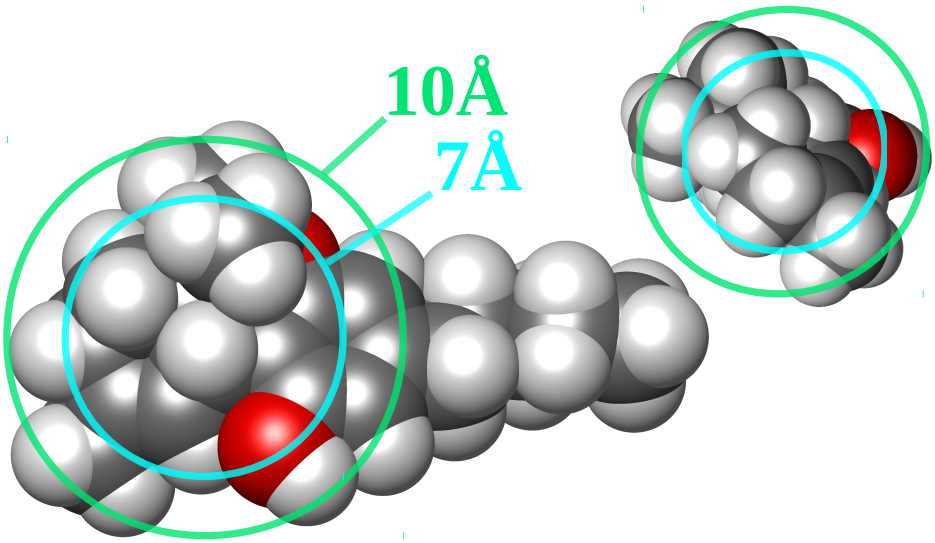

Figure 3.2: Cross-sectional diameters of THC molecule, from a frontal and lateral view. The diameters of the atoms are displayed as the Lennard-Jones's sigma from UFF:[34] 2.57 Å for H, 3.43 Å for C, and 3.12 Å for O.

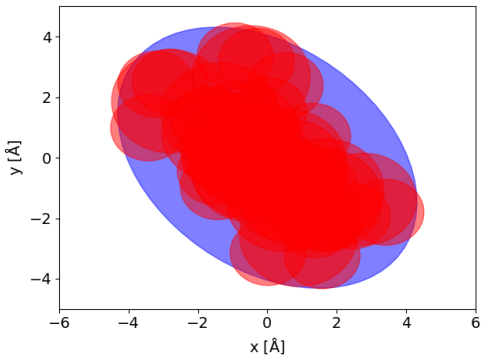

Figure 3.3: Projection of THC molecule (red circles, radii represent Lennard-Jones sigma) overlaid with an ellipse (blue) with minor and major axes of 3.5 Å and 5 Å, respectively.

3.3 Results

3.3.1 Screening MOF Databases for THC Adsorption

We assembled a database of MOFs to screen for THC selectivity, considering the frameworks from the Computation-Ready Experimental (CoRE) MOF database,[89] as well as the MOF-74 analogs from Witman *et al.*[25] A large fraction of these porous frameworks can be excluded from our screening on the basis of accessibility: THC, due to its size, can diffuse only through pores that are connected by wide channels. Therefore, we excluded all the MOFs with a computed pore limiting diameter (PLD) less than 7 Å, leaving about 14 % of the frameworks

in the original databases (Figure 3.4). We also removed the CoRE MOFs that have a net charge and contain ions in the pores to counter-balance their charge. The modelling of these counter-ions requires more advanced techniques as they can move inside the pore. Finally, we excluded other six materials that do not contain any carbon atoms in their structures and therefore can not be considered MOFs (MARJAQ, LETPOR, LETPUX, LETQAE, LETQEI, LETRAF). These probably come from erroneous parsing during the creation of the CoRE MOF database.

We chose a lower PLD limit of 7 Å as it corresponds to the narrowest part of the terpenoid group (Figure 3.2). However, it is still possible that in materials with a PLD of 7 Å would not be permeable by a THC molecule, if the perpendicular axis is smaller than the longer axis of THC (with size of roughly 10 Å). This motivates our development of the novel "ellipsoid overlap" method to determine more accurately the accessibility to THC, discussed in the following section.

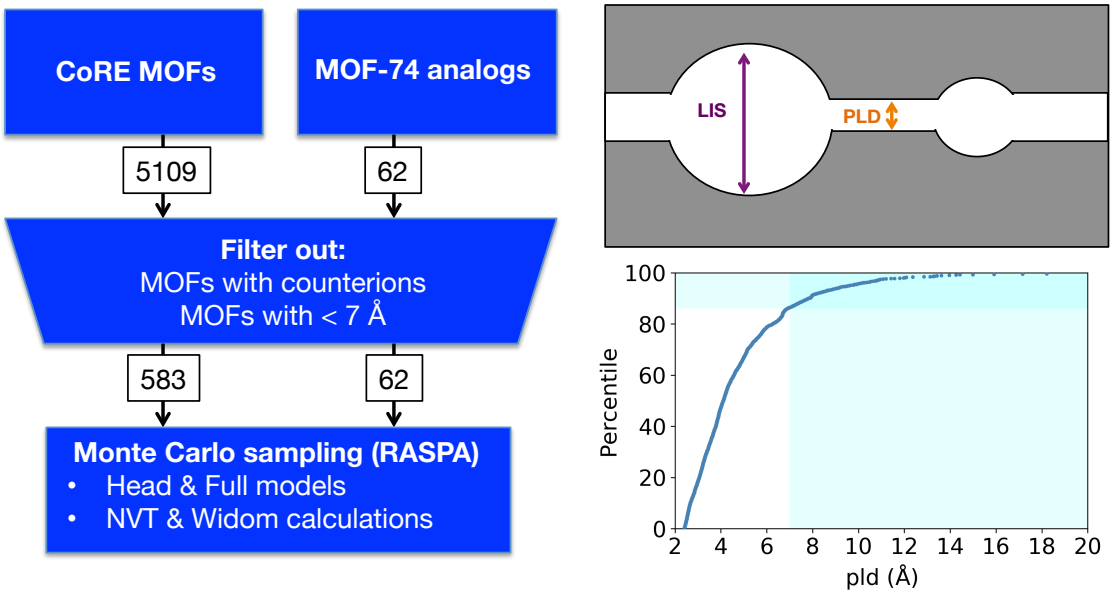

Figure 3.4: Diagram of screening workflow, including a filter to select only materials with PLD larger than 7 Å and without counterions in the pores.

For the remainder of this work we consider only the subset of 645 MOFs with PLD>7 Å and without counter-ions. The distribution of properties of these materials are shown as histograms in Figure 3.5. All the MOF-74 analogs have a PLD between 14 Å and 45 Å, as seen in the inset of the figure. The larger pore size MOFs will allow us to observe the influence of the ligand type for adsorption in MOFs with all the same topology.

We start by comparing the Henry coefficient for all MOFs as obtained from Widom insertions using the THC-HEAD and the THC-FULL models. This will allow us to assess the contribution of the alkyl tail for the adsorption properties in a diverse set of pore topologies.

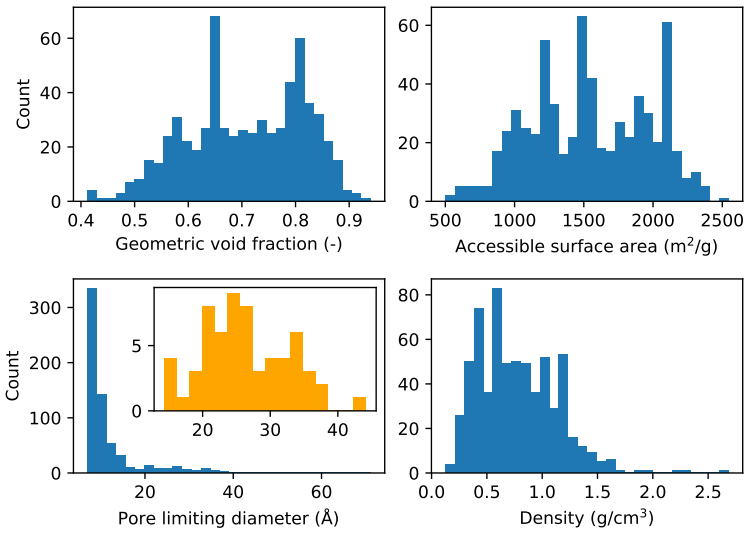

Figure 3.5: Distributions of pore descriptors for 645 frameworks screened in this study. The orange inset shows the pore limiting diameters for only the MOF-74 analog library.

As one can see from Figure 3.6 the THC-HEAD model, despite its simplicity, leads to a computed Henry coefficient that correlates very well with the full model.

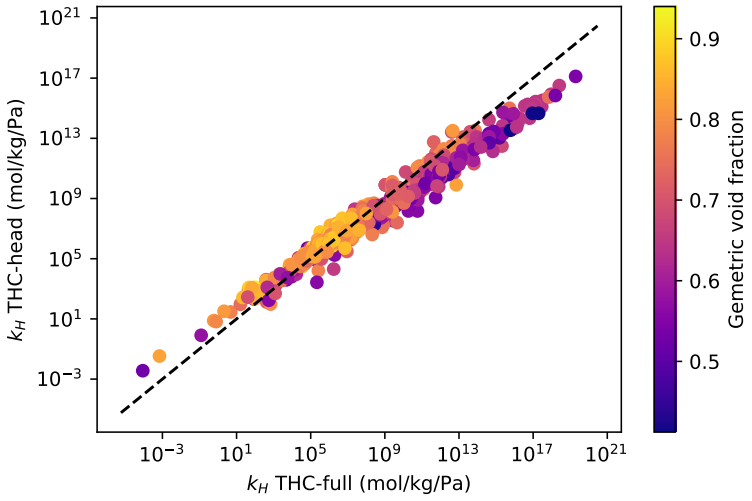

Figure 3.6: Parity plot of the Henry coefficient for the THC-HEAD and THC-FULL models. The geometric void fraction of the frameworks is indicated by the colouring. These results are computed from 20 millions Widom insertions.

It is interesting to observe the two extremes of low and high Henry coefficient. In frameworks where the Henry coefficient is high (*i.e.*, in more favorable adsorption sites), the inclusion of the flexible alkyl tail increases the Henry coefficient from the THC-HEAD model,

with only a few exceptions. This phenomenon is the expectable consequence of adding more atoms, *i.e.*, more dispersion interactions with the adsorbent. On the other end, in frameworks where the Henry coefficient is very low, adding the tail makes the Henry coefficient slightly lower. This suggests that these materials with low Henry coefficient have pores where the THC-HEAD already barely fits, and the inclusion of the tail makes these crowded sites even more sterically hindered. Despite these systematic differences, the inclusion of the flexible tail in the model does not significantly change the overall ranking in performance of these MOFs, suggesting that the THC-HEAD model could be a suitably accurate proxy for screening for adsorption properties.

Using both models we can now evaluate the contribute of the entropy and the enthalpy on the Henry coefficient. Since the enthalpy of adsorption can be computed more efficiently from an NVT simulation, we are interested to assess if this can be used as a reasonable ranking parameter for THC adsorption. Indeed, we showed in the Supporting information that NVT simulations of THC in MOF-74 already converged after $2 \cdot 10^6$ MC steps while, when probing with Widom insertions, a comparable convergence can be achieved with $2 \cdot 10^7$ insertions. This makes, in practice, the Widom technique roughly 10 times more expensive. Moreover, by comparing the same quantity, the enthalpy of adsorption ($\Delta H_{ads} = \Delta E_{ads} - RT$), as computed separately by both Widom and NVT, we have a further check on the convergence of the calculations. The entropic and enthalpic contributions to the Henry coefficient are shown in Figures 3.7, together with the comparison with the enthalpy as computed from NVT simulation.

We can observe that the main contribution to the Henry coefficient, *i.e.*, from the equation

$$k_H \cdot \rho_{MOF} = \frac{1}{RT} \exp\left(\frac{\Delta S_{ads} \cdot T - \Delta H_{ads}}{RT}\right), \tag{3.2}$$

comes from the enthalpic term. Indeed, considering the whole set of frameworks, the observed range of enthalpies is more than 5 times larger than the entropic range (in Figure 3.7 we multiplied the entropy by the temperature to have a quantity with the same units of energy as the enthalpy). This gets exponentially enhanced in equation 3.2, letting us conclude that the main contribute to the Henry coefficient, for THC adsorption, comes from the enthalpy (*i.e.*, from the adsorption energy). This quantity can be computed with less computational cost from an NVT simulations, and we may therefore expect that it provides already a quick and accurate ranking to identify materials with high Henry coefficient for THC. Figure 3.7 also shows that the enthalpy from Widom insertions matches well with the enthalpy from the NVT simulations, confirming a good convergence for both.

Considering together the results of Figures 3.6 and 3.7, we can conclude that a ranking of materials that are favourable for THC adsorption can be achieved in two ways: (i) by directly comparing the computed Henry coefficient from the most expensive and accurate calculation, *i.e.*, the Widom adsorption using the THC-FULL model, and (ii) by comparing the heat of adsorption from NVT for the THC-HEAD model, a less computationally expensive method. Considering the 10X speedup due to faster convergence of NVT simulations, and the 1.5X-3X speedup of using the THC-HEAD model (see benchmark calculations in the

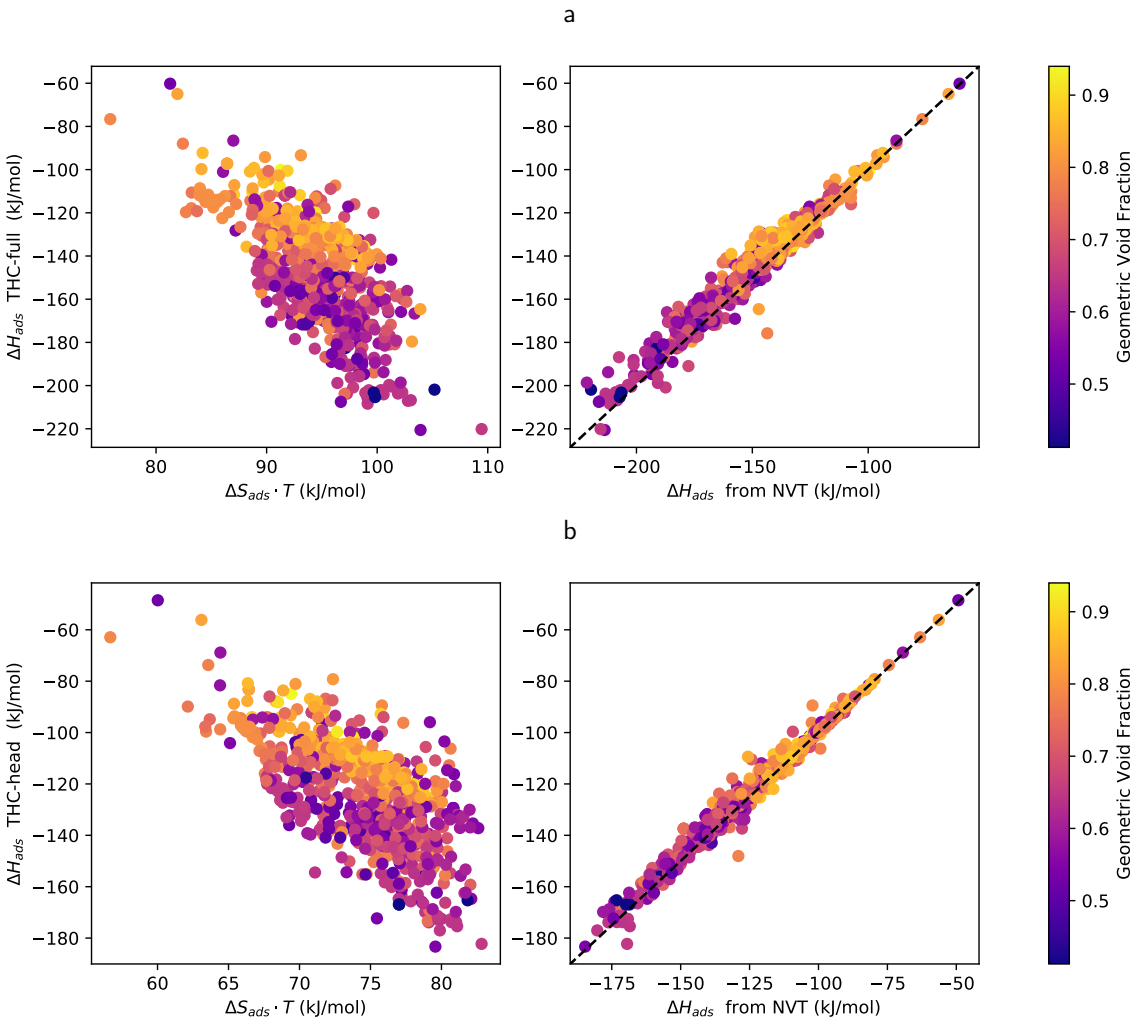

Figure 3.7: The Henry coefficients is decomposed in its enthalpy and entropy components for the THC-FULL (a) and THC-HEAD (b) models. In the parity plot on the right, the adsorption enthalpy computed from Widom insertions (y-axis) is compared with the same quantity as obtained from NVT simulations (x-axis).

Supporting Information), the second protocol results up to 30 times faster than the brute-force calculation of the Henry coefficient with the more realistic and flexible THC-FULL model. Moreover, figure 3.8 shows that there is a very strong correlation, and one can relate the two calculations with the empirical relation

$$k_H^{THC\text{-}full} = \exp(-26.41 - 0.38 \cdot \Delta E_{ads} \pm 3.0)\,, \tag{3.3}$$

with $k_H^{THC\text{-}full}$ in $\mathrm{mol\,kg^{-1}\,Pa^{-1}}$ and ΔE_{ads} in $\mathrm{kJ\,mol^{-1}}$.

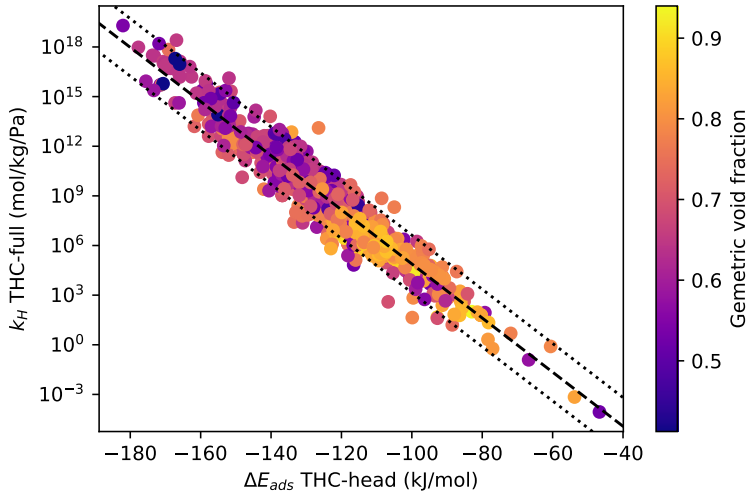

Figure 3.8: Comparison of the Henry coefficient from Widom insertions using the THC-model and the energy of adsorption from NVT MC simulations for the THC-HEAD model. The empirical relation between the two is drawn with a dashed line, while the confidence threshold is shown in dotted lines. This relation has been obtained from linear interpolation.

Next, we investigate the correlation between adsorption and conventional descriptors, to highlight trends that can be exploited for the rational design of new materials. In Figure 3.9, we plot the Henry coefficient and the adsorption energy against geometric void fraction, volumetric surface area, pore limiting diameter, and largest included sphere (LIS, as defined in Figure 3.4).

For most of the descriptors, there is not a clear correlation with Henry coefficient or adsorption energy. The primary interesting feature we can highlight is the similar adsorption energy, around $130\,\mathrm{kJ\,mol^{-1}}$–$150\,\mathrm{kJ\,mol^{-1}}$ for all the MOFs having large pores and channels (*i.e.*, large PLD and LIS), with many MOF-74 analogs falling in this category. To understand this pleateau of adsorption properties, we consider that in large channels and cavities the pore walls have very large radii of curvature and appear close to flat to an adsorbate. When the THC molecule adsorbs to such a low-curvature surface, the adsorption energy is only influenced by the chemistry of the adjacent surface and not by the shape of the pore. Considering the similar adsorption energy for these structures we can conclude that the variations

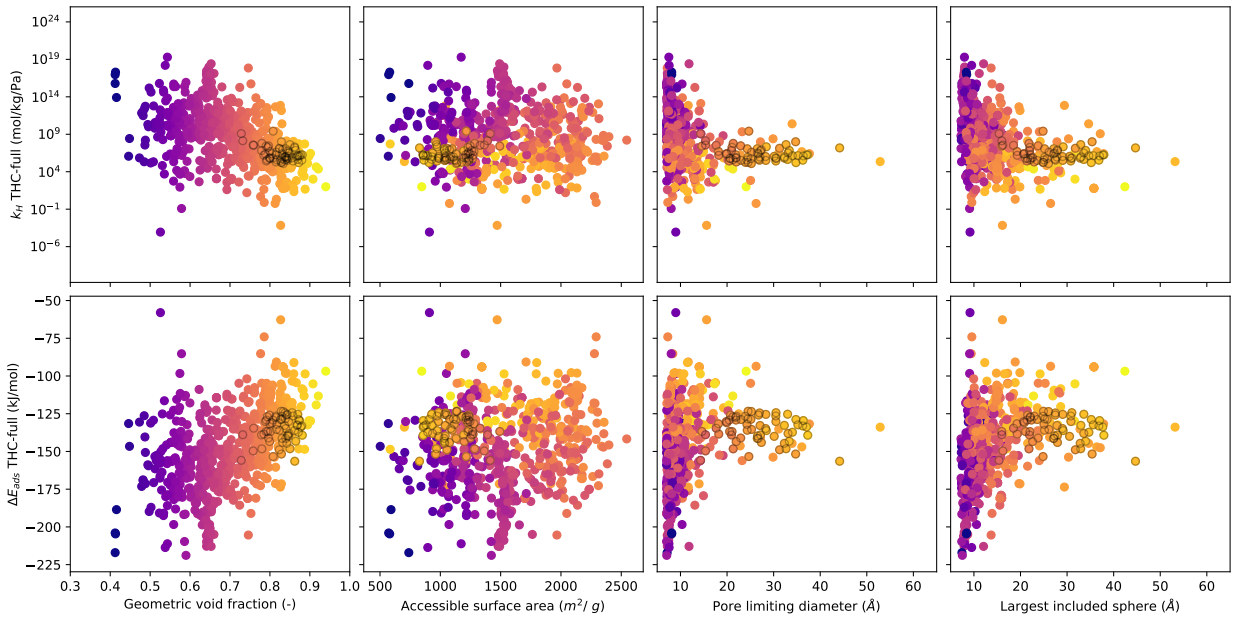

Figure 3.9: The Henry coefficient (from Widom) and energy of adsorption (from NVT) are plotted against the pore descriptors: geometric void fraction, accessible surface area (probed with a sphere of 1.86 Å radius), pore limiting diameter and largest included sphere. The color also describes the geometric void fractions of the frameworks. The 62 MOF-74 analogs are highlighted with grey edges.

in chemistry, *e.g.*, between different ligands in MOF-74 analogs, are not significantly affecting the strength of adsorption. Frameworks with smaller pore limiting diameter have a large range of adsorption energies, extending both lower and higher than the range of adsorption energies for materials with larger PLD. Smaller PLD is correlated with a higher likelihood of finding strongly favorable and unfavorable adsorption energies. The existence of these dual extremes suggests that when pores are small, there is a greater likelihood that the THC molecule will either bind in a very tight, very favorable pocket, or that steric hindrance of an ill-fitting pore will penalize binding. This is consistent with previous work showing similar widening ranges of adsorption energies in small pores for linear and branched alkanes.[38]

3.3.2 Pore Accessibility to Asymmetric Probe Molecules

We are interested in restricting our screening only to those materials through which THC can percolate, as well as determining whether THC can pass through a particular channel in a material. Most geometric methods to evaluate pore accessibility typically use idealized spherical probe molecules for their analyses. For example, the pore limiting diameter indicates the size of the largest sphere which can percolate through the material, giving an idea of the barriers to diffusion. This is useful for adsorbates which are approximately spherical

or at least have a circular cross-section, however, THC is asymmetric from all view points and is therefore characterized by multiple characteristic lengths: As seen in Figure 3.2, when the THC molecule is viewed down its longest axis, it has a cross section with dimensions of roughly 10 Å and 7 Å along its longer and shorter axes, respectively. Therefore, THC should be able to traverse channels with a PLD greater than its longest dimension, while it would not be able to fit through a channel whose PLD is smaller than its shortest dimension. For intermediate pore sizes, accessibility depends on the precise pore geometry as compared with the geometry of the probe molecule.

We developed a method which can be used to determine whether an asymmetric molecule can percolate through a porous material, by comparing the shape of the probe molecule to the cross-sectional geometry at the narrowest part of the pore. The algorithm, which is described in detail in the Methods section, computes the minimum area of overlap between the probe and the pore. We present our results applying this algorithm to our screening database in this section.

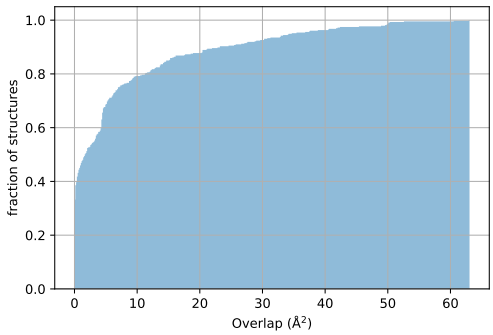

Figure 3.10: Cumulative probability distribution of overlap area.

The cumulative probability distribution of the overlap area for 433 materials with PLD between 7 Å and 10 Å is shown in Figure 3.10. It is not obvious where to draw the line between an accessible and non-accessible material; however, we determine that 4 Å is a sensible threshold for more accessible pores as the cumulative distribution shows a steep increase just above 4 Å. Further examining the probability distribution, we note that 45% of the materials with PLD between 7 Å and 10 Å have an overlap of less than 1 $Å^2$, and 60 % of materials have an overlap below 4 $Å^2$. This allows us to exclude more materials from our consideration of most promising adsorbents, as we show in Figure 3.11, which plots the Henry coefficient vs. PLD of structures with points colored to indicate overlap area, where the color scale extends to 4 Å.

This analysis also justifies our choice of a conservative initial cutoff of 7 Å PLD, since a higher cutoff might have falsely identified materials such as NIGDEO (PLD=7.15 Å) or SUTBIT (PLD=7.94 Å) as inacessible, while we find that the overlap areas for these materials is are 2.88 Å and 1.68 Å, respectively, below our chosen threshold for accessibility. A visualization of the 2-D projections of the pore (in red) and elliptical probe representing

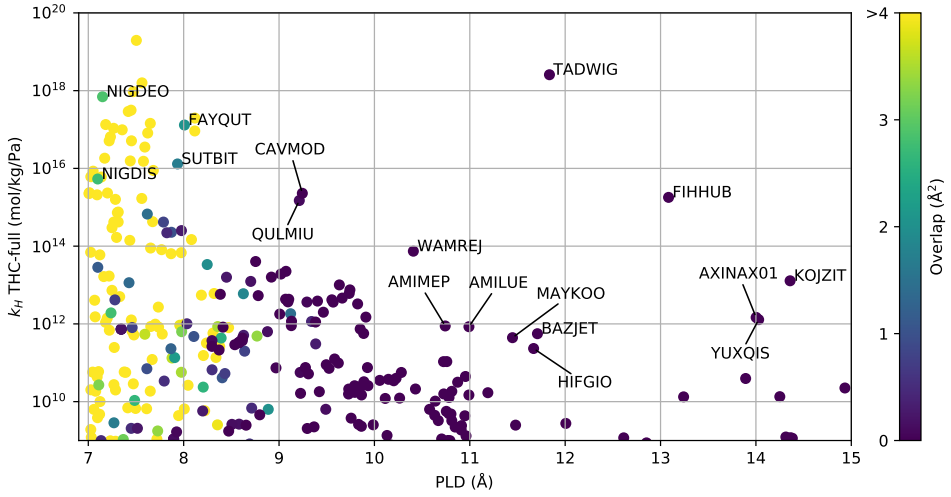

Figure 3.11: Henry coefficient vs. pore limiting diameter (PLD), with point color indicating overlap area. Overlap areas are saturated at 4 Å^2. Materials mentioned in the text are labeled for reference. We note that the overlap area was only computed explicitly for those materials with PLD from 7 Å to 10 Å; for materials with PLD $>$ 10 Å the overlap area was assumed to be 0.

THC (in blue), along with the atomistic representation of the pore, is shown for these two materials in Figure 3.12.

More generally, this method provides a way to quantify pore accessibility to nonspherical adsorbates in an fast and inexpensive manner for high-throughput screening studies. While we use it only for studying accessibility in the pore corresponding to a material's PLD, the algorithm can be flexibly applied to any point inside a material.

3.3.3 Inspection of Promising MOFs for THC Adsorption

Comparing the structures that have the largest Henry coefficients, as shown in Figure 3.11, we identify three "adsorption motifs" associated with high affinity toward THC. The first motif is the presence of narrow pores characterized by low PLD, which serve as tightly fitting adsorption sites for THC. These tight pores contribute strong dispersion interactions to the binding energy, but also lead to slow diffusion because the THC molecules would need to move through the channel in single file. Moreover, the structures with low PLD tend to have a high overlap area, indicating that many of these materials may not even be permeable to THC. We refer to this motif as "narrow channels" and one clear example (which is permeable to THC) is SUTBIT (Figure 3.13). The second motif is associated with larger channels, with a PLD in the range of 8 Å to 11 Å, but low void fractions. This characterizes MOFs that contain many framework atoms in the unit cell. As with the "narrow channels"

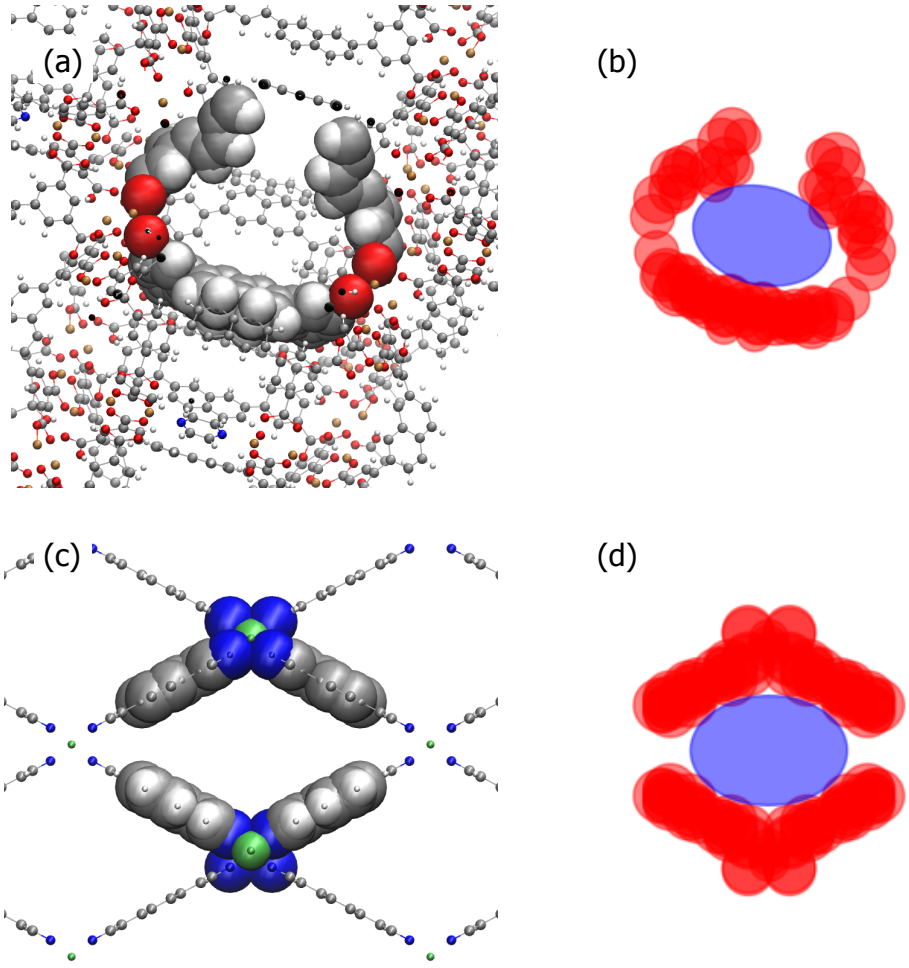

Figure 3.12: Diagram showing the supercell of each framework with atoms within the cylindrical cutoff and the projection of the pore onto $P_{\perp\vec{E}}$ with the minimally overlapping elliptical probe for NIGDEO (a, b) and SUTBIT (c, d). C atoms are shown in gray, H in white, O in red, N in blue, Cu in tan, and Ni in green.

motif, the MOFs displaying the second adsorption motif also exhibit strong framework-adsorbate dispersion interactions, though due to the bulkiness of the framework rather than narrow channels. This motif is found in QULMIU and AMILUE (Figure 3.13) and we refer to it as "thick walls."

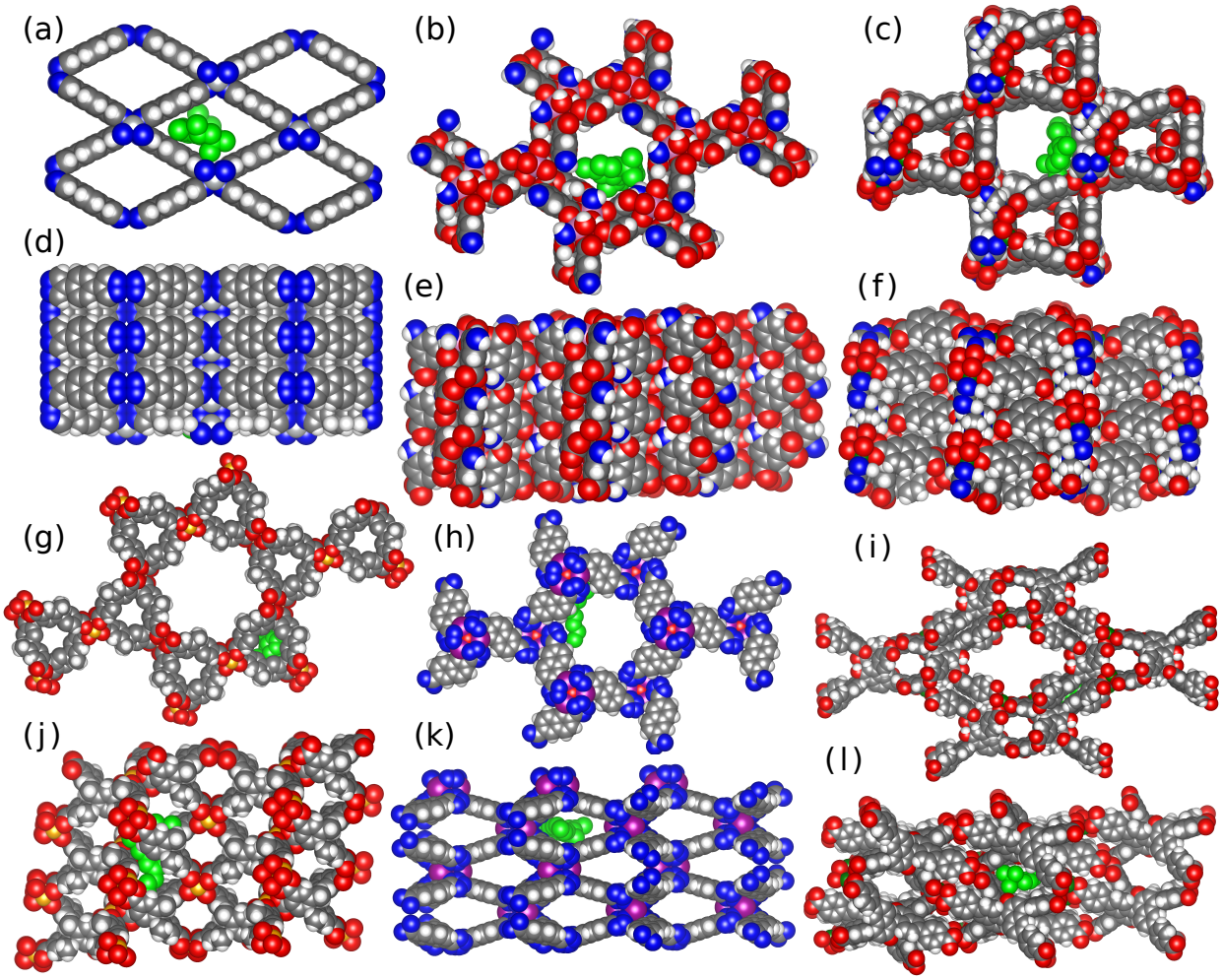

Figure 3.13: The position of adsorbed THC is showed in the pores of six selected MOFs, as discussed in the main text. MOFs are showed from a top and side view: SUTBIT (a,d), QULMIU (b,e), AMILUE (c,f), KOJZIT (g,j), BAZJET (h,k) and TADWIG (i,l). The full-THC's positions have been obtained from equilibrated NVT simulations, and the non-hydrogen elements of the molecule are showed in green. The metals of these MOFs are, respectively: Ni (silver), In (violet), Zn (dark green), Cu (gold), Mn (purple) and Zn (dark green). The colors of nonmetal elements are blue for N, grey for C and red for O.

Note that there is a smooth transition between narrow channels and thick walls: the first has channels with small PLD, while the second has larger channels but also a bulkier framework. The third and final motif, leading to high THC affinity and lower hindrance of

diffusion, represents the most promising feature for THC adsorption: narrow slits, serving as tight binding pockets for THC, which are situated off the sides of wide channels. This configuration is very promising because the THC molecules can diffuse through wider channels (with PLD even above 11 Å) and adsorb in favourable binding sites that also facilitate their detection by constraining the rotational and translational motion of the molecules. This efficient design resembles a car lot, which has wide lanes to access the narrow spaces where cars are parked: therefore, we gave this motif the name "parking spots". An example of parking spots can be found in KOJZIT and BAZJET (Figure 3.13).

Once we have defined these three motifs, it is interesting to note that the permeable material with the highest Henry coefficient for THC, TADWIG, exhibits two of them, both parking spots and thick walls (Figure 3.13). The combination of the two makes it particularly favourable for adsorption and detection of THC.

It is also important to notice that these three adsorption motifs are not restricted to MOF structures: they can in principle be found in other categories of microporous materials such as Covalent Organic Frameworks or zeolites, and they can serve as a guideline to discover or rationally design materials not only for the adsorption of THC, but also for other large molecules with a planar and/or nonspherical shape.

3.3.4 THC Adsorption in the Presence of Water

As a final computational check of feasibility of these materials for THC detection from breath, we consider the selectivity of THC adsorption in the presence of water. Selectivity against water is important for this application since breath is very humid. In order to determine the affinity of the materials toward water, we computed the Henry coefficient of water using MC Widom insertion simulations. The THC/H_2O selectivities (defined as the ratio of K_H of THC to K_H of water) of the materials screened are shown in Figure 3.14. The materials which have an overlap area of less than 4 Å (*i.e.*, in which THC can percolate through the pores) are colored by the Henry coefficient of THC adsorption, and materials with a larger overlap are shown in light gray. The most promising materials as identified in the previous section are labeled. We notice that the upper bound of selectivity is higher as the PLD decreases, reflecting the correlation of higher maximum $k_{H,THC\text{-}full}$ with decreased PLD. In addition, we find that most of the promising materials previously identified also have some of the highest computed THC/H_2O selectivities.

In order to determine the THC/H_2O selectivity needed in a material for feasible detection of THC from breath, we undertake a basic thermodynamic analysis of adsorption. Breath-based THC assays have shown that a large amount of THC is present in aerosolized saliva droplets, leading us to assume that THC is present in both vapor and aqueous liquid phases. Typical concentrations for THC in oral fluid within the first 3 h of smoking are reported to be on the order of 10 µg L^{-1} to 1 mg L^{-1},[74] nearing the solubility reported for THC in aqueous solutions of 1.05 mg L^{-1}.[111] The Henry's law constant for THC in water is 0.024 318 Pa m^3 mol^{-1}.[112] Assuming that THC at such low liquid concentrations is in the Henry regime, we find that the partial pressure of THC in contact with a THC-saturated

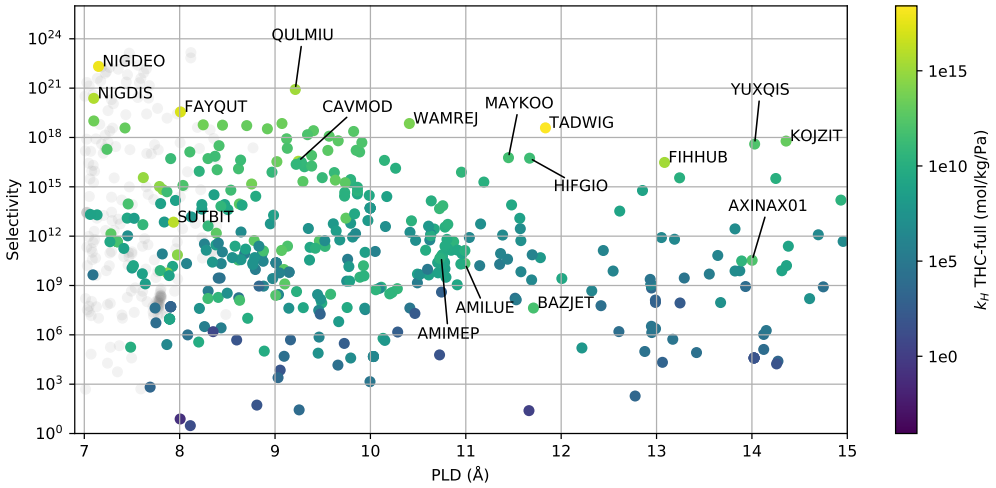

Figure 3.14: Selectivity of THC adsorption in the presence of water. The colors of the points indicate the Henry coefficient from Widom insertion.

aqueous phase is $8.12 \cdot 10^{-5}$ Pa at 25 °C; for oral samples where the liquid-phase concentration varies, the partial pressure could be up to two orders of magnitude lower. As breath has a nearly 100% relative humidity, we can assume that the partial pressure of water is near its saturation pressure, $3.17 \cdot 10^{3}$ Pa at 25 °C, which is 7 to 9 orders of magnitude larger than the partial pressure of THC in breath. If the selectivity of the THC adsorbent is 10^{12} or larger, the THC uptake will be at least 1000X that of water, even for lower concentrations of THC in breath. About 40% of materials meet this criteria (Figure 3.15), and several of the promising materials we identified have selectivities many orders of magnitude larger.

This does not mean, however, that materials with a lower selectivity cannot be used in a breath-based THC sensing device. In order to make detection with lower-selectivity materials feasible, the detection device could have a way to remove most of the moisture from the air, perhaps using a very hydrophilic layer first to "dry" the air before it reaches the adsorption and detection module. However, our calculations show that even without a drying step, there are promising candidates with selective adsorption of THC in the presence of water.

3.4 Conclusions

We have conducted Monte Carlo simulations to investigate the adsorption of THC in a database of experimentally-synthesized and proposed structures. In order to increase the efficiency of the screening, we tested a minimal model of THC using only the rigid aromatic head, in addition to a full model of THC with the flexible alkyl tail. We found that using

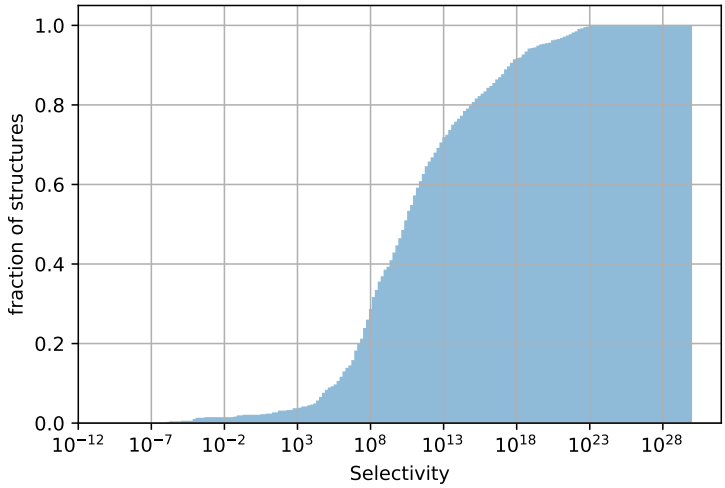

Figure 3.15: Histogram of selectivities of screening library.

only the THC-HEAD model represents a speedup of 3 times over the THC-FULL model, and is a good proxy for the full model in larger pores. In very small pores, it might be necessary to include the tail, as if there is a very favorable binding site for the THC head where the head group fits very tightly within the pore, there might not be space for the tail, and the same site could be an unfavorable binding site for the full THC molecule.

We next introduced a method to evaluate the accessibility of pores in the materials by computing the overlap area between the cross-sectional areas of the THC and the pore limiting channels in the materials. This method could be useful as an addition to the PLD in determining whether an nonspherical probe can percolate through a material or through a selected pore. By screening for the overlap area in our database, we are able to exclude materials within which THC would have limited accessibility.

Within the THC-accessible materials, we identify three motifs of promising materials for THC adsorption: "narrow channels," "thick walls," and "parking spots." These motifs are not mutually exclusive and indeed, some materials exhibit more than one. The "parking spot" motif is perhaps the most interesting for an adsorption and sensing application, as the wide channels allow for fast diffusion and the narrow slits bind the adsorbate strongly and limit rotational and translational motions which can lead to noise in optical sensing.

Finally, we computed the Henry coefficient for water to calculate the THC/H_2O selectivity of our materials. We conducted a simple thermodynamic analysis to estimate that a selectivity of at least 10^{12} would be advantageous for detection of THC directly from humid breath. About 40% of all the THC-accesible materials, and the majority of the most promising materials, fell above this threshold selectivity.

Further investigation is needed to experimentally confirm THC adsorption in the promising materials identified in this study. Moreover, since the goal is to not only adsorb THC but to detect it, experimental and theoretical work can help to identify practicable sensing

technologies that would work with these adsorbents.

This study shows that there are materials with potentially selective and favorable adsorption sites for THC. These materials can be used to develop new sensing pathways or improve existing ones towards the goal of a breath sensor for THC. More broadly, we present strategies that can be used for study of adsorption of large molecules in porous materials, including an algorithm to determine pore accessibility to strongly asymmetric molecules such as THC.

Chapter 4

Amine-Appended MOFs for CO_2 Capture*

4.1 Porous Materials for Carbon Capture

Carbon emissions have grown rapidly in the past decades, causing unprecedented rises in global temperatures.[115] Scenarios for capping temperature rises to 2.0 or even 1.5 °C generally include technologies to reduce emissions from existing sources of CO_2 which are unlikely to be phased out in the next generation. One of the largest single point-source emitters of CO_2 in the United States is coal-fired power plants, representing about a quarter of carbon emissions from the energy sector (Figure 4.1). From these point sources, CO_2 can be separated from the flue gas stream before emission to the environment and then stored in geological reservoirs in a technolgy called carbon capture and sequestration (CCS). Currently, industrial-scale carbon capture uses aqueous amines to absorb CO_2. Aqueous amine scrubbing can achieve excellent separation performance, but could reduce a power plant's efficiency up to 30%[116] and, according to a 2009 study, would cause energy costs to rise up to 86%, rendering amine scrubbing commercially unattractive.[117]

Solid adsorbents represent a more economical alternative, as they require less energy to operate in an adsorption process.[119] In particular, metal-organic frameworks (MOFs) are reported to reduce the parasitic energy of a CCS process by up to 30%.[120] MOFs are a family of solid adsorbents consisting of metal centers joined by organic linkers to form a network with pore diameters on the order of nanometers, meaning they have extremely high internal surface areas. They are chemically tunable and modular, and the possibility of matching

*This chapter is based on [1] Xu, J., Blaakmeer, E. S. M., Lipton, A. S., McDonald, T. M., Liu, Y. M., Smit, B., Long, J. R., Kentgens, A. P. M. & Reimer, J. A. Uncovering the Local Magnesium Environment in the Metal-Organic Framework Mg2(dobpdc) Using 25Mg NMR Spectroscopy. *J. Phys. Chem. C* **121,** 19938–19945. http://pubs.acs.org/doi/abs/10.1021/acs.jpcc.7b07809 (2017) and [2] Xu, J., Liu, Y. M., Lipton, A. S., Ye, J., Milner, P. J., McDonald, T. M., Siegelman, R. L., Forse, A. C., Smit, B., Long, J. R. & Reimer, J. A. Amine Dynamics in Diamine-Appended Mg2(dobpdc) Metal-Organic Frameworks. *Submitted* (2018).

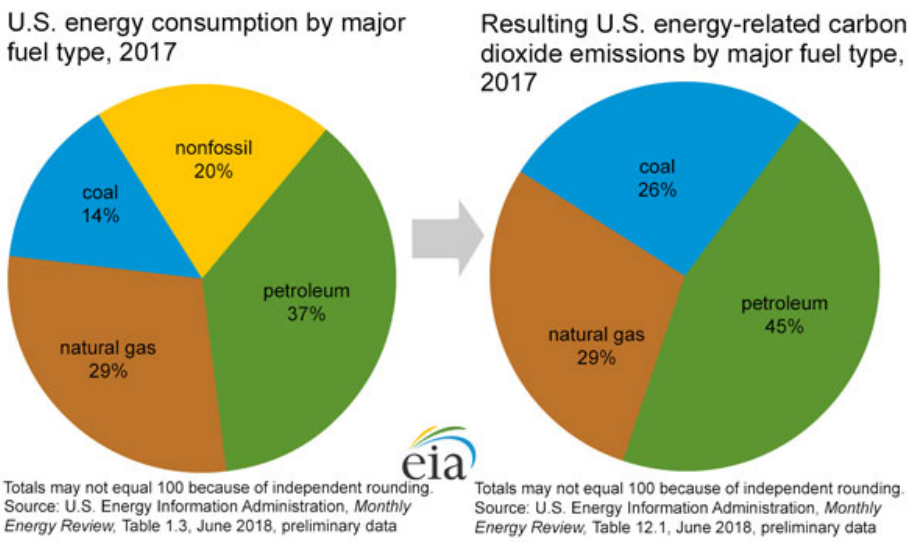

Figure 4.1: US energy consumption and energy-related carbon dioxide emissions by major fuel type, 2017. Figure from Reference [118].

different linkers and metal clusters means that the hypothetical design space MOF structures is combinatorially large, and an optimal MOF can be sought for a particular process such as post-combustion carbon capture.[121]

4.1.1 mmen-Mg_2(dobpdc): A Promising Phase-Change Material

The mmen-Mg_2(dobpdc) MOF (mmen=*N,N'*-dimethylethylenediamine, dobpdc^{4-} = 4,4'-dioxido-3,3'-biphenyldicarboxylate) (Figure 4.2, first reported by McDonald and coworkers in 2012, shows particular promise for its high CO_2/N_2 selectivity, relative water stability, and large working capacity due to a step-shaped isotherm.[122] This isotherm arises because CO_2, rather than adsorbing via physisorption, inserts into the nitrogen-metal bond and forms a carbamate compound with an adjacent free nitrogen. Above a temperature-dependent threshhold of CO_2 concentration, collective insertion of CO_2 in neighboring metal sites leads to formation of a carbamate chain spanning the c-axis of the material. This phase-change adsorption mechanism was discovered in 2015, again by McDonald and coworkers.[123] They showed in the same work that in the absence of CO_2, the mmen functional groups are not statically bonded to the metal sites. Rather, they interconvert faster than the timescale of solid-state ^{15}N NMR, such that only one nitrogen peak appears, indicating that the two nitrogens in mmen appear to be in equivalent chemical environments.

Molecular simulations are useful to study this unique adsorption mechanism and interconversion dynamics of the mmen functional group, as well as other diamine ligands which can be appended to Mg_2(dobpdc) and its expanded analogs. In particular, characterizing the nature of the amine dynamics in the absence of CO_2 can provide insight into design rules

for materials for optimal CO_2 capture performance under different conditions.

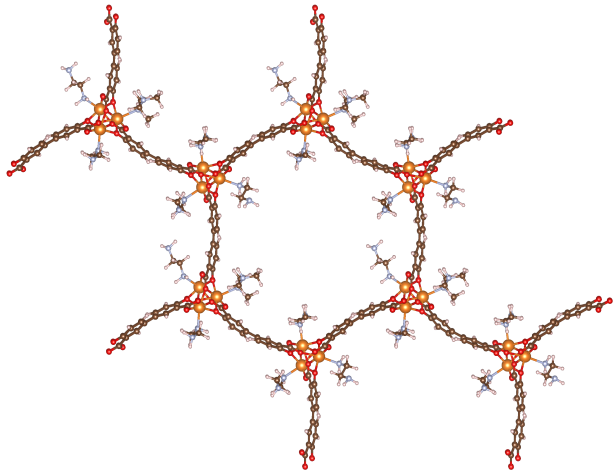

Figure 4.2: Structure of mmen-Mg_2(dobpdc) MOF.

4.2 Methods for Simulation of Amine-Appended MOFs

4.2.1 Reactive Force Field Model of Amine-Appended MOF

A central feature of the amine-appended MOFs is the lability of the coordinate bond between the amine functional groups and the metal nodes. NMR spectroscopy has indicated that for mmen-Mg_2(dobpdc) at timescales relevant for CO_2 capture, there is only one ^{15}N peak corresponding to the functional group *N,N'*-dimethylethylenediamine (mmen). Since only one amine group can be coordinated to the metal while the other is free, the evidence that there is only one chemical environment for ^{15}N suggests that there is an exchange of amine group coordination occuring faster than the timescale of NMR.[27]

Most classical force field models assume that bond networks remain fixed throughout the course of a simulation, which would not be appropriate for this system. On the other end of the spectrum, quantum mechanical methods do not assume a bonding network, but the computational cost of such methods is prohibitive for modeling a system on the length and timescales necessary to study amine functional group dynamics. We therefore turn to reactive force field methods, which incorporate a bond order term in the total energy function of the system, where the bond order is calculated at each timestep based on the pairwise distances between atoms.

Many reactive force field methods exist, some which have been expanded for simulation of a variety of systems, such as ReaxFF,[124,125] and others which are designed for a class of materials, such as REBO and AIREBO for carbon/hydrogen systems.[126,127] We chose the ReaxFF force field method because it has been used widely for both inorganic and organic

systems. In the ReaxFF method the contributions to the potential energy are:

$$U_{system} = U_{bond} + U_{angle} + U_{tors} + U_{conj} + U_{vdWaals} + U_{coulomb}\,, \tag{4.1}$$

where the primary difference from a traditional force fields lies in the bonded term. In a traditional force field, the bonded potential is typically described by a harmonic functional form:

$$E_{bond}^{traditional} = -k(r - r_0)^2\,, \tag{4.2}$$

where r_0 is the equilibrium bond distance and k is the force constant, with units of energy per mol. By contrast, the ReaxFF force field has the following functional form for the bonded potential:

$$E_{bond} = -D_e \cdot BO_{ij} \cdot \exp[p_{be,1}(1 - BO_{ij}^{p_{be_1}})]\,, \tag{4.3}$$

where D_e is the depth of the bonded potential well, BO_{ij} is the bond order calculated by the system, and $p_{be,1}$ is an empirical parameter.

The angle and torsion terms are calculated using harmonic functional forms, as in a traditional force field. The van der Waals interactions are described using a distance-corrected Morse potential and the Coulomb interactions using a shielded Coulomb potential.

The molecular dynamics simulation using the ReaxFF force field is run in the Large Scale Atomic/Molecular Massively Parallel Simulator (LAMMPS), using the built-in implementation of ReaxFF. Charges at every time step are equilibrated using the QEq method of Rappe and Goddard.[128]

4.2.1.1 Force Field Optimization

The ReaxFF parameters are optimized using GARFfield program developed by Andres Jaramillo-Botero.[129] GARFfield takes a training set of geometries with energies calculated by DFT and conducts a genetic algorithm search to match the ReaxFF energies to those calculated using DFT.

The training set used to optimize the Gen 2 force field consisted of a set of unit cell expansions and contractions of the bare Mg_2(dobpdc) MOF (without the diamine functional groups) in order to improve the stability of the framework on its own.

The Gen 3 force field, still under development, uses a training set that comes from a ReaxFF simulation of the entire mmen-Mg_2(dobpdc) MOF using the Gen 2 force field, which allows the amines to adopt different configurations so that the interaction energies between the amines and the framework atoms can be tuned.

4.2.2 DFT Structure Optimization

DFT calculations were performed in the Vienna Ab initio Simulation Package (VASP) to relax atomic positions with the lattice held constant before molecular dynamics simulations. DFT calculations used projector augmented-wave pseudopotentials and Perdew-Burke-Ernzerhof exchange-correlation functionals with a cut-off energy of 550 eV, energy

convergence threshold of 1e-7, and a max force of $0.02\,\mathrm{eV\,\AA^{-1}}$. Relaxation was carried out for a maximum of 100 ionic steps.

4.2.3 Kinetic Analysis of Amine Dynamics

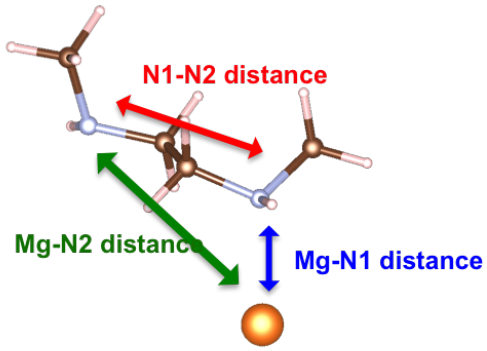

Figure 4.3: Order parameters for analysis of amine interconversion and stability.

Simulations are analyzed for amine interconversion and amine stability using the order parameters described in Figure 4.3.

In the initial configuration of a system, the amine end which is coordinated to the metal is defined as `N1` and the free amine end is defined as `N2`. Thus the `Mg-N1` is initially smaller than the `Mg-N2` distance. An interconversion event is defined when the `Mg-N1` and `Mg-N2` distances swap their relative sizes and remain in such a state for a non-negligible amount of time. An amine may undergo multiple interconversion events.

An amine is characterized to be unstable when the `Mg-N1` and `Mg-N2` distances both begin to increase in tandem, indicating that the amine is no longer coordinated to the metal site. In order to calculate exchange rates, interconversion events were counted for a simulation run and the rate was computed as the number of interconversion events divided by the length of the simulation and the total number of amine groups in the system.

The enthalpy and entropy of activation were calculated by fitting amine exchange rates at different temperatures to the Eyring-Polanyi equation,[130,131]

$$\ln \frac{k}{T} = \frac{-\Delta H_a}{RT} \times \frac{1}{T} + \ln \frac{k_B}{h} + \frac{\Delta S_a}{R}\,. \tag{4.4}$$

By plotting $\ln \frac{k}{T}$ against $\frac{1}{T}$ the enthalpy and entropy can be determined.

4.3 Force Field Optimization and Characterization

Force field parameters were optimized using parameters for CuBTC[125] as a starting point, as it contained parameters for all of the elements in mmen-Mg_2(dobpdc). Using these un-

optimized CuBTC parameters, the simulation of mmen-Mg_2(dobpdc) was unstable, yielding unphysically high forces within the first few steps of simulation. This was a result of undefined Mg-C interactions in the initial force field, as the CuBTC force field was not explicitly designed for materials containing magnesium.

In order to generate a ReaxFF force field usable for mmen-Mg_2(dobpdc), Mg-C bonded interaction parameters were set to the same value as the Cu-C interaction parameters, yielding a first-generation force field for which the total system energy and forces were physically bounded. Simulations of the mmen MOF at physically relevant temperatures show decrease in unit cell volume and pore shape deformations (Figures 4.4a and 4.5a). Up to 600 K, the unit cell volume shrinks approximately 20% within the first 30 ps when initialized from the DFT-optimized structure and equilibrates at 40 000 $Å^3$. At 700 K, the unit cell volume undergoes larger fluctuations while appearing to equilibrate, but around 40 ps the framework ultimately collapses. This collapse coincides with concerted de-coordination of amine groups from the metal nodes.

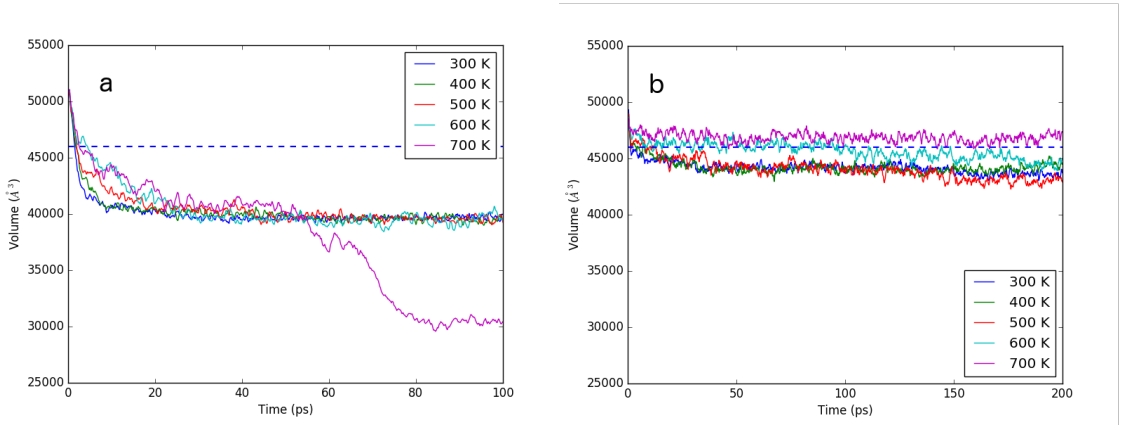

Figure 4.4: Unit cell stability for (a) 1^{st} and (b) 2^{nd} generation force fields. The 1^{st} generation force field shows collapse of the framework at 700 K, while the 2^{nd} generation force field framework is stable at 700 K.

Individual instances of amine separation can be observed at even lower temperatures in the 1^{st} generation force field simulations, starting at 500 K. This is consistent with thermogravimetric analysis data indicating a 32% mass loss between 200 °C and 350 °C, which has been attributed to amine volatilization.[63] The 1^{st} generation force field simulation also displays buckling in the sides of the unit cell (Figure 4.5). Inspection of the simulation reveals that the conformational change resulting from the linker buckling is responsible for the shrinkage in unit cell volume compared to experiment. This degree of buckling is observed neither experimentally nor in *ab initio* molecular dynamics.[132]

These discrepancies between simulated and experimental observations prompted further force field optimization. The second-generation force field was parameterized just using the bare framework (the Mg_2(dobpdc) framework without amines), using a set of unit cell expansions and contractions as the training set and modifying the Mg-Mg, Mg-C, and Mg-O

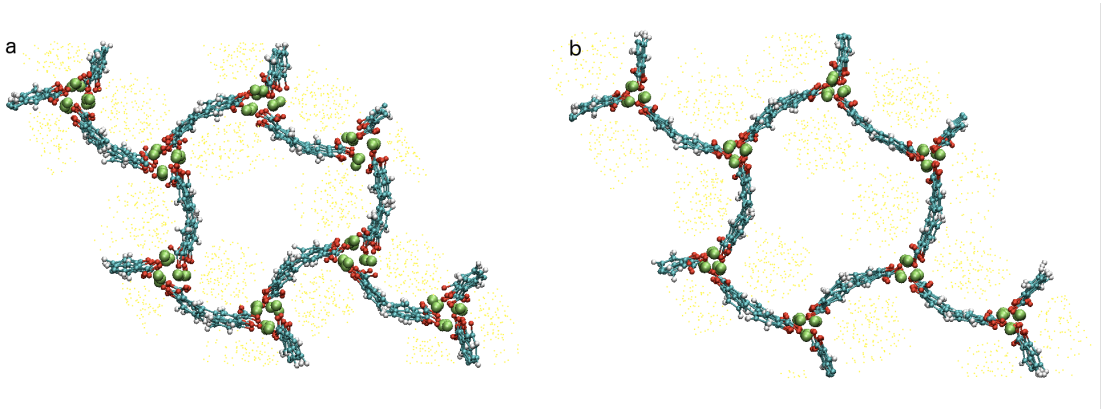

Figure 4.5: Unit cell equilibrium structures for (a) 1^{st} and (b) 2^{nd} generation force fields The 1^{st} generation unit cell is much more buckled than the 2^{nd} generation structure, corresponding to the smaller equilibrium unit cell volume shown in Figure 4.4.

interaction parameters. The optimization used a combined genetic algorithm and conjugate gradient method developed by Jaramillo-Botero.[133]

The unit cell volume of a molecular dynamics simulation using the optimized parameters are shown in Figures 4.4b and 4.5b. With the 2^{nd} generation force field, the linkers buckle less and the equilibrium volume of the MD simulation is within 10% of the experimentally measured value. However, significant amine detachment is visible even at 300 K, and by 600 K–700 K, almost all of the amines are fully detached from the framework. It is believed that the amines are more mobile because the framework shape is more open than the first generation force field. The excessive amine mobility indicates that further force field optimization must focus on tuning the interaction strength between Mg and N atoms.

For subsequent analysis, the 1^{st} generation force field was used rather than the optimized 2^{nd} generation force field. Though the 1^{st} generation force field displays larger deviations in structure and volume from experimental observations, the relative stability of the amine functional groups makes it a better candidate to study amine dynamics.

4.4 Amine Exchange in mmen-Mg_2(dobpdc)

4.4.1 Observing Amine Interconversion

The following amine interconversion analysis is done using the first generation force field. Figure 4.6 shows the intra-mmen distances for two functional groups selected from a simulation at 500 K. In the figure with no interconversion, all three distances remain close to their DFT-optimized values (horizontal lines). In the figure with interconversion, fluctuations in the N1-N2 distance precede the crossing of the Mg-N1 and Mg-N2 distances. This indicates that mmen first buckles, bringing both nitrogens roughly equidistant from the metal site, before switching the nitrogen bound to Mg. These steps are shown in Figure 4.7.

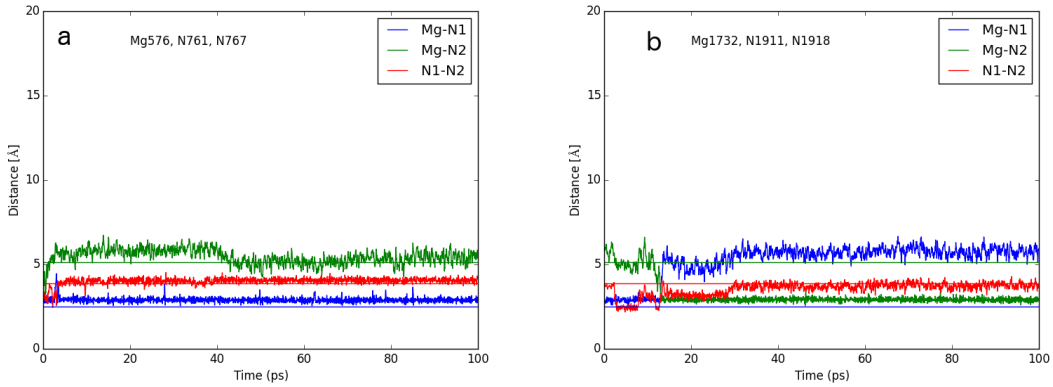

Figure 4.6: Diamine interconversion examples, where the colors correspond to Figure 4.3. a, no interconversion, and b, interconversion can be observed.

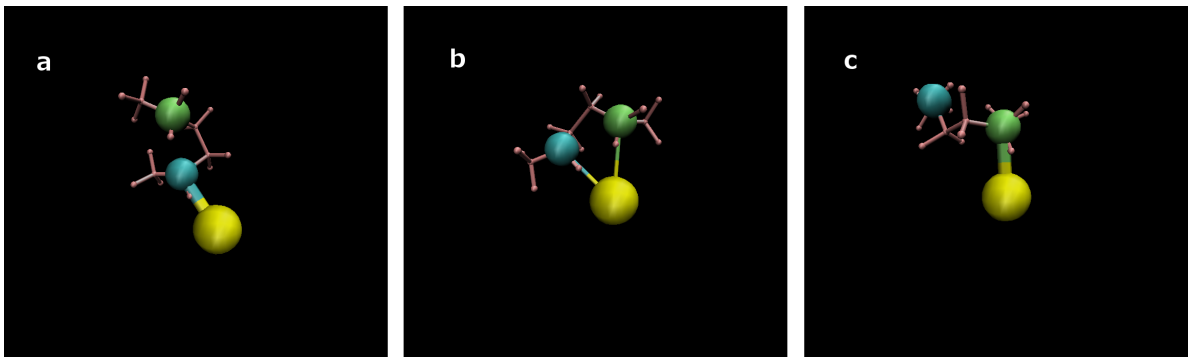

Figure 4.7: Still frames (a) before conversion, (b) during a hypothesized transition state, and (c) after amine interconversion. During the transition state, the amine is buckled (as reflected by fluctuations in its N1-N2 distance in Figure 4.3) and both nitrogens appear 4 Å from the Mg atom. In the initial and final structures, the nitrogens bound to the Mg atom are below 3 Å away.

These results suggest that one mmen "hopping" on the same Mg atom is one of the contributors to the mobility of the amines seen via NMR. It does not rule out amines "rocking" between neighboring metal sites, however. In fact, there is evidence from simulation that this may happen as well, as we can observe that some mmen molecules migrate away from their initial metal site entirely (Figure 4.8).

4.4.2 Interconversion Rate and Activation Energy

The activation enthalpy and entropy for mmen interconversion are $(5.4 \pm 1.3)\,\mathrm{kJ\,mol^{-1}}$ and $(-57.4 \pm 4.2)\,\mathrm{J\,mol^{-1}\,K^{-1}}$, respectively, where the error represents a 95% confidence interval). The enthalpy and entropy measured via NMR by experimental collaborators are

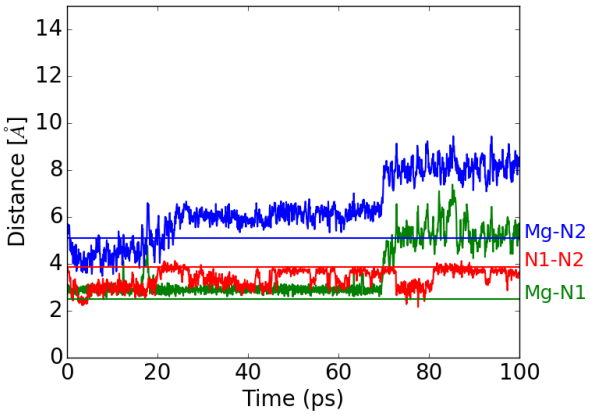

Figure 4.8: Example of an mmen that may be moving away from the initial metal site. The N1-N2 distance is remaining roughly constant, indicating the mmen is staying int act, but the distance between both nitrogens and the Mg is increasing.

$3.6\,\mathrm{kJ\,mol^{-1}}$ and $-82\,\mathrm{J\,mol^{-1}\,K^{-1}}$ (uncertainty values not provided). The simulated and measured activation enthalpies are close to within the uncertainty range. However, the activation entropies are very different, indicating that while the rates scale similarly with temperature, the simulated reaction rate is orders of magnitude larger than the experimental reaction rate according to the Eyring-Polanyi equation (Equation 4.4).

The difference in activation entropy for mmen is attributed to the excess mobility of the simulated framework as compared to the experimental system. As noted, the 1^{st} generation force field allows for a notable deformation of the pore volume and shape while the system is equilibrating, and in the equilibrated system there is dynamic buckling of the linkers, changing the coordination environment around the metal nodes. This altered coordination environment appears to make the activated state of the "hopping" interconversion more entropically favored in simulation compared to experiment.

In both simulation and experiment, however, the transition state has lower entropy than either the reactant and product state. This supports the proposed reaction mechanasm as involving a transition state where both ends of the diamine are coordinated to the metal, and therefore have restricted mobility compared to when one amine end is "free." The closeness in values of the activation enthalpy also suggests that the activation complex observed in simulation is the same as seen in experiment.

Name	Structure
ethylenediamine	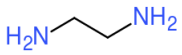
N,N'-dimethylethylenediamine	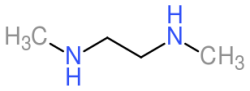
methylethylethylenediamine	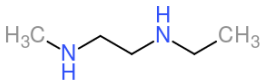
N,N'-diethylethylenediamine	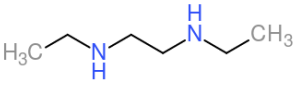

Table 4.1: Molecular structures of amine group analogs.

4.5 Comparison of Functional Group Dynamics in Amine-Appended MOF Analogs

The mobility of the amine groups is an important property influencing CO_2 adsorption, since CO_2 molecules must insert into the metal-amine bond to adsorb at saturation. If the amine groups interchange more quickly, that might make it easier for CO_2 to insert in the coordination bond. On the contrary, if there is little or no interconversion, it might be because the amine groups are sterically hindered from "hopping." This steric hindrance could also make the barrier for CO_2 adsorption higher, and perhaps push the temperatures and pressures at which the CO_2 adsorption step takes place to lower and higher values, respectively.

In order to study the amine group dynamics for different amines, we made the structures *in silico* and relaxed with DFT as described. In addition to mmen, three additional amines were simulated: ethylenediamine, methylethylethylenediamine, and *N,N'*-diethylethylenediamine, shown in Table 4.1. The same simulation protocol was used as for mmen to measure the simulated rates of reaction at different temperatures and extract the enthalpies and entropies of activation.

The computed energies of activation are provided in Table 4.2. The only amine for which an enthalpy and entropy of activation could not be calculated was ethylenediamine, the only primary-primary diamine (meaning that the amine ends have no appended alkyl groups). When the ethylenediamine-appended MOF was simulated, the ethylenediamine groups virtually all detached from the metal nodes. In NMR experiments carried out by collaborators, loss of diamine was also observed.

In the remaining two amines, methylethylethylenediamine (henceforward methylethyl) and N,N'-diethylethylenediamine (diethyl), the methyl end groups of mmen were changed,

Table 4.2: Enthalpies and entropies of activation for interconversion of amine-appended MOF analogs. Experimental values were measured by Jun Xu in the Jeff Reimer group at Berkeley.

Diamine	ΔH_a expt ($\mathrm{kJ\,mol^{-1}}$)	ΔS_a sim ($\mathrm{J\,mol^{-1}\,K^{-1}}$)	ΔH_a expt ($\mathrm{kJ\,mol^{-1}}$)	ΔS_a expt ($\mathrm{J\,mol^{-1}\,K^{-1}}$)
N,N'-dimethylethylenediamine	5.4 ± 1.3	-57.4 ± 4.2	3.6	-82
ethylenediamine	unstable	—	unstable	—
methylethylethylenediamine	6.7 ± 0.9	-54.7 ± 3.0	—	—
N,N'-diethylethylenediamine	8.0 ± 1.2	-48.4 ± 3.8	7.4	-65

one at a time, into ethyl groups, to increase the steric hindrance around the amine tails. As the steric hindrance increased, from mmen to methylethyl to diethyl, the enthalpy of conversion computed from simulation also increased from (5.4 ± 1.3) to (6.7 ± 0.9) to $(8.0 \pm 1.2)\,\mathrm{kJ\,mol^{-1}}$, respectively, while the entropy of conversion decreased from (-57.4 ± 4.2) to (-54.7 ± 3.0) to $(-48.4 \pm 3.8)\,\mathrm{J\,mol^{-1}\,K^{-1}}$, respectively.

The increasing activation enthalpy is due to the steric hindrance of the increasingly bulky alkyl end groups in the interconversion transition state. Since both amine groups need to be coordinated to the metal node during the transition state, the larger alkyl groups make this configuration more energetically unfavorable. The decreasing activation entropy could reflect the fact that in the reactant/product states (which are the same for symmetric amines), bulkier amines already have somewhat restricted mobility since the adjacent ethyl groups along the metal rod crowd each other. In the transition state, more sterically hindered molecules should also have lower entropy, but the loss of entropy in the non-transition states are larger than in the transition state, making the ΔS_a smaller.

4.6 Local Structure Around ^{25}Mg

Molecular dynamics simulations were also used in conjunction with NMR experiments performed by a collaborator to verify that the local structure around the Mg centers in mmen-Mg_2(dobpdc) is deformed with respect to the bare Mg_2(dobpdc) MOF, in order to explain the distribution in ^{25}Mg NMR parameters when mmen is coordinated to the MOF.[113]

Snapshots from molecular dynamics simulations were used to calculate the ^{25}Mg NMR parameters as a function of time over 50 ps. These NMR parameters can be found in the Electronic Supporting Information of Xu *et al.*[113] and vary between different Mg sites at a single point in time, and for individual Mg sites over time.

The reason for this distribution in NMR parameters is thought to be the motion in the amine groups. Simulations show that at experimentally relevant temperatures, amine molecules are mobile within the MOF channels. These amine motions are thought to sterically stabilize more bending fluctuations in the linkers than is present in the bare MOF,

and these dynamic motions of the linker result in a dynamic pore deformation and resulting distribution of NMR parameters.

A movie of the dynamic framework deformation can be found online in the published work.[113]

4.7 Conclusions

In conclusion, we were able to make a reactive force field to model mmen-Mg_2(dobpdc). The 1^{st} generation force field displayed some phenomena inconsistent with experimental observations, namely large deformations of the MOF pore shape. Optimization of the force field using a genetic algorithm/conjugate gradient method resulted in a pore shape more similar to that observed experimentally, however, the 2^{nd} generation force field exhibited concerted de-coordination of the amine groups. In order to study the dynamics of amine motion inside the amine-appended MOF, the 1^{st} generation force field was used.

Using this force field, we were able to observe a mechanism for amine interconversion via "hopping," or exchanging of the amine end coordinated to the metal site. Enthalpic and entropic barriers to this hopping interconversion were computed and compared to experimental values. The enthalpy of activation for interconversion was close to the experimentally measured value, supporting the hypothesis that the hopping mechanism explains the equivalent amine environments seen in NMR experiments.[123] The simulated activation entropy was further away from the experimentally measured ΔS_a. This is attributed to the aforementioned unrealistic pore shape deformation, which causes a shift in the activation entropy because the dynamically deformed pore shape results in more disorder in the transition state structure than if the pore was more rigid.

Diamine mobility was also studied for three other amine analoggs: ethylenediamine, methylethylethylenediamine, and *N,N'*-diethylethylenediamine, all appended in the same Mg_2(dobpdc) framework. The ethylenediamine simulation was not usable for calculation of activation enthalpy and entropy because the ethylenediamine molecules were very labile, detaching from the framework almost immediately after the start of framework equilibration. This is consistent with experiments conducted by collaborators, where the ethylenediamine-appended frameworks were shown to experience mass loss associated with volatilization of ethylenediamine from the framework.

For methylethyl- and *N,N'*-diethyl diamines, which are increasing in steric hindrance from mmen, the activation enthalpy increased and the activation entropy decreased with increasing bulkiness of alkyl end groups. This is consistent with experimental observations, further confirming the appropriateness of the 1^{st} generation force field for studying diamine mobility. These trends provide insights into tuning diamine structure to modify CO_2 adsorption step temperature and pressure for different carbon capture conditions.

Finally, snapshots from molecular dynamics simulations were used to calculate NMR parameters to confirm experimental observations that in the mmen-appended MOFs, the Mg groups exhibit a distribution of NMR parameters corresponding to loss of symmetry of

the environment around ^{25}Mg. The simulations showed that different Mg sites experience different environments from each other at a single point in time, and changing environments as a function of time, due to the dynamics and mobility of the amine groups, which promote fluctuations in the shape of the MOF pore via linker buckling.[113]

Chapter 5

Zeolite-Templated Carbon Electrical Double-Layer Capacitors*

5.1 Introduction

Energy storage is becoming ever more important as society moves away from fossil fuels toward a cleaner energy paradigm. Storage technologies are often compared using the high-level metrics of energy density and power density. Batteries have relatively high energy density and low power density, while traditional capacitors have high power density and low energy density.[135,136] One advantage of capacitors is that, since they store energy through electric charge, they do not degrade as easily as batteries, which store energy through a chemical reaction. Capacitors are thus able to provide millions of charge-discharge cycles, versus several thousand cycles for the best-performing batteries.[31] Motivation to increase the energy density of capacitors has spurred the development in the past few decades of a new type of capacitor, called the electrical double layer capacitor (EDLC), or supercapacitor. EDLCs are differentiated from traditional capacitors by having a liquid electrolyte in place of a solid dielectric. Under an applied voltage, the accumulation of positive and negative ions at the anode and cathode, respectively, leads to the creation of a double layer at each electrode.

The energy density of a capacitor is expressed as capacitance, defined as the amount of charge, Q, stored by a capacitor at a given voltage, V:[31]

$$C = \frac{Q}{V}\,. \tag{5.1}$$

For an idealized parallel plate capacitor consisting of metallic electrodes enclosing a dielectric medium of uniform dielectric constant, ε, the capacitance can be derived exactly as

$$C = \varepsilon A/d\,, \tag{5.2}$$

*This chapter is based on Liu, Y. M., Merlet, C. & Smit, B. Mechanisms of Charge Storage in Zeolite-Templated Carbon Supercapacitors. *Submitted* (2019).

where A is the cross-sectional area of the capacitor and d is the separation distance between the electrodes. If we transpose this expression to an EDLC, A would be the surface area of the electrode which is accessible to electrolyte ions, and d the characteristic thickness of the electrode-electrolyte interface. Equation 5.2 provides some intuition for why EDLCs have increased capacitance over their traditional counterparts: First, the charge separation distance is smaller in an EDLC than in a traditional capacitor, since ions can approach within less than 0.5 nm of the electrode surface, while in a traditional capacitor d is a few nanometers or higher.[31,137] Second, the accessible surface area of an EDLC can be increased by several orders of magnitude using rough or porous electrode.

Multiple theories have arisen to describe the electrochemical double layer, beginning with the classical theory of Helmoltz,[138,139] which was subsequently improved by Gouy,[140] Chapman,[141] and Stern[142] to consider discrete ions and complex double layer structures. These theories can accurately predict capacitances of EDLCs whose pores are macroscopic. However, when the pores become comparable in size to the electrolyte ions, so-called "anomalously" high capacitances have been observed that break with both existing theories and empirical trends.[143,144] Reports of materials with such impressive capacitances have led to considerable growth in the field of microporous materials for EDLCs, to better understand the mechanisms behind capacitance in small pores.[8,145–150]

A popular choice of material for EDLC electrodes is porous carbon, due to its stability, ease of synthesis, and low cost. Porous carbons used in EDLCs include activated carbons,[144] carbide-derived carbons,[143,151] carbon onions and nanotubes,[152] carbonized precursors such as metal-organic frameworks,[32] and graphene-based composites.[9,153] Experiments and simulations have shed some light on the charge-storage mechanisms in such materials;[8,147,148,154,155] however, a major challenge is that most microporous carbon materials have neither a well-defined porosity nor long-range order, making it difficult to draw conclusions between structure and performance.

A new class of materials called zeolite-templated carbons (ZTCs), which are synthesized using a sacrificial zeolite scaffold,[7,22] has been demonstrated as a promising EDLC material.[156,157] Thus far ZTCs have been synthesized from just three zeolites (FAU, EMT, and beta) of the 245 frameworks recognized by the IZA Structure Commission.[16] Recently, Braun and coworkers reported a method to computationally synthesize ZTCs from a given zeolite structure.[158] Their predicted ZTCs are composed of sp^2-hybridized carbons which tile a surface that is dual to the zeolite. Templating on a crystalline framework confers well-defined pore geometries which could yield insights into the structure-property relationships of electrode materials, motivating further study of ZTCs for energy storage applications.

In this work we use molecular dynamics (MD) simulations to screen the ZTC materials of Braun *et al.* as electrode materials in EDLC cells. We show that the charging timescale of the ZTCs is negatively correlated with pore limiting diameter, and that there is evidence of both progressive charge penetration and kinetic trapping within the ZTCs during charging. We then study the equilibrium capacitance of the ZTCs to investigate the correlation between geometric descriptors, local electrolyte configurations, and charge storage mechanisms within the electrode. Introducing the concept of charge compensation per carbon (CCpC), We find

that charge storage is more efficient at ion adsorption sites with high CCpC, which are more likely within pores with a lower radius of curvature. Conversely, charge storage is diminished at high-radius-of-curvature sites and within sites with a mismatch of local pore diameter and ion size.

5.2 Methods

5.2.1 Model and Force Field

In our simulations we used an organic electrolyte composed of a mixture of 1-butyl-3-methylimidazolium tetrafluoroborate ($[BMI^+][BF_4^-]$) and acetonitrile (ACN) with the concentration of ions equal to 1 M. We modeled the organic electrolyte using a coarse-grained description consisting of a three-site model for BMI^+ and ACN, and a single-site model for BF_4^-, as shown in Supplementary Figure C.1. Non-bonded interactions were described by a pairwise Lennard-Jones potential with Lorentz-Berthelot mixing rules, and electrostatic interactions by a Coulombic potential.

For the non-bonded parameters of BMI^+ we used those developed by Roy and Maroncelli.[159] The non-bonded parameters for BF_4^- and ACN were taken from Merlet *et al.*[8] and from Edwards *et al.*[160] respectively. Bonds and angles of BMI^+, and bonds of ACN, were kept rigid using the SHAKE algorithm.[161,162] For the angles of ACN we used a harmonic potential with a stiff spring constant of $400\,\mathrm{kcal^2\,rad^{-1}\,mol^{-1}}$ to keep the molecule close to linear. The carbon atoms of the electrodes were modeled as rigid. During the constant applied potential simulations, the charges of the electrode atoms were computed at each timestep according to the constant-potential method.[163,164] All force field parameters and further details regarding the constant-potential method are provided in the Supporting Information.

ZTC materials were synthesized *in silico* as described in Braun, *et al.*[158] Carbide-derived carbon (CDC) materials, which are studied in depth computationally by Merlet and coworkers,[8,165] are used here as a reference material. CDC structures were taken from Palmer *et al.*,[166] who generated them using Quench Molecular Dynamics. In this work, we consider 27 ZTC and 2 CDC materials for the constant-charge simulations and a subset of 19 of the ZTCs for constant-potential simulations. CDCs are named as in the original article by Palmer *et al.* ZTCs are referred to using the name of the templating zeolite. We indicate hypothetical zeolites using the prefix "h" and the last 2 digits of their 7-digit identifier (*e.g.*, h37 for h8326837). Complete names for all the zeolites referenced in the text can be found in the Supporting Information, along with information on framework properties (pore size, void fraction, accessible surface area).

We used a semi-automated protocol to build two-electrode EDLC cells using the Zeo++ software suite[90] and the VMD script interface with the TopoTools package.[167,168] Further details are provided in the Supporting Information. This protocol was designed to fill the EDLC cell with an amount of electrolyte such that when the capacitor is equilibrated at either constant-charge or constant-voltage, the electrolyte density and composition in the

bulk region matches the experimental values. We present these results in a later section. An example of the simulation setup for FAU_1 ZTC is provided in Figure 5.1.

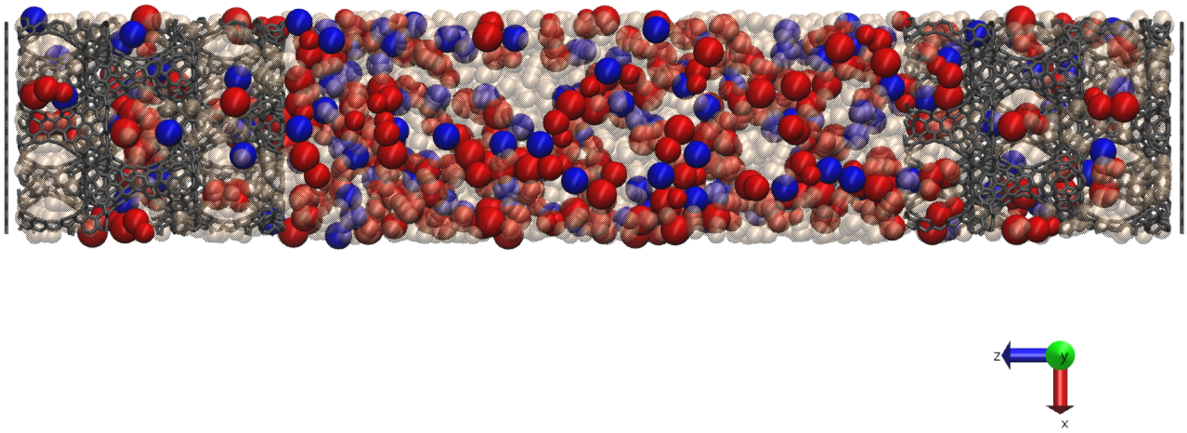

Figure 5.1: Example of simulation setup for FAU_1, with box lengths a=34.4 Å, b =30.7 Å, and c=194.2 Å. BMI^+ ions are in red, BF_4^- ions in blue, and ACN molecules in tan and translucent. The ZTC electrode and graphene caps are in gray. The length of the electrodes in the z direction is 43.4 Å and they are separated by 106.6 Å. Graphene sheets cap the electrodes on both sides of the capacitor cell. The electrolyte consists of 144 $[BMI^+][BF_4^-]$ ion pairs and 1344 ACN molecules. In total, the system contains 9072 atoms.

5.2.2 Molecular Dynamics Simulations

MD simulations were done using the LAMMPS simulation package[169] with Velocity-Verlet time integration using a time step of 1 fs, and a Nosé-Hoover thermostat[170] to maintain a temperature of 300 K. The initial EDLC cell was equilibrated with a constant charge of 0 e on each carbon atom for 4 ns. Final configurations from the zero-charge simulations were used to initialize all further simulation steps.

Molecular simulation is a powerful tool to study EDLCs, as it allows for precise determination of the microscopic properties, such as the structure of the electrolyte within the pores, which can be difficult to access experimentally but which play an important role in determining the capacitance of the material.[8,146] At the same time, simulation of EDLCs presents technical challenges due to long equilibration times[171] and the need to compute the fluctuating charges in the electrode in response to a constant applied potential. The constant potential approach is more accurate but also much more computationally expensive than simulating an EDLC with constant charges on the electrode atoms.[172,173]

We tested multiple protocols for equilibrating the simulation cells, one with a constant-charge equilibration followed by a short constant-potential equilibration step,[8] and the other with a long constant-potential equilibration. In the constant-charge equilibration method,

partial charges of $\pm 0.01\,e$ were applied to all the electrode atoms, positive charges for anode atoms and negative charges for cathode atoms. The EDLC cell was equilibrated with these fixed charges for 8 ns. Then, the effective potential across the cell was calculated using either the 1-D Poisson equation or using the averaged local potentials at each electrode atom, and this potential was applied for the constant-potential equilibration and production runs.

In the constant-potential equilibration, a constant potential difference of 1 V was applied across the EDLC cell (± 0.5 V for each electrode), and the constant potential simulation was run for at least 10 ns. During the constant-potential run, the average absolute charge on the electrodes was monitored and fit to an exponential. The equilibration step was considered completed when the simulation was at least as long as 5τ, where τ is the time constant of the exponential. This equilibration process was found to be the best following a number of tests which are described in the next section, "Development of Computational Protocol".

Production runs for simulation of capacitance were carried out after equilibration at constant potential. The length of production runs was at least 2 ns. Capacitance was computed using Equation 5.1, where $V = \Delta\Psi$ is the voltage drop applied across the cell, and Q is the average absolute value of the charge stored on a single electrode. From the production run we also computed local properties of interest using an in-house software package developed for this study,[174] such as the degree of confinement (DoC)[147] and the charge compensation per carbon (CCpC), in order to understand the mechanisms of charge storage and gain physical insights into differences in capacitances between the materials. The definitions of these local properties are provided in the Supporting Information.

5.2.3 Development of Computational Protocol

5.2.3.1 Pore Filling and Bulk Density

Because the EDLC is simulated at constant volume and number of particles, it is important to check that the loading of electrolyte during cell assembly yields the correct bulk density when equilibrated. We computed a density of $0.926\,\mathrm{g\,cm^{-3}}$ for a box of pure 1 M $[BMI^+][BF_4^-]$ in ACN in the NPT ensemble at 300 K and 1 atm. Within the EDLC, the average density for the bulk electrolyte region was $(0.921 \pm 0.001)\,\mathrm{g\,cm^{-3}}$, computed from the bulk region between the electrodes and excluding a layer of 15 Å on either side from the electrode-bulk interface. The "fill fraction" of the pore volume, described as the ratio of the electrolyte density inside the pore (normalized by void fraction) to the bulk density, was on average 96.8%. Histograms of bulk densities and fill fractions across ZTC materials are in the Supporting Information.

5.2.3.2 Poisson Potential from Constant-Charge Simulation

The constant-potential scheme developed provides a way to treat charges of a metallic electrode and has been demonstrated to yield more physically realistic solvent and ion density profiles in simulating EDLCs.[164,173] However, constant-potential simulations require an order of magnitude longer computational time per step compared to constant-charge simulations,

as at each step the partial charges on each electrode atom must be updated to maintain the same potential at each atom as the electrolyte configuration evolves. To decrease equilibration times, we adopted the procedure used by Merlet *et al.*[8] to "pre-equilibrate" the EDLC at a constant charge. During the constant-charge step, we set the charges of the positive electrode (anode) to $0.01\,e$ and the charges of the negative electrode (cathode) to $-0.01\,e$. We then computed the 1-D Poisson potential across the EDLC from this constant-charge simulation to estimate the potential difference to apply in a constant-potential simulation to obtain the same charge. The Poisson potential is calculated following

$$\Psi_{Poisson}(z) = \Psi(z_0) - \frac{1}{\varepsilon_0}\int_{z_0}^{z} dz' \int_{-\infty}^{z'} dz'' \rho_q(z'')\,, \tag{5.3}$$

where z_0 is a reference point inside the positive electrode with $\Psi(z_0) = \Psi^+$ and $\rho_q(z)$ is the charge density across the cell, which includes the contributions from the electrolyte molecules and the electrode atoms.

We equilibrated the EDLCs at constant-charge for 8 ns and used the final configurations as starting configurations for the constant-potential production runs. We emphasize here that we ran these simulations for a much longer time than the 0.2 ns of constant-charge equilibration used by Merlet *et al.*[8] We believe that the longer constant-charge equilibration was necessary because of the slow electrolyte diffusion in the ZTC materials. Because the ZTC materials are perfectly crystalline, they have a more uniform distribution of small pores and lack the large cavities or channels present in the CDCs. This limits the diffusion rates of the bulky ion molecules (particularly of BMI^+) through the pores of the ZTCs. An example of Poisson potential profile, obtained for FAU_1, is given in Supplementary Figure C.4, where the Poisson potential is shown to be converged after 8 ns of constant-charge simulation.

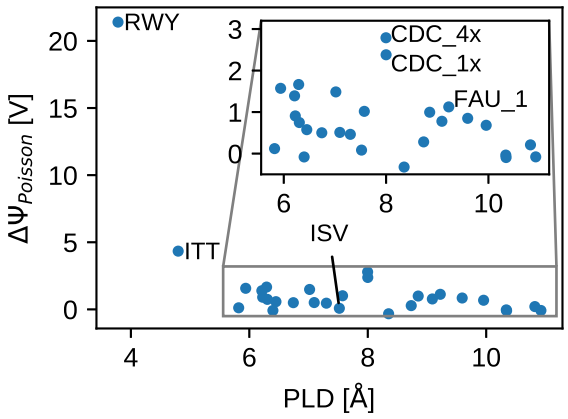

Figure 5.2: 1-D Poisson potential differences from negative to positive electrode of EDLCs, simulated with a constant charge of $\pm 0.01\,e$ per carbon atom. Materials mentioned in the text are labeled for reference.

The Poisson potential drops for 29 EDLCs (27 ZTC EDLCs and 2 CDC EDLCs) are shown in Figure 5.2. Values of the Poisson potential drops range from 0.084 V (ISV) to 21.4 V (RWY) for positive potentials, while 5 ZTCs have negative Poisson potentials. All computed Poisson potentials are provided in the Supporting Information. If the Poisson potential drop were an adequate measure of the real potential difference in a constant-charge simulation, we would get the same average charge ($\pm 0.01\,e$ per atom) on the electrode if the Poisson potential were applied in a constant-potential simulation. Such an assumption would imply a difference of three orders of magnitude in the gravimetric capacitances of the ZTCs studied, between the highest capacitance of $1000\,\mathrm{F\,g^{-1}}$ for ISV, and the lowest capacitance of $3.75\,\mathrm{F\,g^{-1}}$ for RWY. Moreover, the negative potential drop would imply negative capacitances which is obviously not realistic. We note here that the limitation of the Poisson potential to accurately determine the potential drop was already described in the work of Péan *et al.*[175] Indeed, the lack of symmetry (no translational invariance along the x and y axes) and the presence of ions inside the pores imply that there is no obvious reference potential for the integration of the charge density (*cf.* Equation 5.3 and Supplementary Figure C.4b).

It remains possible that the Poisson potential, while not equal to the equivalent potential at constant charge, could still be a good proxy, and the negative values could be due to a too large noise in EDLCs with very low capacitances. To test this possibility, we ran constant-potential simulations using the equilibrated constant-charge EDLC as a starting configuration. Here, we describe results for the FAU_1. Results for other ZTCs are provided in the Supporting Information. For FAU_1, the Poisson potential computed from 8 ns of constant-charge simulation was 1.06 V, so this is the potential we apply in the constant-potential simulation. The number of ions in each of the electrodes as a function of time is shown in Supplementary Figure C.5.

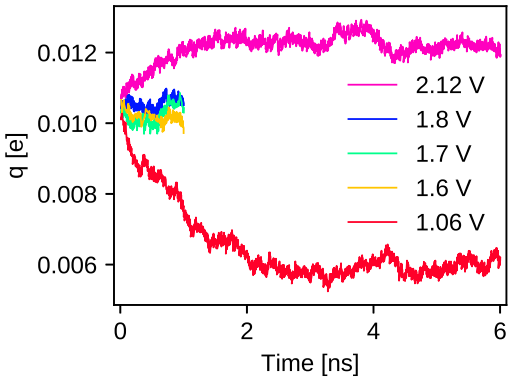

Figure 5.3: Average charge per atom in constant-potential simulations of FAU_1 at various applied voltages, started from the same $\pm 0.01\,e$ constant-charge equilibrated structure.

The FAU_1 EDLC initially had an excess ionic charge of $25\,e$ in the cathode, and an equal in magnitude, opposite in sign, excess charge of anions in the anode. After equilibration,

the magnitude of excess ionic charge in each electrode is about 16 e. This represents a decrease of about 36% in charge stored in the electrode, since the electrode's net charge always balances the excess charge of ions inside the electrode. This discharging shows that in the FAU_1 EDLC, the Poisson potential is not the potential we should apply to obtain the charge equivalent to the constant-charge simulation.

To assess the actual potential we need to apply to obtain an average atom charge of $\pm 0.01\,e$, we try several potential differences and follow the evolution of the total electrode charge as a function of time (see Figure 5.3). We found that this "0.01 e–equivalent" voltage is approximately 1.6 V. A longer simulation would be needed to determine the exact voltage to higher precision. Moreover, we were surprised to see that even when the change in equilibrium charge is small, equilibration at constant potential from a "nearby" constant-charge configuration still takes several nanoseconds. We believe this is due to two factors: First, the driving force for ions to diffuse in and out of the electrodes is proportional to how far away the EDLC is from equilibrium charge, leading to exponential convergence at constant potential. Second, the configuration of ions in the electrode is not only a function of the total charge in the electrode, but also depends sensitively on the distribution of this charge among the atoms of the electrode. Rearrangement of ions can take on the order of nanoseconds due to diffusive limitations in liquid that are exacerbated by the bulky size of the ions and the small pores of the ZTCs, which at their narrowest points have diameters similar to the ion sizes.

The same type of investigation was done for a number of other ZTCs and gives similar results. After switching to a constant-potential simulation using the Poisson potential drop, the resulting equilibrium electrode charges differed from the initial constant charges by 50–200% (see Supporting Information). Following this extensive study, we thus conclude that the approach of doing a constant-charge equilibration associated with a Poisson potential calculation is not suitable for the current work. For the constant-charge equilibration to still be interesting, we would need a better way to estimate the potential difference to apply in the constant-potential simulation.

5.2.3.3 Local Electrostatic Potential from Constant-Charge Simulations

In an attempt to improve the determination of the potential difference corresponding to a particular amount of charge stored, we turned to the calculation of the three-dimensional electric potential field as described in Wang *et al.*[176] We used the software package developed by the authors for constant potential simulations in a previous work,[173] which implicitly computes the electrostatic potential at the position of each electrode atom in order to determine fluctuating charges. We adapted the code to the case of a constant-charge simulation in which the electrostatic potential of each electrode atom fluctuates.

The electrostatic potential averaged over all the atoms in each electrode during a constant-charge simulation was computed for 5 ZTC and 2 CDC materials and results are shown in Table 5.1. For almost all materials, the potential drop computed from the averaged local electrostatic potential appears to have no correlation with the Poisson potential one. For

materials which had extremely low or negative capacitances, such as the ZTCs 221_2_6 and SAO, the average local potential drop was approximately 2 V. For FAU_1, where 1.06 V (computed from the 1-D Poisson potential) was too low to store a charge of $\pm 0.01\,e$ per atom, the local potential method computed a potential drop of 2.3 V for the $\pm 0.01\,e$ constant-charge simulation. This is too high compared to the "$0.01\,e$–equivalent" potential of 1.6 V determined in Figure 5.3.

calculation method:	Local electrostatic potential			1-D Poisson potential
Material	$\Psi_{cathode}$	Ψ_{anode}	$\Delta\Psi$	$\Delta\Psi$
CDC_1x	-0.893	0.559	1.452	2.38
CDC_4x	-1.965	1.231	3.196	2.79
221_2_6	-1.098	0.916	2.014	-0.045
BEA_beta	-0.904	0.856	1.760	0.595
BEC	-0.723	0.760	1.482	0.561
FAU_1	-1.022	1.292	2.314	1.06
SAO	-0.951	0.973	1.924	0.208

Table 5.1: Electrostatic potential, Ψ (in volts), computed using the local electrostatic potential and 1-D Poisson potential methods.

It seems therefore that while the local electrostatic potential method does not, unlike the Poisson potential method, yield physically unrealistic values such as near-zero and negative potentials drops across the cell, the potential drops computed by the local potential method are still not accurate enough to be useful for significantly decreasing the time needed to converge the electrode charge in a constant-potential simulation.

Our initial motivation for calculating the Poisson potential or averaged local potential from a constant-charge simulation was to reduce the time needed for charges on the electrodes to converge in a constant-potential simulation. However, we found that these proxy potentials were not representative of what the applied potential should be to obtain the same amount of stored charge, and the simulation times required for the charge convergence following the constant-charge equilibration were still more than a few nanoseconds. Moving forward, we thus opted to compute constant-potential properties such as capacitance and electrolyte configuration by skipping the constant-charge equilibration step, and directly applying a potential difference of 1 V to the EDLC. The results of these simulations are detailed in the remainder of this article. In the constant-potential production runs, we excluded materials for which the EDLC simulation cell had more than 12 000 atoms. These larger cells could not be studied due to computational limitations affecting the memory-intensive constant potential method.

5.3 Results and Discussion

As demonstrated in the Methods section, we determined suitable protocols for building an EDLC simulation cell and tested different MD equilibration schemes. Here we present the results of our simulations using the constant-potential method for charge equilibration, discussing first the dynamics of charging and then equilibrium capacitances.

5.3.1 Charging Dynamics

An EDLC cell can be represented macroscopically with an equivalent circuit model,[31] which can range in complexity from an RC circuit, consisting of a capacitor in series with a resistor (representing the electrode capacitance and solution resistance, respectively), to more detailed representations such as a transmission line model, which assumes that the properties of the circuit are distributed continuously throughout the material and thus models the EDLC as a series of individual circuit elements.[177] These more complex models, such as the two-slice transmission line model used by Péan and coworkers,[171] are especially useful when extrapolating macroscopic charging dynamics from microscopic simulations. Since we only want estimates of the relative charging dynamics among different ZTC materials, we use here the simplest RC equivalent circuit (effectively a one-slice model) to model the ZTC EDLCs.

Under an applied constant potential, the accumulated charge in an RC circuit exponentially approaches its steady-state value.[178] We therefore fit the transient charge per atom $q(t)$ of the EDLCs to the exponential function

$$q(t) = q_{inf}(1 - e^{-t/\tau}) \,, \tag{5.4}$$

where q_{inf} is the steady-state (infinitely equilibrated) charge per atom of the capacitor and τ is the time constant of the exponential, which for an RC circuit is $R \times C$ (the product of the resistance and the capacitance of the circuit). The circuit is considered to be equilibrated after 5τ, at which point the charge is within 1% of the steady-state charge.

Examples of the exponential fits for the charging of FAU_1, BEA, and EMT are shown in Figure 5.4. For all of the structures, the electrode atom charges are underestimated by the exponential fit during the first 1 ns to 2 ns of constant-potential charging (Supplementary Figure C.8). Defining an "average residual" $\varepsilon_{1\tau}$ to be the relative root-mean-square error (RMSE) between the exponential fit and the charging profile over the first characteristic time, we plot the characteristic time τ against pore limiting diameter (PLD) of the material, with the points colored to show $\varepsilon_{1\tau}$, in Figure 5.5. We observe that τ is negatively correlated with PLD, indicating that it takes longer for charge to equilibrate in materials with smaller PLD, likely due to larger diffusive barriers. Similarly, $\varepsilon_{1\tau}$ also increases with smaller PLD. Since $\varepsilon_{1\tau}$ reflects the quality of the exponential fit of the accumulated charge (higher $\varepsilon_{1\tau}$ indicates worse fit), the data show that the exponential fit at early times is more severely underestimated when PLD decreases. This underestimation of the initial charging profile

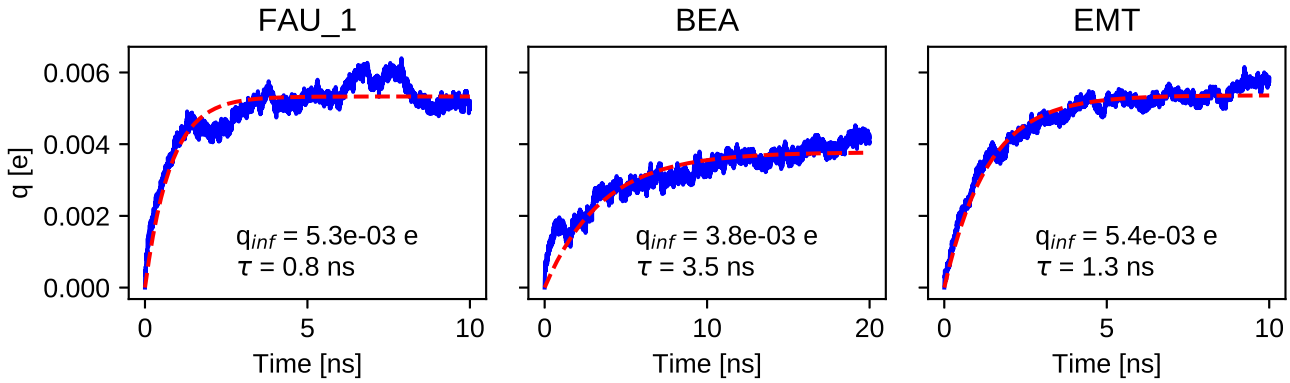

Figure 5.4: Evolution of average absolute charge per atom for FAU_1, BEA, and EMT, with a constant potential drop of 1 V applied to the cell starting at t=0 ps. Exponential fit is shown in the red dashed line and fit parameters are provided in the label.

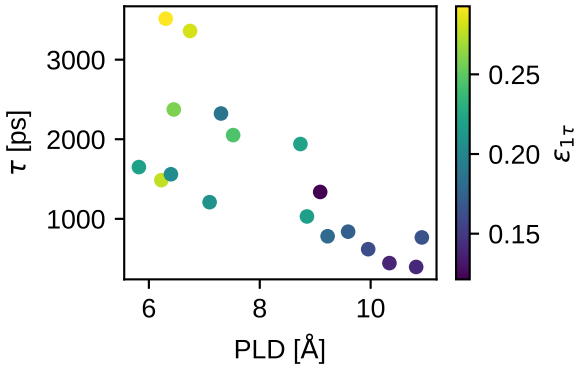

Figure 5.5: Characteristic timescale τ of EDLCs during charging at $\Delta\Psi = 1\,\mathrm{V}$, colored with the normalized $\varepsilon_{1\tau}$ of the exponential fit during the first characteristic timescale.

by the exponential fit suggests the existence of multiple timescales in EDLC charging, due to both progressive charging of the electrodes from the bulk electrolyte inward (consistent with a transmission line model), as well as "overfilling" and ion trapping analogous to that observed by Kondrat *et al.*[149,179] Both phenomena are discussed further in the Supporting Information.

5.3.2 Capacitance Screening

The capacitance under a constant applied potential is plotted against various geometric descriptors (top row) and average local interfacial properties (bottom row) in Figure 5.6. Geometric descriptors, in particular average pore size and pore size distributions, are of-

ten used to rationalize structure-capacitance relationships in EDLCs.[180,181] Some theoretical studies on slit nanopores even suggest that the capacitance could follow an oscillatory behaviour with the average pore size for carbons with well defined pore sizes.[182–184] However, in our materials we do not see a definite correlation with any of the geometric descriptors alone.

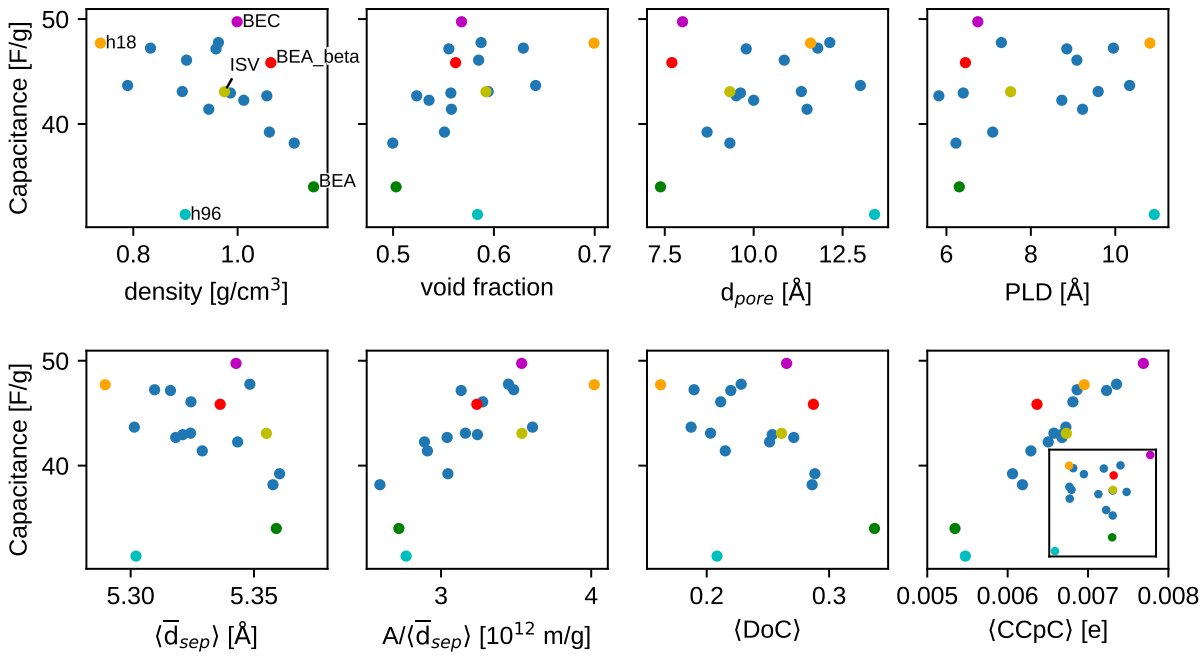

Figure 5.6: Gravimetric capacitance as a function of geometric descriptors in the top row: density, void fraction, average pore size, and PLD; and local properties in the bottom row: distance between counterions and electrode ($\langle \bar{d}_{sep} \rangle$), the surface area to charge separation ratio ($A/\langle \bar{d}_{sep} \rangle$), the average degree of confinement ($\langle DoC \rangle$), and the average charge compensation per carbon ($\langle CCpC \rangle$). The inset plots the gravimetric capacitance against total charge compensation in the coordination shell, where the x-axis range goes from 0.15 e to 0.23 e.

This suggests that while particular geometric descriptors might be a useful indicator of capacitance within particular families of materials, a clear relationship between capacitance and, for example, pore size is not the rule, but rather the exception for materials which are otherwise geometrically similar. ZTCs, due to their well-defined templated structures, exhibit a diversity of topologies, pore geometries, and local curvatures, which are not well captured by traditional geometric descriptors, but are known to influence charge storage.[147] Thus the insights we can glean from local interfacial properties in ZTCs might be better translated to microporous carbon materials in general.

The bottom row of Figure 5.6 plots capacitance versus quantities related to the electrolyte-

electrode interfacial configuration, which are computed for an ion in relation to the electrode atoms within its coordination shell: The charge separation ($\overline{d}_{sep}$) is the average distance between the counterion and the carbons within its coordination shell. The degree of confinement (DoC) is defined as the fraction of the maximum solid angle around a counterion which is occupied by carbon atoms within the coordination shell cutoff (set to the first minimum in the ion-carbon radial distribution function).[147] And finally, the charge compensation per carbon (CCpC), a quantity introduced in this work, is defined as the magnitude of the average charge per electrode atom in the coordination shell. A high CCpC indicates strong and localized charges in the electrode, as opposed to a weak or diffuse charge response. For all quantities, the angle brackets $\langle\rangle$ denote averaging over all counterions in an electrode.

Of particular interest with regard to classical theories of capacitance, a positive correlation can be observed between the capacitance and $A/\langle\overline{d}_{sep}\rangle$, reminiscent of Equation 5.2. This suggests that we can view capacitance in the ZTCs as arising from an "ideal" contribution from a reference electrode with the same $A/\langle\overline{d}_{sep}\rangle$, and a "non-ideal" contribution responsible for the deviations from classical double layer theory, arising from the microporosity. One measure of how micropores influence charge storage is the DoC. Here, we note that we are plotting in Figure 5.6 the average degree of confinement, $\langle$DoC$\rangle$, which obscures differences in the range and distribution of confinement values within a material. We do not observe a strong correlation with capacitance when $\langle$DoC$\rangle$ is below 0.25, and when $\langle$DoC$\rangle$ is above 0.25 the capacitance seems to be slightly negatively correlated with confinement. This finding adds nuance to the conclusions from previous studies that more confinement is generally a positive influence on charge storage efficiency.[147,150] We discuss confinement effects further in a later section, where we examine charge storage mechanisms in individual pores.

Finally, the local descriptor which appears to have the best correlation with capacitance is $\langle$CCpC$\rangle$, for which we observe a positive and nearly linear relationship with even less scatter than for $A/\langle\overline{d}_{sep}\rangle$. Capacitance and $\langle$CCpC$\rangle$ both aggregate information about the charge stored by the electrode atoms, however their strong correlation is not trivial because only about 30–45% of the electrode atoms are within the coordination shell of a counter-ion at a given timestep. These coordination shell carbons have a slightly larger-than-proportional share of charge, carrying between 35 and 50% of the net charge in the electrode (Supplementary Figure C.11). Perhaps surprisingly, the capacitance does not correlate with the total charge compensation within the coordination shell (inset of Figure 5.6). The observation that per-carbon (rather than total) charge compensation correlates so strongly with the capacitance indicates that localized charge distributions within the electrode store charge more efficiently than disperse charge distributions, as they use less electrode "real estate" to counterbalance an ionic charge.

One complication with comparing materials using local properties is that they are computed with a definition of coordination shell that uses a cut-off radius, r_{cut} around the ion. r_{cut} radius was chosen following the literature[147] as the first minimum in the ion-carbon RDF. However, we found in our materials that the first minima were not all at the same location in all materials, and some of them did not have a clear "minimum" at all. Therefore, we opted

to use the same r_{cut} of 6.3 Å for all materials, as this was the location of most of the RDF first minima and also was consistent with the literature. Further work is needed to determine how to better define a coordination shell and compute local interfacial properties. However, since we were able to observe quite a strong correlation of capacitance with $\langle \mathrm{CCpC} \rangle$ with the existing coordination shell definition, we leave this complication for a future study.

Having investigated geometric descriptors and local interfacial properties of EDLCs, averaged over the entire electrode, we find that almost all of them other than $\langle \mathrm{CCpC} \rangle$ lack a clear correlation with capacitance or, in the case of $\mathrm{A}/\langle \overline{d}_{sep} \rangle$, are correlated but exhibit significant scatter. In the following sections we turn our attention to the relationship between pore geometry, local electrolyte properties, and charge storage within individual pores of selected materials. We then move toward a more general framework for rationalizing differences in capacitance among ZTC materials. Due to the structural diversity of ZTC frameworks, we believe insights drawn from ZTCs are also relevant general design rules for porous carbon EDLC electrodes.

5.3.3 Charge Storage Mechanism in Selected Materials

We begin our examination of individual materials by considering BEA and BEA_beta, which are templated on different polymorphs of the same zeolite (known as zeolite beta) as shown in Figure 5.7a.[185] Naturally occuring zeolite beta consists of a mixture of polymorphs A and B, both of which contain layers of the same tertiary building unit which are rotated $\pm 90°$ with respect to each other. In polymorph A (corresponding to BEA_beta ZTC), the layers are stacked in a chiral fashion, while in polymorph B (corresponding to BEA ZTC), the rotation of the layers alternates. As a result the pore size distributions of BEA and BEA_beta differ, with slightly larger pore sizes for BEA_beta as shown in Figure 5.7b.

The capacitances of these ZTCs differ widely, with 34.0 F g^{-1} (45.8 F g^{-1}) gravimetric and 2.33 µF cm^{-2} (2.65 F cm^{-2}) areal capacitances computed for BEA (BEA_beta). The ions within the pores also have different degrees of confinement, possibly arising from the slight differences in the most probable pore sizes. As seen in Figure 5.7c, the anions in the anode of BEA_beta have a single peak in their DoC histogram around 0.33, while the anions in the BEA have on average higher DoCs, with one peak at 0.35 and another at 0.42. We might suppose from this that BEA should have the higher charge storage efficiency, since Merlet *et al.* showed that highly confined ions are able to store more charge in supercapacitors,[147] however, in this case the opposite is true: $\langle \mathrm{CCpC} \rangle_{\mathrm{DoC}}$ is higher in BEA_beta than in BEA for all DoC values (Figure 5.7d). In the cathode, as well, the average charge compensation is lower for BEA than for BEA_beta (Supplementary Figure C.12).

One noteworthy feature in the charge compensation distribution of the BEA anode is a minima in $\langle \mathrm{CCpC} \rangle_{\mathrm{DoC}}$ at 0.43 DoC (Figure 5.7d), the location of the higher peak in the DoC histogram. This drop is significant as it does not appear in BEA_beta, showing that sites with the same DoC can have drastically different contributions to capacitance. The source of this low-CCpC region becomes clear when examining representative configurations of the most highly confined anions of BEA and BEA_beta in Figure 5.8. In BEA, the anion is

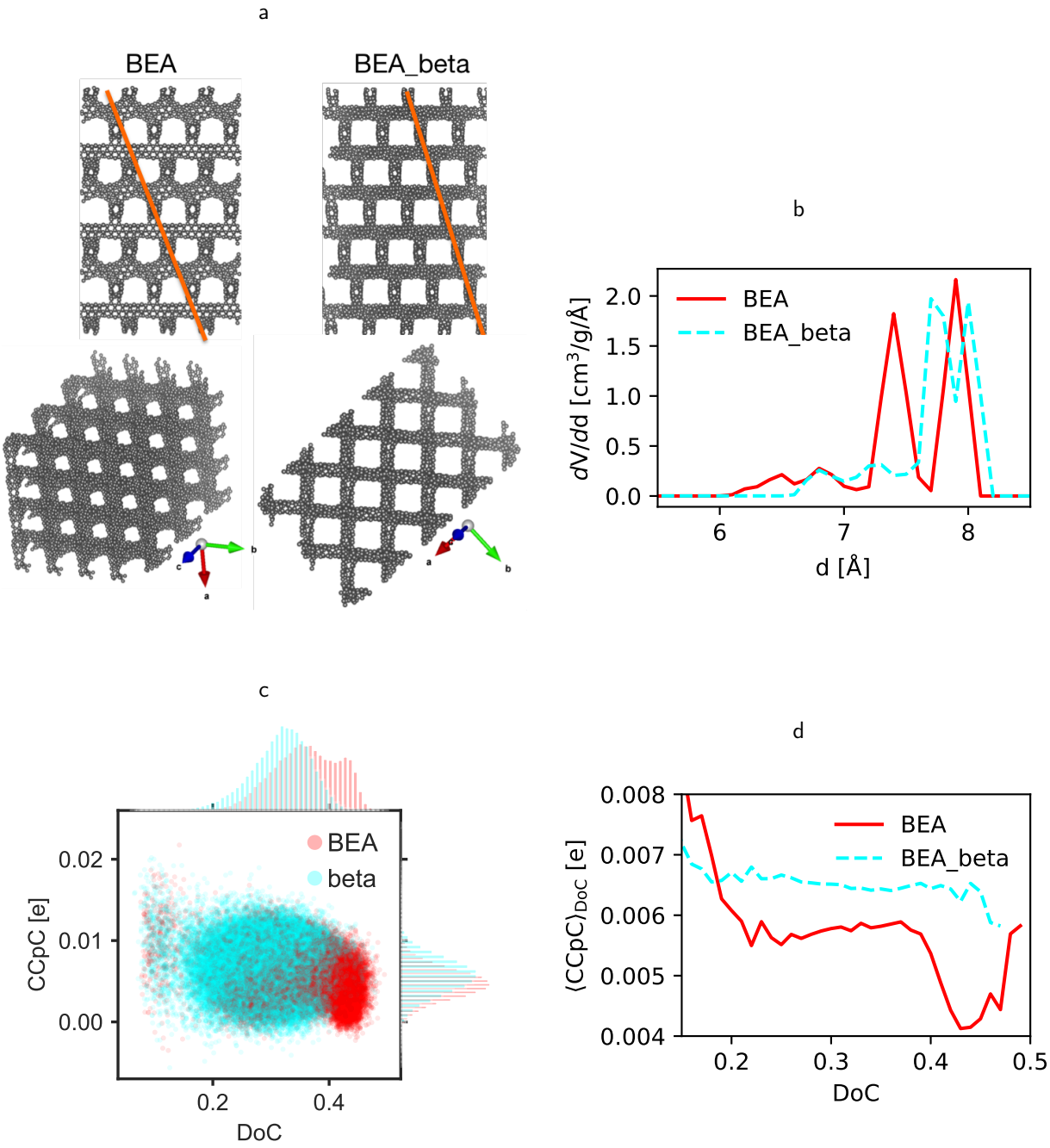

Figure 5.7: a, BEA and BEA_beta ZTC unit cells. b, pore size distributions. c, scatterplot showing joint distribution of CCpC and DoC for counterion adsorption sites, with probability distributions on the corresponding axes. d, conditional expectation of CCpC for a given DoC, denoted $\langle \mathrm{CCpC} \rangle_{\mathrm{DoC}}$.

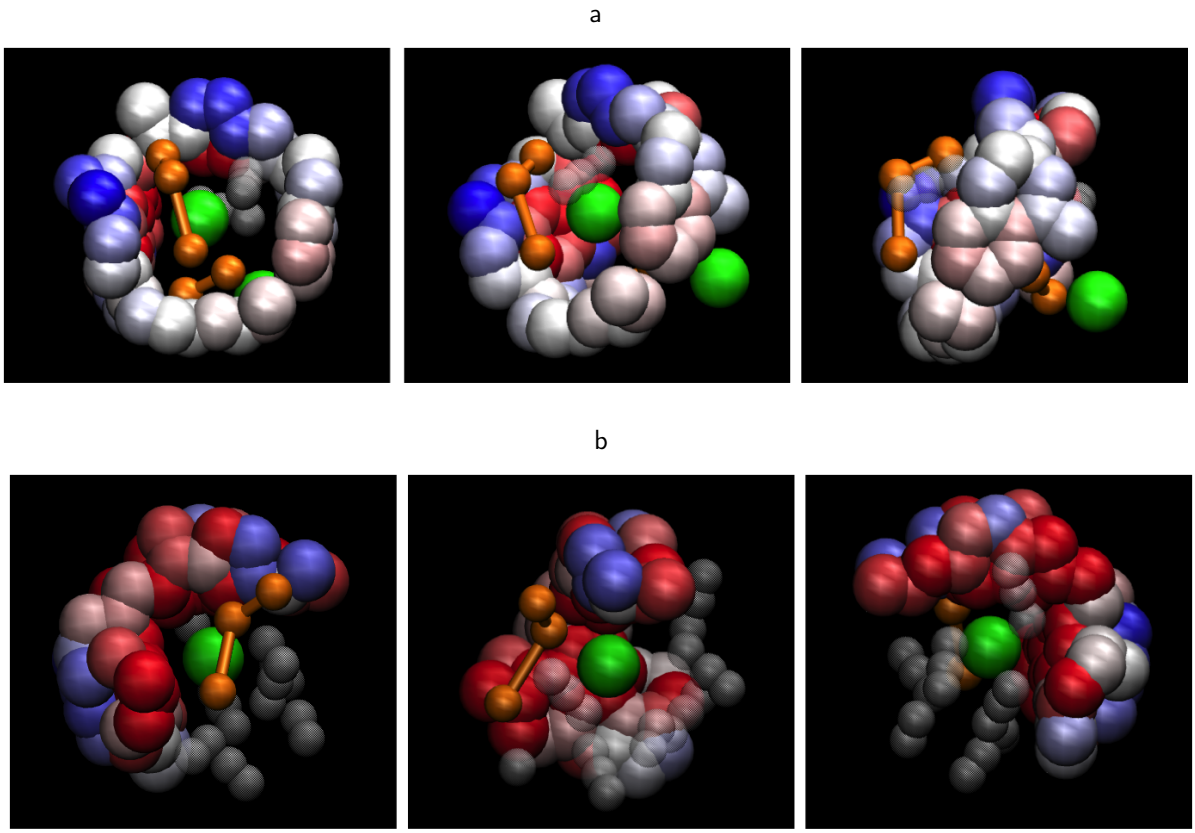

Figure 5.8: Snapshots of the coordination shells of highly coordinated anions in the positive electrodes of (a) BEA and (b) BEA_beta. Carbon atoms are colored according to their charge, with blue indicating negative and red indicating positive charge, scaled from $-0.01\,e$ to $0.01\,e$. The green color corresponds to the anions, BF_4^-, and the orange color to the cations, BMI^+; the transparent linear molecules are the solvent.

located in a cylindrical, nanotube-like structure, with a coordination shell of electrode atoms encircling the anion on all sides, while the anion in BEA_beta is only confined on two out of four sides by the electrode. The cylindrical pore of BEA is too small to fit another anion or even solvent molecule, but too large to snugly fit BF_4^-, causing it to be stuck in the middle of the pore where it is not close enough to induce a strong compensating charge on any of the atoms within its coordination shell. As a result, the coordination shell atoms in BEA have a total charge of $-0.026\,e$, while the coordination shell in BEA_beta has a total charge of $0.223\,e$. This effect has also been observed in the literature; for example, Kondrat *et al.* showed a local minimum in capacitance when the pore-to-ion-diameter ratio L/d was around 1.5, and increased capacitance when L/d was near 1 and 2.[146]

The charge storage efficiency also depends on the ion size in relation to the pore size: In the electrolyte studied here the cation is larger than the anion and its charge is distributed on three sites. As such, when a cation is at the center of the nanotube-like pore, the partial

charges of its coarse-grained sites are able to approach more closely to the electrode surface, making the equivalent pore in the cathode more efficient at storing charge. This explains why there is no drop in $\langle \mathrm{CCpC} \rangle_{\mathrm{DoC}}$ in the BEA cathode (Supplementary Figure C.12). These observations highlight one important role of pore geometry in determining charge storage efficiency, by influencing local ion density and electrolyte coordination environment.

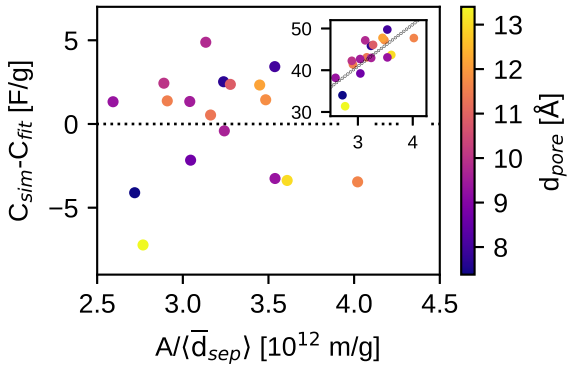

Figure 5.9: Deviation of gravimetric capacitance from the linear least-squares fit of capacitance vs. $\mathrm{A}/\langle \overline{d}_{sep} \rangle$. Structures mentioned in the text are labeled. The inset shows the simulated gravimetric capacitance with the fitted line and the color bar indicates the pore diameter.

We next examine another pair of ZTCs, BEC and ISV, to test our hypothesis that differences in microporosity leads to deviations from the classical capacitance relation, Equation 5.2. We chose these two structures because they have virtually the same $\mathrm{A}/\langle \overline{d}_{sep} \rangle$ ($3.5 \cdot 10^{12}\,\mathrm{m\,g^{-1}}$), but different capacitances of $50\,\mathrm{F\,g^{-1}}$ and $43\,\mathrm{F\,g^{-1}}$ for BEC and ISV, respectively, putting them at high and low ends of the capacitance range for the given $\mathrm{A}/\langle \overline{d}_{sep} \rangle$ value, as seen in the plot of $C_{sim} - C_{fit}$ in (Figure 5.9). Analyzing these structures in a similar fashion as for the BEA polymorphs, we find that BEC has more highly confined sites than ISV and a higher $\langle \mathrm{CCpC} \rangle_{\mathrm{DoC}}$ for all values of DoC (Supplementary Figure C.13).

We visualize in Figure 5.10 the instantaneous CCpC and $\overline{d}_{sep}$ of each counterion at snapshots taken every 0.5 ps during the production run, along with probability distributions for CCpC and $\overline{d}_{sep}$ along the corresponding axes. The joint distributions for the two materials are largely overlapping, but the adsorption sites in BEC have their highest probability density at slightly lower $\overline{d}_{sep}$ than the sites in ISV, corresponding to more efficient charge storage (as seen by the higher CCpC distribution) and higher overall capacitance of BEC.

By examining individual pairs of structures, and comparing properties of the individual pores inside those structures, we start to obtain insights into how charge storage mechanisms are related to pore geometries. We generalize this approach in the following section, looking at many structures to extract structure-property trends.

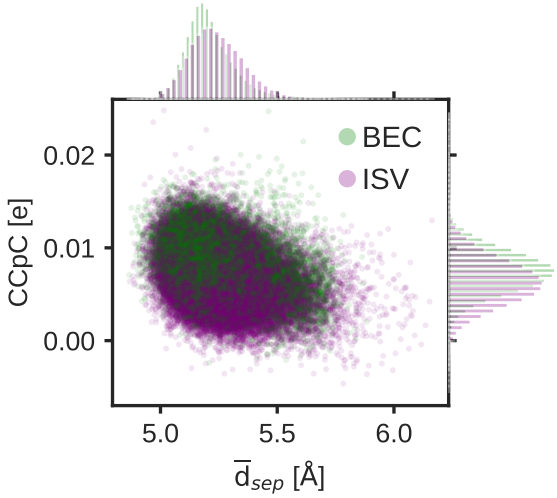

Figure 5.10: Scatterplot of CCpC and $\overline{d}_{sep}$ of each counterion adsorption site during production run, with probability distributions, for BEC and ISV.

5.3.4 Effect of Pore Geometry on Charge Storage Efficiency

We show in Figure 5.11 the structures of the materials with highest and lowest $C_{sim} - C_{fit}$, indicating the average charge of each crystallographically unique electrode carbon atom during the equilibrated constant potential run, along with the probability density isosurfaces of counterion locations within the electrodes. Isosurfaces for adsorption sites with more than $0.1\,e$ total charge compensation are shown in purple, while sites with less than $0.1\,e$ charge compensation are shown in green. This allows us to visually associate geometry with average contribution to capacitance for an individual pore.

We observe that the adsorption site isosurfaces which have more than $0.1\,e$ coordination-shell charge compensation are close to the surface of the frameworks, while the isosurfaces associated with less than $0.1\,e$ charge compensation tend to be in the middle of the pores. Inspecting the average atomic charges, we observe that BEC and h91 (Figure 5.11a and b) have more individual carbon atoms with high charge, corresponding to high CCpC. As seen in Figure 5.9, BEC and h91 are also the two materials with the highest enhancement in capacitance compared to materials of similar $\mathrm{A}/\langle\overline{d}_{sep}\rangle$. In contrast, h18, h49, and ISV, which have $\mathrm{A}/\langle\overline{d}_{sep}\rangle$ similar or greater than that of BEC, but lower capacitance, have fewer highly-charged atoms. Figure 5.11f provides further quantitative evidence of the correlation between the probability of highly-charged atoms and $C_{sim} - C_{fit}$: structures with a higher probability density of average atomic charge greater than $0.1\,e$ tend to have a higher $C_{sim} - C_{fit}$.

In order to rationalize the differences in charge storage between these materials, we focus on the local radius of curvature of the materials, as this roughly determines the distribution of ion-electrode distances at a particular adsorption site. In BEC, which has square-shaped

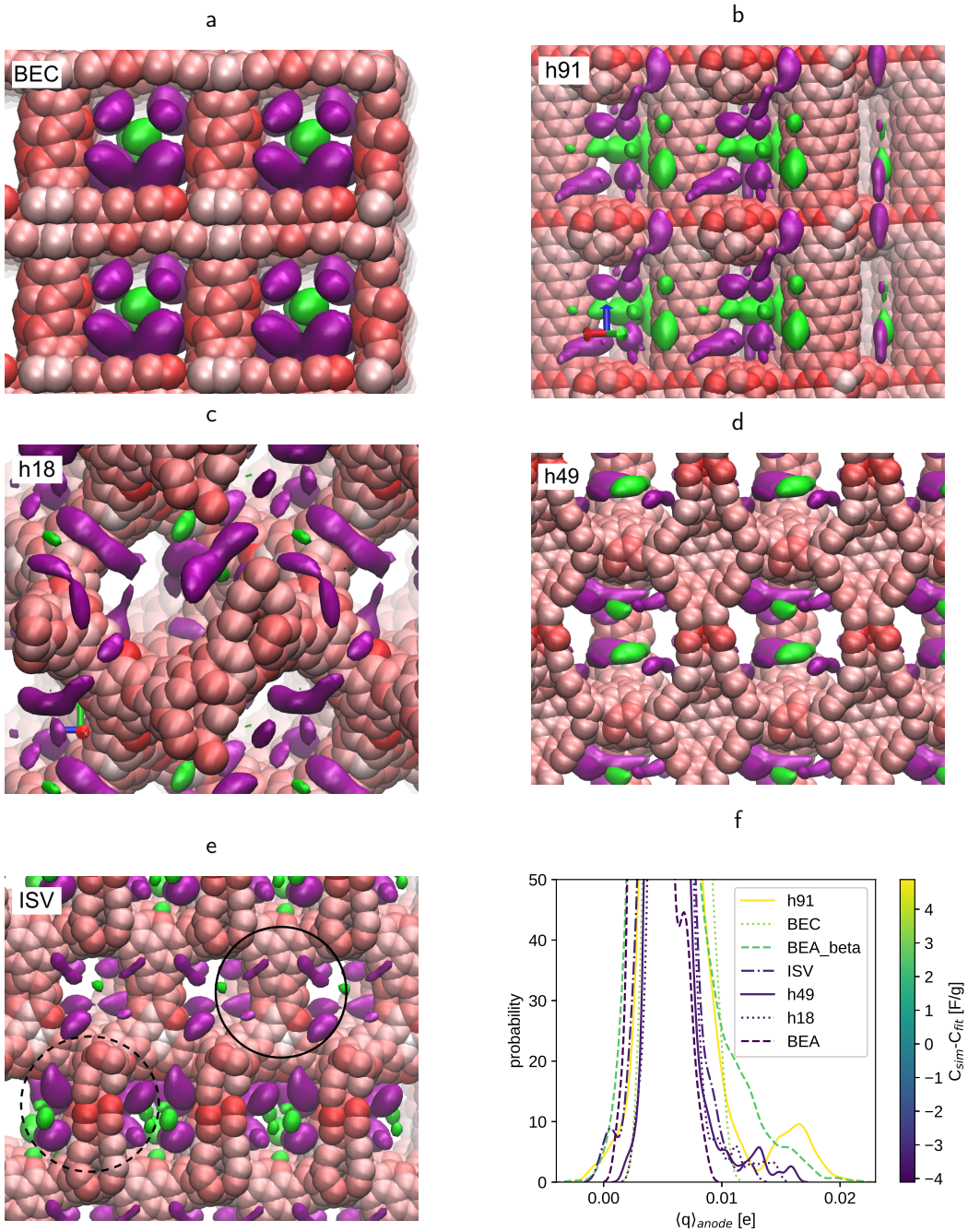

Figure 5.11: Average electrode atom charges and isosurfaces of ion probability density, computed for anions within the anode (a-e), probability density of average charges in the anode of materials discussed in the text, colored by deviation of gravimetric capacitance from the linear fit (f). Electrode atoms are colored on a scale from 0 (white) to 0.01 e (red). Purple isosurfaces indicate total charge compensation within the coordination shell cutoff radius greater than 0.1 e, while green isosurfaces indicate total charge compensation less than 0.1 e.

windows with right-angle "corners," we see electrode atoms with large average partial charges at two locations for each adsorption isosurface, corresponding the positions at which an adsorbed ion can be in close proximity with two "walls" of the framework simultaneously. In h91, cynlindrical pores adjoining with rounded beams create small-radius of curvature sites where ions can again approach the electrode surface closely at multiple sites, leading to more electrode atoms with large partial charges.

In contrast, adsorption sites which are near large radius of curvature sites, such as in h18, h49, and ISV, (Figure 5.11c, d, and e), tend to be associated with materials with lower capacitances relative to their respective $A/\langle\overline{d}_{sep}\rangle$. In adsorption sites with a large radius of curvature, an ion is not able to induce as many favorable Coulombic interactions with the electrode surface, leading to lower charge compensation for ions within those materials. ISV merits particular mention, as it does contain some adsorption sites with low radius of curvature and high charge compensation (dashed circles in Figure 5.11e), but because it also has high radius of curvature/low charge compensation sites (solid circles), ISV still has a relatively low capacitance considering its high $A/\langle\overline{d}_{sep}\rangle$ (Figure 5.9).

Overall, our results demonstrate that pore geometries which are capacitance-enhancing tend to faciliate the close approach of counterions to multiple carbons within the electrode via low radius of curvature adsorption sites, so that the compensating charge from the electrodes can be localized and large in magnitude to most efficiently screen countercharges and allow for higher counterion loading (and thus a large magnitude of charge storage) in the pores. Conversely, capacitance-diminishing properties include pores with high radius of curvature and cylindrical and ill-fitting pores, as these types of sites have inefficient charge storage and therefore decrease the overall capacitance of the material.

5.4 Conclusions

In summary, we developed a semi-automated workflow to build an EDLC simulation cell from the crystal structure of the ZTC materials, loaded with the amount of solvent that yields the experimental density in the bulk liquid region when the cell is relaxed with zero charge. We investigated different methods to equilibrate the EDLC and converge its capacitance. First, we used a constant-charge equilibration and a 1-D Poisson potential to compute voltage drop across the cell, and next tested a method to compute the local potential on each electrode atom from a constant-charge simulation, but we found that neither method provided an accurate calculation of the applied potential that would be needed to maintain an equivalent amount of charge on the electrode. We believe this is because the homogeneous charge distribution applied during constant-charge simulations is not representative of the charge distribution that would arise in a constant-potential simulation. Instead of equilibrating using a constant-charge scheme, we directly applied a constant potential to the cell. We found that the equilibration time at constant potential varied depending on the material, from as little as 3 ns to over 10 ns. The equilibration time increased, in general, as the pore size decreased, indicating that the limiting process in EDLC charge convergence is

solvent diffusion and reorganization, which becomes slower as the PLD decreases. We also found evidence of ion trapping and progressive charging of the electrode, which leads to an underestimation of the initial charging profile by a single-exponential fit.

We observed that the capacitance of the ZTCs was not correlated with geometric pore descriptors such as PLD, and only weakly correlated with most "globally" averaged local properties such as DoC. However, we found that it was correlated strongly with $\langle$CCpC$\rangle$, a measure of the magnitude and localization of electrode charge in the coordination shell. We were able to rationalize some of the mechanisms of charge storage by comparing similar ZTC structures with key differences leading to diverging capacitances. By comparing probability distributions for charge compensation, degree of confinement, and charge separation distances, we identified pore geometries that corresponded to enhanced or diminished charge storage efficiency. Finally, by analyzing the average charge storage across materials at the high and low extremes of capacitance, we observed that the capacitance tends to be higher in materials which have pores with low radius of curvature adsorption sites, compared to pores with rounded corners or larger radii of curvature. Low radius of curvature sites in pores accommodate ions which can approach close to the pore at multiple points, inducing strong opposing charges in the electrode which efficiently screen the ion charge. These insights can inform design of materials, or identification of materials in computational screening, for next-generation porous carbon EDLCs.

Chapter 6

Summary and Outlook

In this work I presented my doctoral research on molecular simulations of porous materials for applications in energy storage and environmental applications. The first two chapters were motivated by experimental applications (propene dimerization and THC sensing for breathalyzers), and focused largely on molecular simulation methods for bulky adsorbates. In Chapter 2, I showed that we can use configurational-bias Monte Carlo methods to compute the adsorption energy of chain molecules, and that this adsorption energy, though a simple metric, can be used to predict with considerable accuracy how a material can enhance the conversion of linear alkenes over branched ones. Initially, I was surprised at how well the predicted linear enhancement matched experimental results,[46] since heterogeneous catalysis is a complex process, but I concluded that this shows the extent to which the pore shape influences the catalysis product distribution. (This phenomenon is not restricted to catalysis; the importance of shape in determining binding site specificity has also been noted in such chemically complex processes as protein-ligand docking.[186,187]) Our screening results sought to provide some insight into shape selectivity, a well-studied concept,[188,189] in the context of the industrially important olefin dimerization reaction. We found that the effect of pore size diminishes with very large pores, whereas for smaller pores the effect on linear conversion (whether enhancing or diminishing) depends on the enthalpy-entropy tradeoffs of the product confinement in very small pores. Diffusion limitations in smaller pores might be a problem for an industrial reaction process, but even among the MOFs with larger pore sizes, there are materials that can increase the linear conversion of propene dimerization by several percentage points over the current industrial standard. This could be significant C_6 olefins are produced at industrial scales, and an improved reaction selectivity could help both the chemical industry and the environment because it would take less energy to produce the same amount of product.

In Chapter 3, we screened a database of MOFs for a THC adsorbent material, which could be used in a THC breathalyzer. Such a breathalyzer could help to quantify cannabis intoxication and impairment, and thus empower legislation on a responsible use of cannabis, which is seeing increasing legalization both in the United States and abroad. We believed that MOFs could help address some of the challenges of THC sensing, in particular the low

concentration of THC in the breath and the need for a selective sensing mechanism. We encountered several interesting simulation challenges during the course of our work, due to the complex shape of the THC molecule, comprising a bulky aromatic head with a long alkyl tail. We tested two models of THC, one with only the bulky head group and another full model with the head and tail, to see whether the salient features of THC adsorption could be captured by using the more computationally efficient head model. We also compared the results of Monte Carlo simulations under the NVT ensemble with one molecule versus Widom insertions in an empty framework, as possible ways to compute the average adsorption energy of THC. We found that the head model was a decent proxy for computing the adsorption energy of THC in most materials, but had lower accuracy for materials with a very low or very high Henry coefficient. We identified several promising frameworks based on a trio of adsorption motifs, most notably the "parking spots" motif, which is an ideal trait for THC adsorption, as it combines large channels through which the bulky molecule can easily diffuse, with slit pores extending from the main channel where THC can bind favorably.

There are both methodological and experimental takeaways from our THC study. From a simulation methodology point of view, we showed that using a partial model of a bulky adsorbate can be sufficient, as we found a similar ranking of materials using the head model as compared to the full THC model. We also found that for bulky adsorbates, NVT simulations are more reliable methods to compute a heat of adsorption, because Widom insertion methods are not accurate unless run for an extremely long time. The next steps of this project are to determine through experiments whether the promising materials that we identified can be synthesized, whether their THC adsorption performance is as predicted by our simulations, and in the longer term, whether THC adsorption in MOFs is a practical component of a selective and accurate THC sensing device.

The second half of my dissertation focuses on energy and environmental applications, investigating mechanisms by which microporous materials can be promising candidates for improved carbon capture and EDLC technologies. Chapter 4 is an in-depth study of the amine-appended Mg_2(dobpdc) MOF, which has a unique step-shaped CO_2 adsorption isotherm, as demonstrated by previous experimental work. We did not study carbon capture directly in this chapter, but instead focused on a feature of the material that was experimentally not well understood: the nature of the amine functional group dynamics. We simulated the system with a set of ReaxFF parameters that we optimized for the amine-appended MOF, so that we could study dynamics arising from bonds breaking and forming in the system. We found that we were able to observe a "hopping" motion in which the two amine ends of the diamine functional group alternated in their coordination bonding to a single metal site. This motion was consistent with experimental evidence that the two amine groups were equivalent on the timescale of NMR, even though only one amine end could coordinate to the metal node at a single time.[27] We studied the transition state of this hopping transition (an intermediate state in which both amine ends were coordinated to the metal) and calculated the activation energy and enthalpy of this transition for the original *N,N'*-dimethylethylenediamine molecule as well as for experimentally synthesized analogs. We found that by changing the end groups of the diamines, thereby increasing or decreasing the steric hindrance, it was

possible to change the rate and activation energy of hopping. This insight is relevant to the carbon capture applications of the amine-appended MOFs because the strength of the amine-metal coordination bond and the mobility of the functional group can influence the step temperature or pressure at which CO_2 undergoes phase-change adsorption in the material, and hence allows for the design of a material with an optimum adsorption step for carbon capture solutions.

Chapter 5 presents the most recent research I have done during my PhD on studying zeolite-templated carbons as candidates for improved electrical double-layer capacitor electrodes. This work was inspired by the work of a former PhD student colleague in the group, Dr. Efrem Braun, who designed a way to synthesize ZTC materials *in silico* from a given zeolite.[158] I found the prospect of using ZTCs for EDLC applications interesting because most porous carbons used for EDLCs are amorphous, meaning that correlating structure to properties is very difficult as the pore geometry is not well-defined. From an environmental perspective, EDLCs are an important technology to complement batteries and renewable energy technologies for a global energy portfolio that is not dependent on greenhouse gas-emitting fossil fuels. We developed a high-throughput procedure to build EDLC cells from ZTC structures and solvate them with an organic electrolyte. From our initial studies we learned that when simulating EDLCs, it is very important to ensure that the capacitance is converged, as the processes of solvent diffusion and reorganization result in slow equilibration times (between 3 ns and 10 ns, depending on the structure). From our constant potential simulations to study electrode charging, we found a strong correlation between charging rate and pore size, with faster charging speeds in materials with larger pore limiting diameters.

When investigating the equilibrium capacitance of the ZTC materials, we did not find a clear correlation between capacitance and any of the simple geometric pore descriptors conventionally used. However, we discovered that the capacitance was correlated to quantities related to the local configurations of the electrode and electrolyte, which we termed "interfacial" properties. For example, we introduced a descriptor called charge compensation per carbon, which measures the efficiency of charge storage, and used it to show that regions of the electrode surface with small radii of curvature stored charge most efficiently. Ions within these tight pores were able to sit closer to the electrode surface than ions within pores with a more a gentle curvature, thus allowing for stronger local induced charges in the electrode, which screen ions using less electrode "real estate." It is our hope that this work will inform better EDLC design, both computational and experimental, and motivate experimental efforts to synthesize the ZTCs that we predicted to have high capacitance.

Appendix A

Supporting Information for Propene Dimerization

A.1 Adsorbate Probability Density Plots

Below are probability density plots of C_6 olefin isomer adsorption sites inside selected frameworks. The probability densities correspond to the indicated points marking the geometric center of the π bond on the three product isomers shown below:

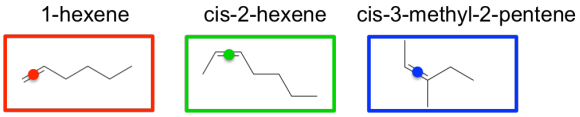

The atoms shown in the figures are colored as follows: Mg (green), O (red), C (gray), H (white), Si (tan).

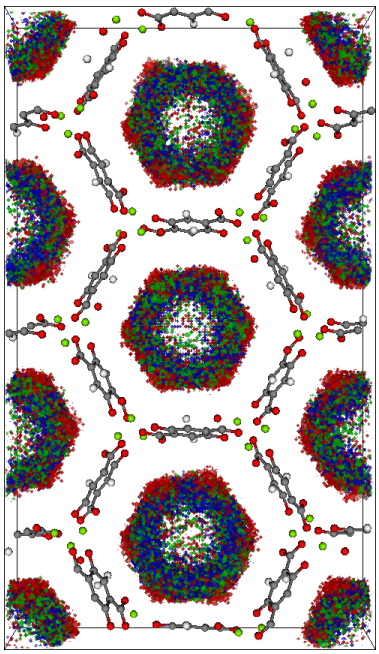

Figure A.1: Mg_2(dobdc) MOF, $d_{free} = 11.03\,\text{Å}$.

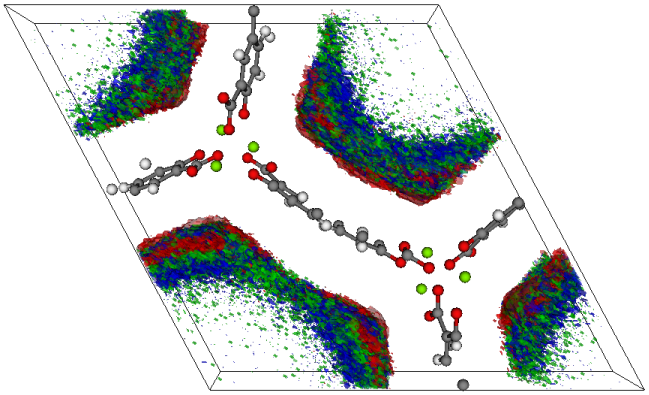

Figure A.2: Mg_2(dobpdc) MOF, $d_{free} = 16.00\,\text{Å}$.

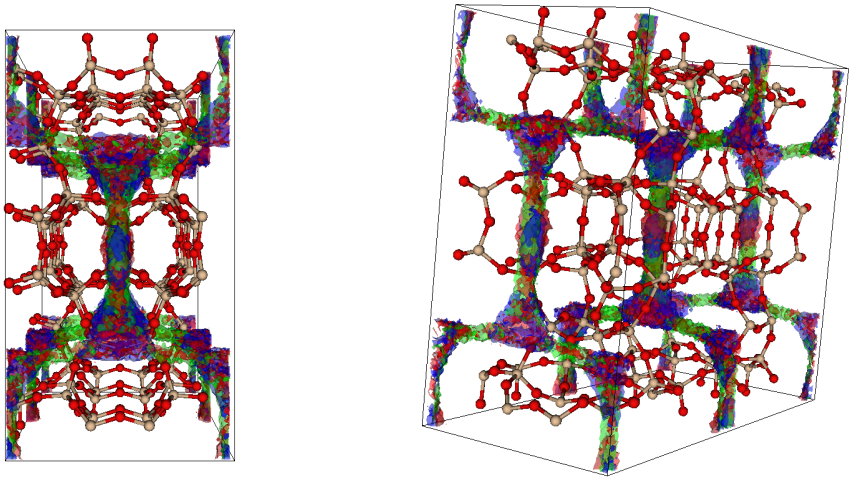

Figure A.3: ITR zeolite, $d_{free} = 4.72\,\text{Å}$.

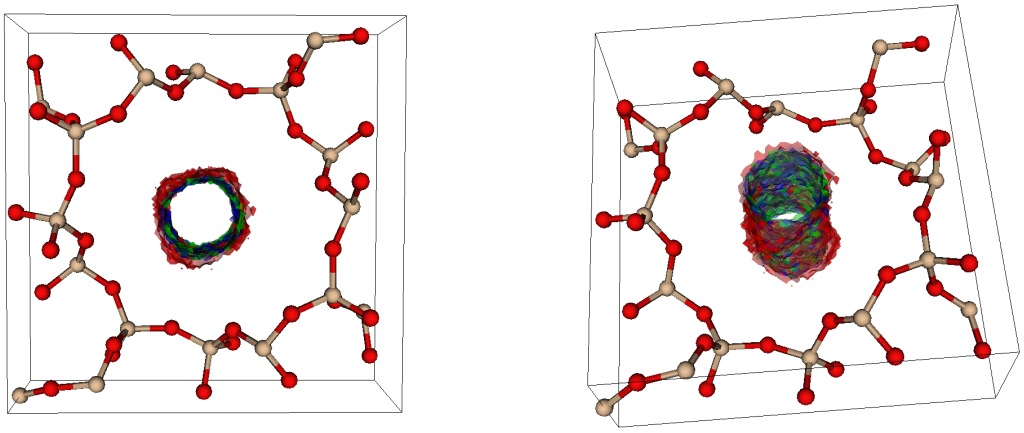

Figure A.4: VET zeolite, $d_{free} = 5.58\,\text{Å}$.

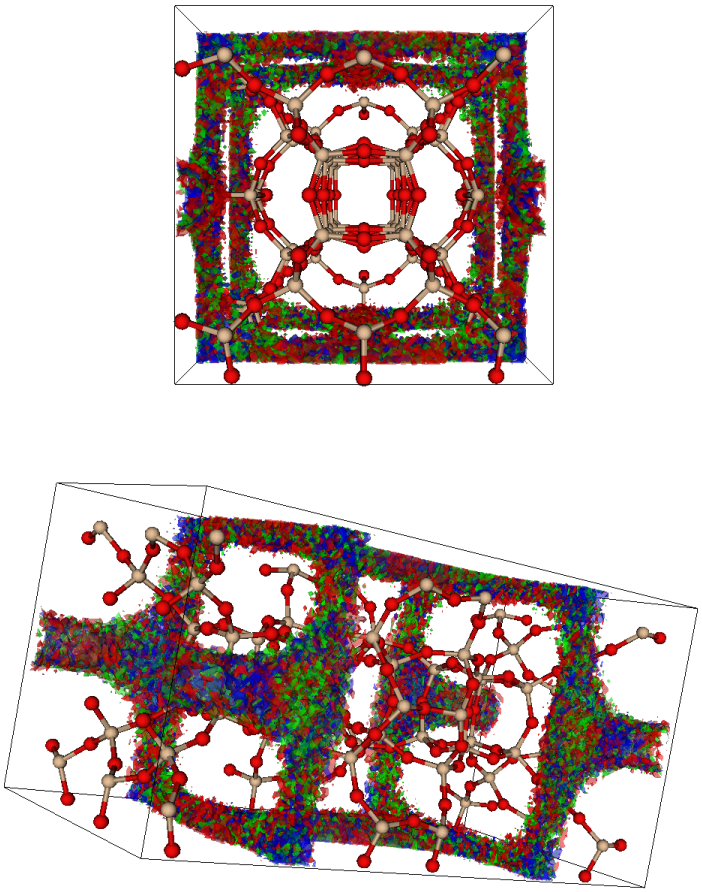

Figure A.5: ISV zeolite, $d_{free} = 5.92\,\text{Å}$.

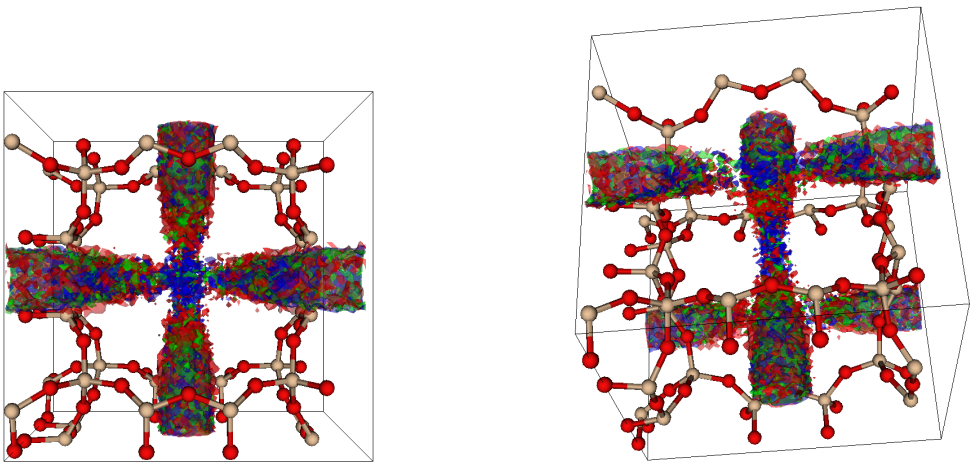

Figure A.6: BEC zeolite, $d_{free} = 6.12\,\text{Å}$.

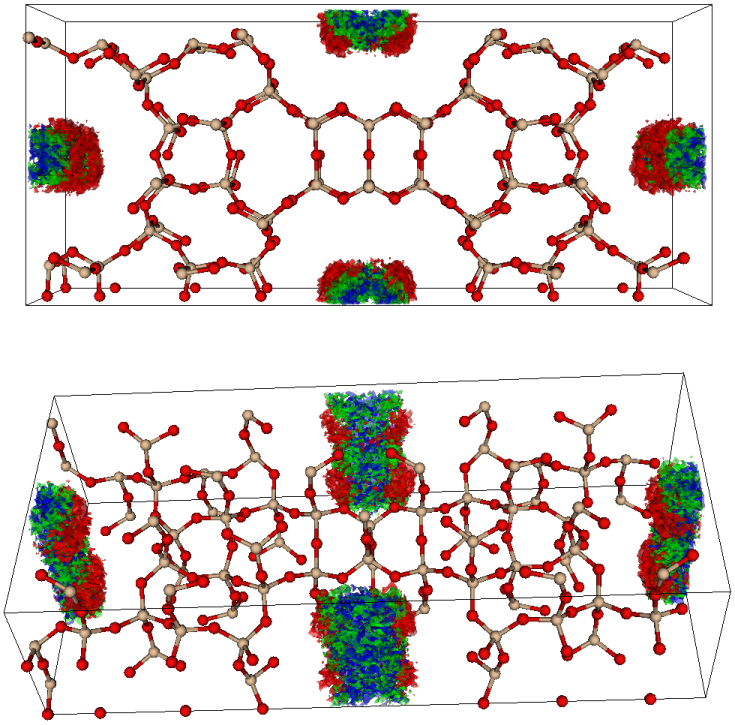

Figure A.7: AET zeolite, $d_{free} = 7.19\,\text{Å}$.

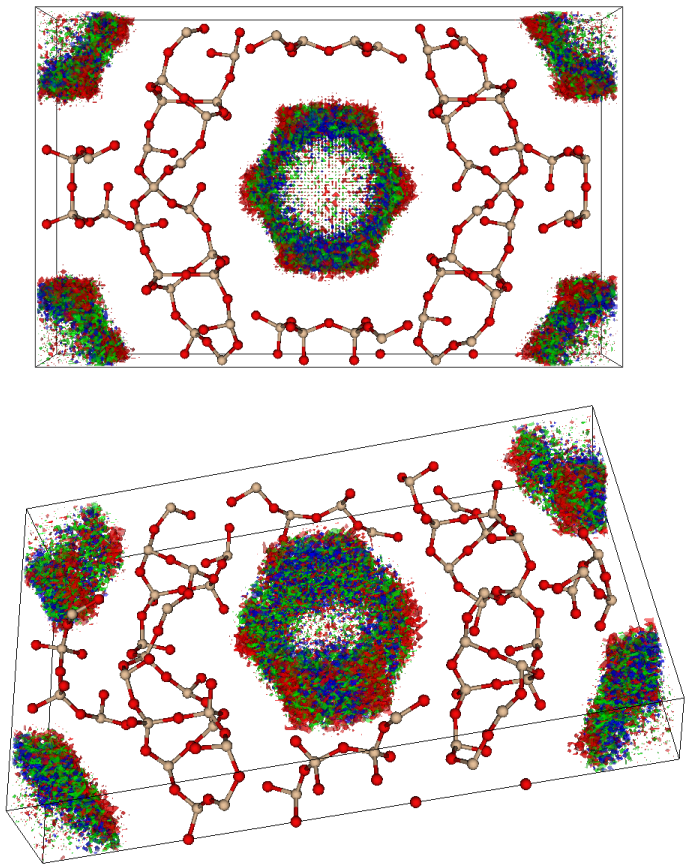

Figure A.8: h8160847 zeolite, $d_{free} = 11.88\,\text{Å}$.

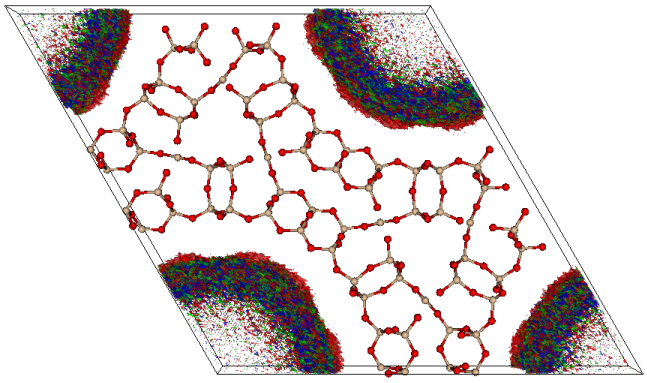

Figure A.9: h8322962 zeolite, $d_{free} = 20.37\,\text{Å}$.

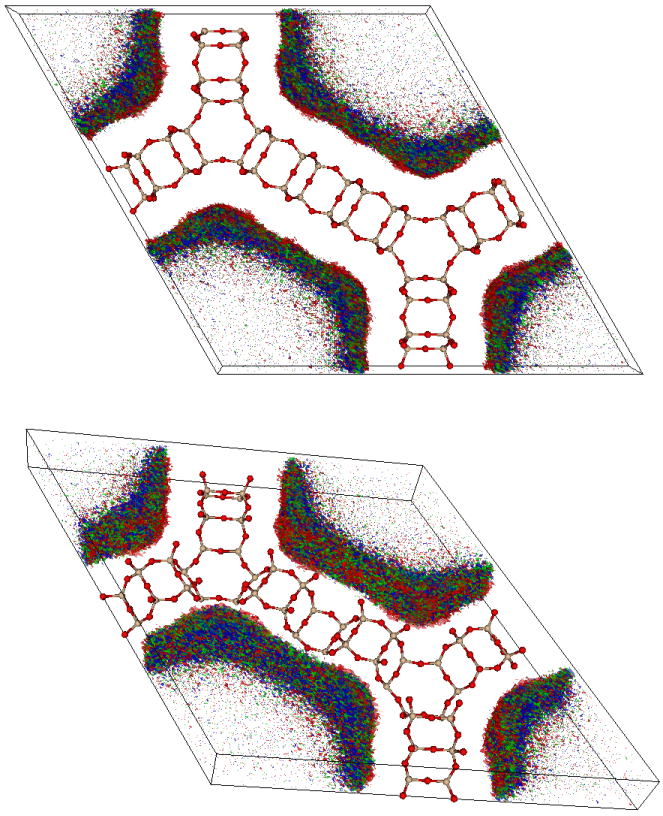

Figure A.10: h8325731 zeolite, $d_{free} = 28.44\,\text{Å}$.

A.2 Framework Descriptor and Product Distribution Data

Table A.1: Geometric descriptors and thermodynamic properties of the materials studied.

Framework	Free sphere diam (Å)	Linear conversion	$\Delta\Delta H_{ads}$ (kJ mol^{-1})[a]	$\Delta\Delta S_{ads}$ (J/molK)[b]	Material class
Mg-MOF-274	16.00	0.498	-8.62	-7.96	MOF
Mg-MOF-74	11.03	0.489	-8.22	-5.61	MOF
Ni-MOF-74	11.02	0.482	-7.64	-5.04	MOF
1000_all_conf_0_0	6.26	0.370	-8.37	-6.54	MOF-74 Analog
101.1_all_conf_413_0	24.72	0.500	-6.69	-6.70	MOF-74 Analog
102.1_all_conf_239_0	30.51	0.495	-6.09	-5.75	MOF-74 Analog
107.1_all_conf_1073_0	35.17	0.485	-5.66	-5.80	MOF-74 Analog
118_all_conf_528_0	36.77	0.492	-5.98	-5.96	MOF-74 Analog
119_all_conf_89_0	23.32	0.496	-7.27	-7.37	MOF-74 Analog
120_all_conf_45_0	21.71	0.491	-7.19	-7.05	MOF-74 Analog
149_all_conf_47_0	20.94	0.491	-6.07	-5.54	MOF-74 Analog
15_all_conf_144_0	36.64	0.487	-5.56	-5.50	MOF-74 Analog
152x0_all_conf_7740_0	27.14	0.495	-6.21	-6.03	MOF-74 Analog
152x1_all_conf_7899_1	24.66	0.494	-6.33	-5.97	MOF-74 Analog
16_all_conf_9_0	18.35	0.504	-6.45	-5.13	MOF-74 Analog
161_all_conf_493_1	23.28	0.491	-5.89	-5.61	MOF-74 Analog
162_all_conf_233_1	21.31	0.493	-6.73	-7.03	MOF-74 Analog
169_all_conf_656_0	25.25	0.487	-6.19	-6.35	MOF-74 Analog
17_all_conf_29_0	22.35	0.494	-5.89	-5.11	MOF-74 Analog
182_all_conf_7056_1	27.14	0.496	-6.63	-6.56	MOF-74 Analog
184x0_all_conf_4506_0	28.36	0.500	-6.88	-7.38	MOF-74 Analog
184x1_all_conf_10850_1	21.02	0.512	-8.23	-8.93	MOF-74 Analog
185x0_all_conf_6662_0	26.93	0.493	-6.09	-5.74	MOF-74 Analog
185x1_all_conf_10123_1	28.07	0.489	-6.58	-7.15	MOF-74 Analog
187_all_conf_768_1	30.62	0.489	-5.63	-5.21	MOF-74 Analog
188_all_conf_3005_1	22.38	0.492	-6.11	-5.81	MOF-74 Analog
190_all_conf_3_1	20.33	0.497	-6.08	-5.22	MOF-74 Analog
192_all_conf_39_0	26.88	0.494	-6.06	-5.62	MOF-74 Analog
193_all_conf_49_0	37.72	0.489	-5.97	-6.22	MOF-74 Analog
195_all_conf_128_0	18.11	0.500	-6.39	-5.57	MOF-74 Analog
196_all_conf_14_0	25.07	0.498	-6.78	-6.40	MOF-74 Analog
20_all_conf_167_0	21.80	0.495	-6.17	-5.48	MOF-74 Analog
208_all_conf_5978_0	34.43	0.491	-5.93	-5.97	MOF-74 Analog
216_all_conf_471_0	25.66	0.497	-6.98	-7.17	MOF-74 Analog
217_all_conf_728_1	20.45	0.484	-5.62	-5.24	MOF-74 Analog
218_all_conf_2770_0	15.00	0.495	-6.89	-6.65	MOF-74 Analog
22_all_conf_75_0	30.55	0.491	-5.73	-5.07	MOF-74 Analog

Continued on next page

Framework	Free sphere diam (Å)	Linear conversion	$\Delta\Delta H_{ads}$ (kJ mol^{-1})	$\Delta\Delta S_{ads}$ (J mol^{-1} K^{-1})	Material class
226_all_conf_1_1	14.45	0.510	-6.81	-5.20	MOF-74 Analog
227_all_conf_0_0	15.85	0.510	-6.73	-5.07	MOF-74 Analog
229_all_conf_6704_0	28.48	0.491	-6.05	-5.88	MOF-74 Analog
232_all_conf_84_1	15.77	0.499	-6.51	-5.47	MOF-74 Analog
24_all_conf_9_0	32.70	0.496	-7.20	-8.11	MOF-74 Analog
258_all_conf_1584_0	28.72	0.488	-5.96	-5.99	MOF-74 Analog
261.1_all_conf_203_0	33.49	0.491	-5.86	-5.68	MOF-74 Analog
261.2_all_conf_272_0	35.60	0.490	-5.98	-6.15	MOF-74 Analog
264_all_conf_76_0	31.67	0.471	-8.53	-10.92	MOF-74 Analog
269_all_conf_385_0	35.12	0.504	-7.71	-9.08	MOF-74 Analog
271_all_conf_24_0	21.35	0.490	-6.02	-5.65	MOF-74 Analog
277_all_conf_224_0	44.57	0.492	-7.38	-9.21	MOF-74 Analog
284_all_conf_0_0	20.25	0.496	-6.10	-5.15	MOF-74 Analog
285_all_conf_0_0	25.09	0.494	-6.03	-5.55	MOF-74 Analog
32_all_conf_43_1	24.85	0.493	-6.41	-6.52	MOF-74 Analog
34_all_conf_144_0	30.96	0.491	-5.82	-5.52	MOF-74 Analog
34.1_all_conf_10_0	25.51	0.497	-6.40	-6.29	MOF-74 Analog
6_all_conf_98_0	27.76	0.497	-6.63	-6.69	MOF-74 Analog
7_all_conf_50_0	27.04	0.491	-6.11	-5.96	MOF-74 Analog
8_all_conf_4278_1	33.74	0.493	-6.76	-7.82	MOF-74 Analog
85_all_conf_32_0	18.27	0.499	-6.62	-5.90	MOF-74 Analog
88_all_conf_107_0	33.64	0.489	-5.63	-5.42	MOF-74 Analog
9_all_conf_97_0	33.05	0.497	-6.66	-6.95	MOF-74 Analog
91_all_conf_1023_0	27.07	0.490	-5.90	-5.59	MOF-74 Analog
95_all_conf_567_0	37.45	0.490	-5.74	-5.62	MOF-74 Analog
96_all_conf_27_0	21.44	0.495	-6.02	-5.17	MOF-74 Analog
97_all_conf_1034_0	32.34	0.489	-5.61	-5.32	MOF-74 Analog
98x0_all_conf_2659_0	22.35	0.502	-7.14	-7.16	MOF-74 Analog
98x1_all_conf_4342_1	24.33	0.488	-6.29	-6.37	MOF-74 Analog
AEI	3.44	0.120	-4.67	-10.54	Zeolite
AET	7.19	0.293	-5.26	-5.53	Zeolite
AET	7.19	0.291	-5.26	-5.53	Zeolite
APD	3.23	0.999	-39.91	-18.49	Zeolite
ATO	5.09	0.962	-18.85	-0.96	Zeolite
BEC	6.12	0.436	-6.43	-1.68	Zeolite
CAN	5.56	0.790	-13.06	-3.39	Zeolite
DON	7.67	0.317	-5.50	-5.14	Zeolite
EDI	3.04	0.025	16.21	-12.22	Zeolite
FAU	6.95	0.381	-3.44	-0.53	Zeolite
IRR	11.72	0.390	-3.79	-1.54	Zeolite
ISV	5.92	0.417	-6.18	-2.19	Zeolite

Continued on next page

Framework	Free sphere diam (Å)	Linear conversion	$\Delta\Delta H_{ads}$ (kJ mol^{-1})	$\Delta\Delta S_{ads}$ (J mol^{-1} K^{-1})	Material class
ITR	4.72	0.574	-9.48	-3.38	Zeolite
MAZ	7.10	0.289	-5.65	-5.84	Zeolite
MFI	4.25	0.498	-10.09	-6.58	Zeolite
MWW	4.12	0.220	-6.29	-7.67	Zeolite
OFF	6.21	0.427	-6.87	-3.01	Zeolite
OWE	3.39	0.204	-3.77	-14.23	Zeolite
SFE	5.81	0.338	-6.10	-5.24	Zeolite
SFG	4.98	0.419	-7.77	-5.38	Zeolite
SFO	6.55	0.303	-5.55	-5.41	Zeolite
VET	5.58	0.558	-9.32	-3.53	Zeolite
VFI	10.99	0.379	-3.86	-2.96	Zeolite
h8012441	2.80	0.805	-17.66	-22.98	Hyp. Zeolite
h8052601	2.80	0.336	3.18	-22.24	Hyp. Zeolite
h8059177	3.80	0.493	-6.56	-5.14	Hyp. Zeolite
h8080994	2.81	0.464	-3.95	-10.98	Hyp. Zeolite
h8104577	3.71	0.494	-6.77	-2.66	Hyp. Zeolite
h8130819	10.85	0.373	-3.13	-1.43	Hyp. Zeolite
h8158235	10.88	0.372	-3.31	-1.79	Hyp. Zeolite
h8160847	11.88	0.379	-2.93	-1.30	Hyp. Zeolite
h8177386	8.93	0.360	-3.92	-2.34	Hyp. Zeolite
h8186492	2.57	0.048	13.71	-42.39	Hyp. Zeolite
h8194727	8.03	0.302	-4.44	-3.34	Hyp. Zeolite
h8194988	10.82	0.379	-3.26	-1.85	Hyp. Zeolite
h8196690	14.96	0.384	-3.72	-3.42	Hyp. Zeolite
h8196730	6.17	0.294	-4.87	-3.86	Hyp. Zeolite
h8202766	10.08	0.376	-3.20	-2.09	Hyp. Zeolite
h8208342	6.98	0.279	-4.89	-4.32	Hyp. Zeolite
h8217568	7.80	0.321	-3.78	-3.07	Hyp. Zeolite
h8223482	4.66	0.490	-7.96	-5.95	Hyp. Zeolite
h8235482	7.00	0.326	-4.59	-3.29	Hyp. Zeolite
h8267101	6.26	0.380	-3.61	-1.81	Hyp. Zeolite
h8275748	14.53	0.379	-4.29	-4.14	Hyp. Zeolite
h8287168	13.03	0.384	-4.25	-4.16	Hyp. Zeolite
h8298141	12.42	0.390	-4.59	-4.43	Hyp. Zeolite
h8312533	16.14	0.392	-3.30	-3.05	Hyp. Zeolite
h8313092	23.01	0.395	-2.93	-2.37	Hyp. Zeolite
h8319194	19.48	0.380	-2.87	-2.34	Hyp. Zeolite
h8322962	20.37	0.397	-3.30	-2.97	Hyp. Zeolite
h8325731	28.44	0.395	-2.72	-2.13	Hyp. Zeolite
h8327476	18.07	0.396	-3.10	-2.36	Hyp. Zeolite

[a] $\Delta\Delta H_{ads} \equiv \langle \Delta H_{ads} \rangle_{linear} - \langle \Delta H_{ads} \rangle_{branched}$; [b] $\Delta\Delta S_{ads} \equiv \langle \Delta S_{ads} \rangle_{linear} - \langle \Delta S_{ads} \rangle_{branched}$.

Appendix B

Supporting Information for MOFs for THC sensing

B.1 Validation of THC Models on Mg-MOF-74

For a preliminary assessment of the ability of the different models, method and protocols to describe the adsorption of THC in microporous materials and MOFs, we investigated the well-studied Mg-MOF-74. This MOF was chosen because of its large channel diameter, which can host the bulky THC molecule, and because of the presence of strongly charged Mg open metal sites, which have a partial charge of $1.59\,e$ as computed with the DDEC protocol.[190] This allows us to asses the contribution of Coulombic interactions in the adsorption of THC, a weakly charged molecule (all partial charges are smaller than $0.16\,e$ in magnitude) within frameworks having strongly charged binding sites.

The THC-HEAD model was used for a preliminary simulations. Since the alkyl tail is charge-neutral, the THC-HEAD portion of the molecule is also neutral and therefore it can be used to assess the contribution of Coulombic interactions. We ran NVT Monte Carlo simulations at 309 K, the human body temperature, and at infinite dilution, *i.e.*, with one THC-HEAD particle per simulation box, for a total of $2 \cdot 10^6$ Monte Carlo steps (corresponding to 100 000 cycles of 20 steps each in RASPA). To equilibrate the system before the production, 10 000 cycles were added, *i.e.*, one tenth of the total number of steps. Each move was chosen from translation, rotation, and random insertion with equal probability. From the output of these calculations we observed that, while the acceptance ratios of translation and rotation moves are close to the 50%, the regrow acceptance ratio is only 4.8%. This means that it is particularly difficult for the THC molecule to find a new position in the pore volume that is not overlapping with the framework. Nonetheless, we determined that this move is reasonably explored in our $2 \cdot 10^6$ steps of simulation.

The average adsorption energy of THC in Mg-MOF-74 from the NVT simulation is $(-123.5 \pm 0.8)\,\mathrm{kJ\,mol^{-1}}$, where the contribution from the Coulombic interaction is less than 0.5%, while most of the adsorption energy comes from dispersion (van der Waals) interac-

tions. Indeed, a new calculation with the charges turned off resulted in an adsorption energy of $(-123.4 \pm 1.1)\,\mathrm{kJ\,mol^{-1}}$, and very similar acceptance ratios for the MC moves. It was therefore reasonable to neglect in the protocol Coulombic interactions even when strongly charged open metals site are present, as in the test case. This assumption has the twofold benefit of speeding up the MC simulations (in this case the same calculation without charges was about 3X faster) and avoiding the need to compute partial charges for the frameworks.

We next compared the rigid THC-HEAD rigid model with the flexible THC-FULL model that includes four coarse-grained sites to represent the alkyl tail. For this models we added the "reinsertion in place" step, where the algorithm attempts to regrow the alkyl tail from while keeping the aromatic head of the THC molecule fixed, occurring with the same probability as the other MC steps. The NVT calculation, with Coulomb interactions turned off, gave a resulting adsorption energy of $(-149.5 \pm 1.7)\,\mathrm{kJ\,mol^{-1}}$, *i.e.*, *ca.* $26\,\mathrm{kJ\,mol^{-1}}$ more favourable than using the THC-HEAD model. This difference is due to the additional dispersion interactions of the four beads of the tail with the framework. However, we can not assume a priori that the same difference would be found for all the frameworks. Indeed, even in MOFs with similar chemistries, where we might assume that the dispersion interactions are similar, there is the possibility that in some frameworks, the THC-HEAD model is confined in a small pore in such a way that there would be no room to grow the tail. The advantage, however, of using the rigid THC-HEAD particle is a speedup of *ca.* 2X times for the non-charged model. Moreover, one has to consider that the reinsertion moves are accepted more rarely using the full model: the acceptance ratios lower to 1.8% for reinsertion and 2.2% for reinsertion in place.

Finally, we compared the results from NVT simulations with Widom insertions: both methods are supposed to converge to the same adsorption energy, albeit faster in the first case, but the Widom insertion allows us to compute the Henry coefficient as well. This value quantifies the adsorption free energy at infinite dilution, including the entropy of adsorption which is expected to be largely influenced by the topology of the framework. As before, we tested the THC-HEAD and THC-FULL particles in the charged MOF-74, for 2 and 20 million (10X) Widom insertions. Results are summarized in Table B.1.

Table B.1: Comparison of the results from the simulation of THC-HEAD and THC-FULL in MOF-74 at 309 K, with Coulombic interactions turned off. Errors are computed from block averaging, dividing the simulation into 5 subsets. The number of MC steps (NVT moves or Widom insertions) are reported to assess the convergence of the simulation.

Description	**MC steps**	**THC-HEAD model**	**THC-FULL model**
Adsorption energy from NVT ($\mathrm{kJ\,mol^{-1}}$)	$2 \cdot 10^6$	-123.47 ± 0.81	-149.45 ± 1.67
Adsorption energy from NVT ($\mathrm{kJ\,mol^{-1}}$)	$2 \cdot 10^7$	-123.22 ± 0.54	-152.02 ± 1.84
Adsorption energy from Widom ($\mathrm{kJ\,mol^{-1}}$)	$2 \cdot 10^6$	-125.50 ± 1.68	-147.84 ± 5.09
Adsorption energy from Widom ($\mathrm{kJ\,mol^{-1}}$)	$2 \cdot 10^7$	-123.43 ± 2.86	-151.13 ± 3.07
Henry coefficient from Widom ($\mathrm{mol\,kg^{-1}\,Pa^{-1}}$)	$2 \cdot 10^6$	$(2.36 \pm 0.58) \cdot 10^9$	$(8.78 \pm 5.52) \cdot 10^9$
Henry coefficient from Widom ($\mathrm{mol\,kg^{-1}\,Pa^{-1}}$)	$2 \cdot 10^7$	$(1.65 \pm 0.56) \cdot 10^9$	$(12.50 \pm 4.29) \cdot 10^9$

The Widom insertion method has a large uncertainty, due to the very low probability of

finding, with random insertions, the favourable adsorption sites that significantly contribute to the averaging of the adsorption energy and the Henry coefficient. Table B.1 shows that, while for NVT the adsorption energy is already converged with $2 \cdot 10^6$ MC steps, more Widom insertions are necessary to achieve a comparable convergence. Moreover, the error computed for $2 \cdot 10^6$ insertions is not reliable, since this even increase when running 10X more insertions. The Henry coefficient also reflects this problem, as it is exponentially dependent on the adsorption energy. We can further evaluate the convergence behaviour in Figure B.2, where we show a plot of the Henry coefficient averaging during the simulation: one can note discontinuities in the cumulative average that correspond to a favourable insertion of the THC-HEAD particle in the framework, which are rare events.

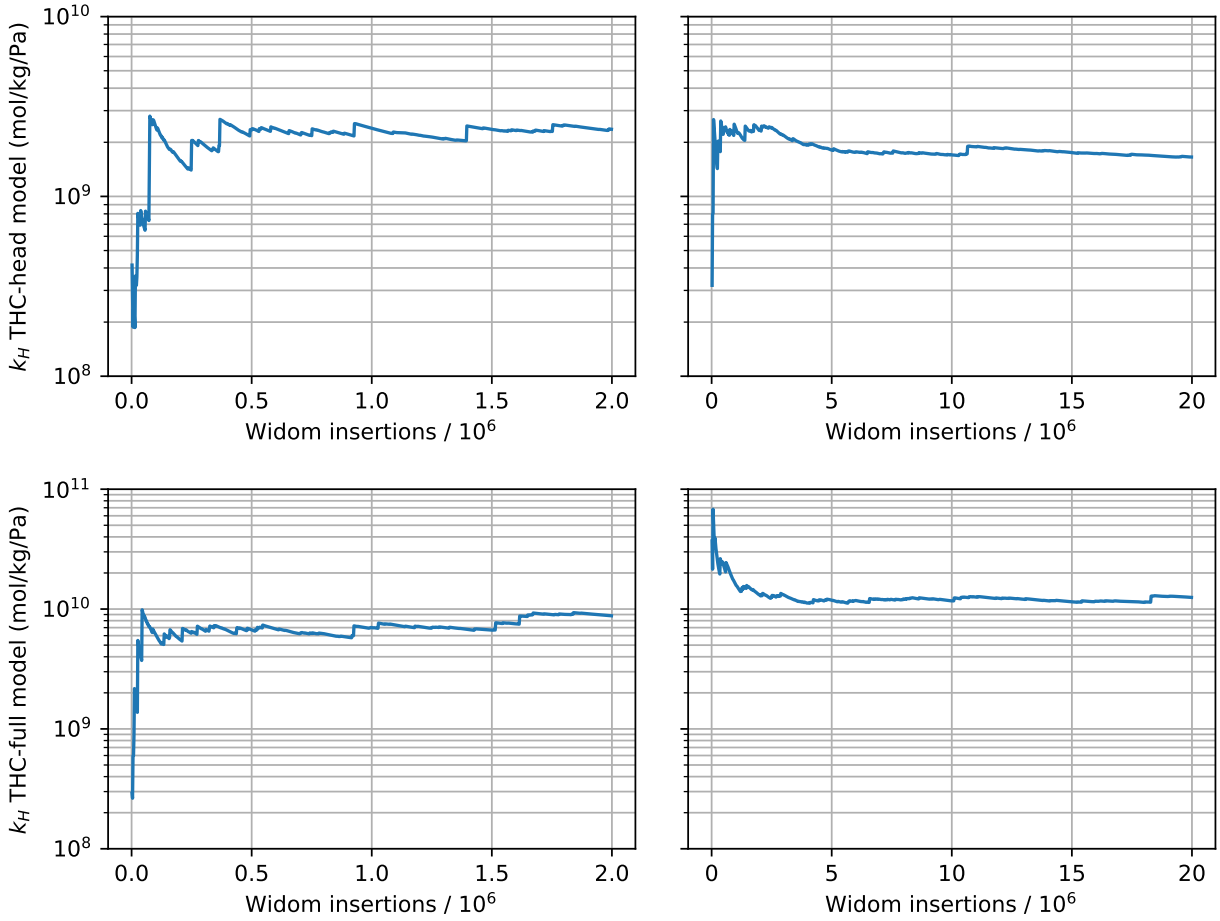

Figure B.1: Average Henry coefficient computed during Widom insertion simulations with $2 \cdot 10^6$ (left) and $2 \cdot 10^7$ (right) total insertions, from two independent run (*e.g.*, different random seeds). Results for the non-charged THC-HEAD (upper plot) and THC-FULL (lower plots) models are shown.

We can conclude that $2 \cdot 10^6$ steps are enough for the NVT simulations but not for Widom

insertions, where a 10X larger number of $2 \cdot 10^7$ insertions is needed to achieve a comparable convergence.

B.2 Timing of Different Methods and Models

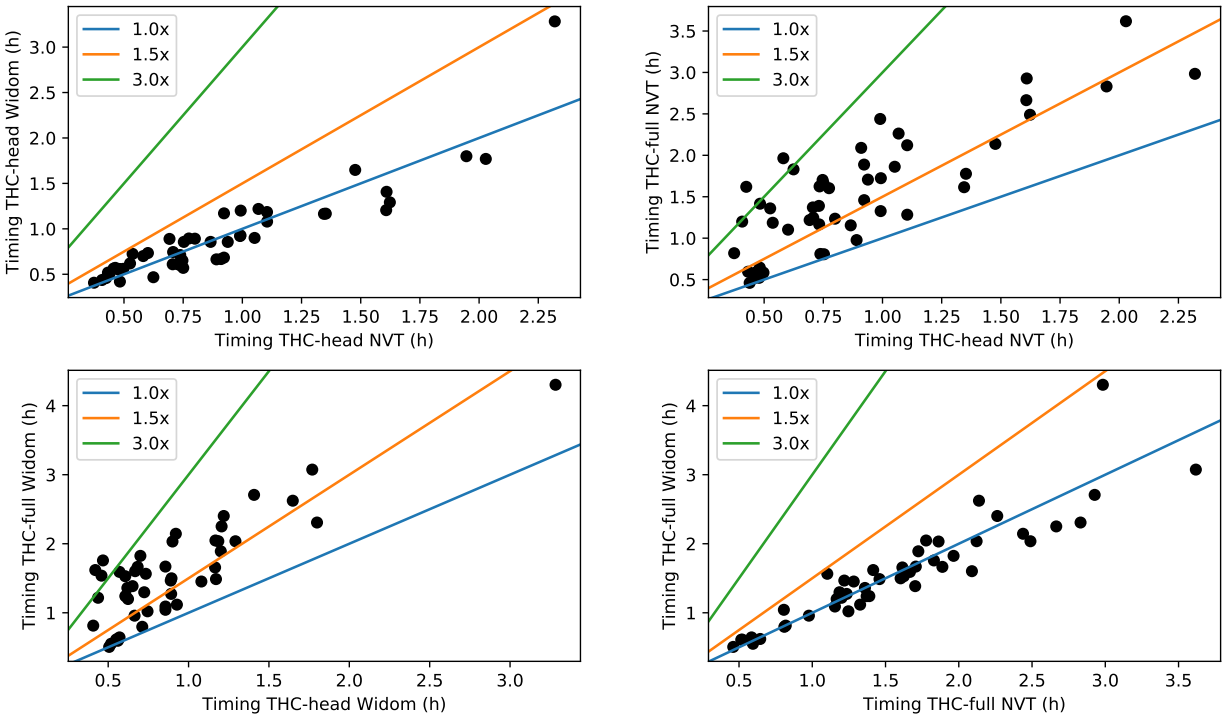

Figure B.2: Comparison of the timings for NVT vs Widom calculations (considering the same number of MC steps, 200 000) and THC-HEAD vs. THC-FULL models. The benchmark was run for 50 MOFs, on the same processor. Note that there is not a significant change in time when using NVT or Widom simulations. However, when using the THC-FULL model, the computational cost can be more than 3 times higher than using the THC-HEAD model.

B.3 Inspection of THC Binding Sites in Additional MOFs

In the main text we showed the location of THC in the pores of six MOFs that were selected because of their high affinity with the molecule and the clear presence of one of the three motifs (*i.e.*, "narrow channels," "thick walls," or "parking spots"). We show here the binding

sites of the remaining MOFs that we highlighted because of their high Henry coefficients at different ranges of the pore limiting diameter.

- AMIMEP (Fig. B.3) has the same topology and chemistry as AMILUE (shown in the main text). Similarly, the main motif found is "thick walls."
- AXINAX01 (Fig. B.3) has small cages where the THC can access from the main channels and that perfectly fit the molecule. The main motif is "parking spots."
- CAVMOD (Fig. B.3) has two layers of ligands separating the one-dimensional channels. The main motif is "thick walls."
- FAYQUT (Fig. B.4) has smaller pores that fit tightly the THC molecults. The main motif is "parking spots."
- FIHHUB (Fig. B.4) has a topology that resembles BAZJET, but in this MOF the slits have the same orientation of the channel (while in BAZJET they are perpendicular). The main motif is "parking spots."
- HIFGIO (Fig. B.4) has a PLD of 11.67 Å and long slits along the channels where THC can fits. The main motif is "parking spots."
- MAYKOO (Fig. B.5) has small slits on the said of the main channels. This MOF is a good example of the "parking spots" motif.
- NIGDEO (Fig. B.5) has a PLD of only 7.14 Å due to its zig-zag channels. However, the overlap is less than 3 $Å^2$ and therefore we consider that THC can percolate though the channel. Even if the channels are not particularly wide, considering the slits where the THC finally adsorbs, the matching motif is the "parking spots."
- NIGDIS (Fig. B.5) is the analog of NIGDEO and also the same adsorption motif (PLD of 7.14 Å).
- WAMREJ (Fig. B.6) has semi-open cages that can favourably host THC. We recognize both the "thick wall" and "parking spots" motifs.
- YUXQIS (Fig. B.6) has a structure very similar to FIHHUB. Therefore, the main motif is "parking spots."

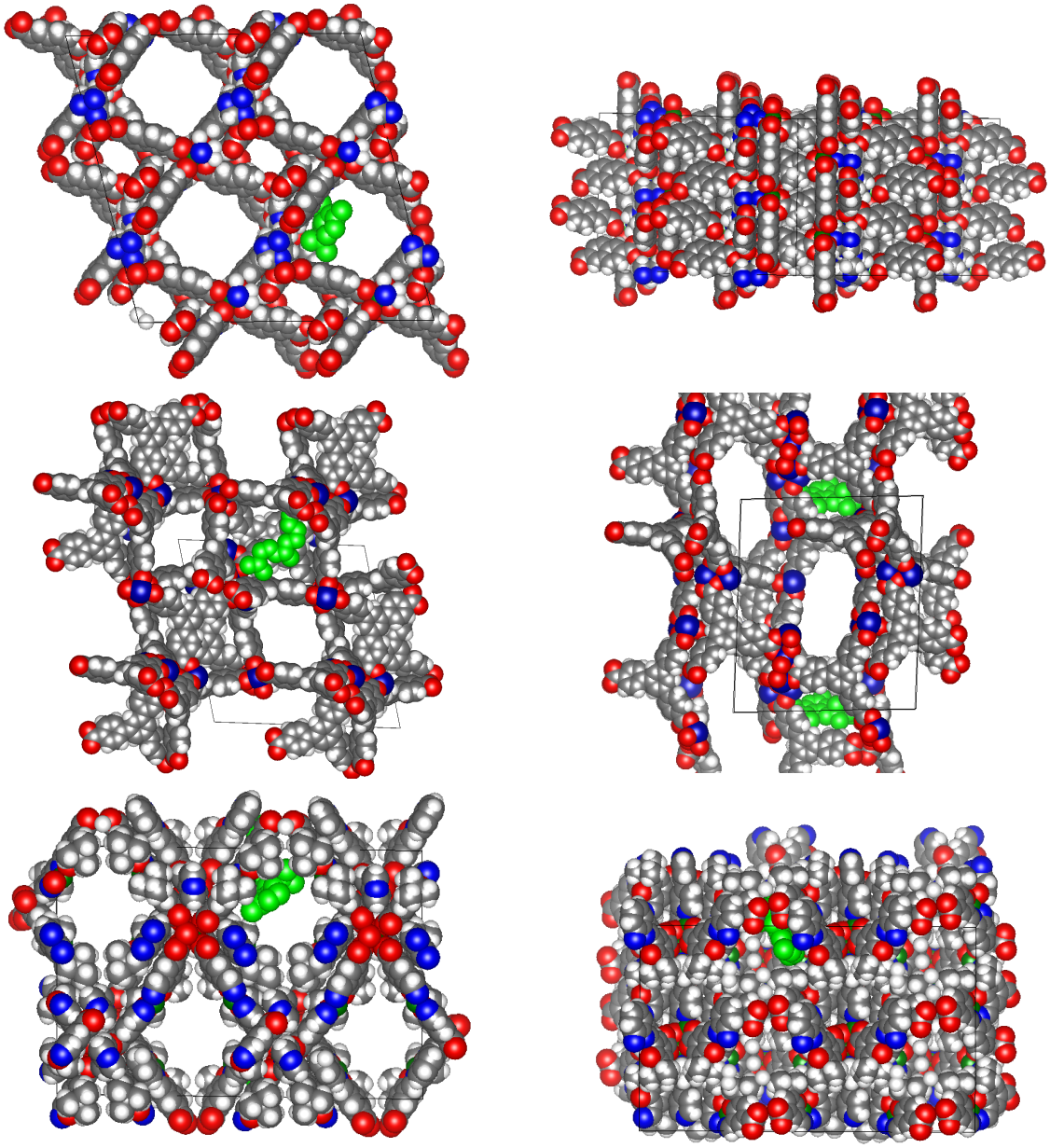

Figure B.3: Top (left) and side (right) views of AMIMEP (upper), AXINAX01 (middle) and CAVMOD (lower) MOFs. THC is colored in green.

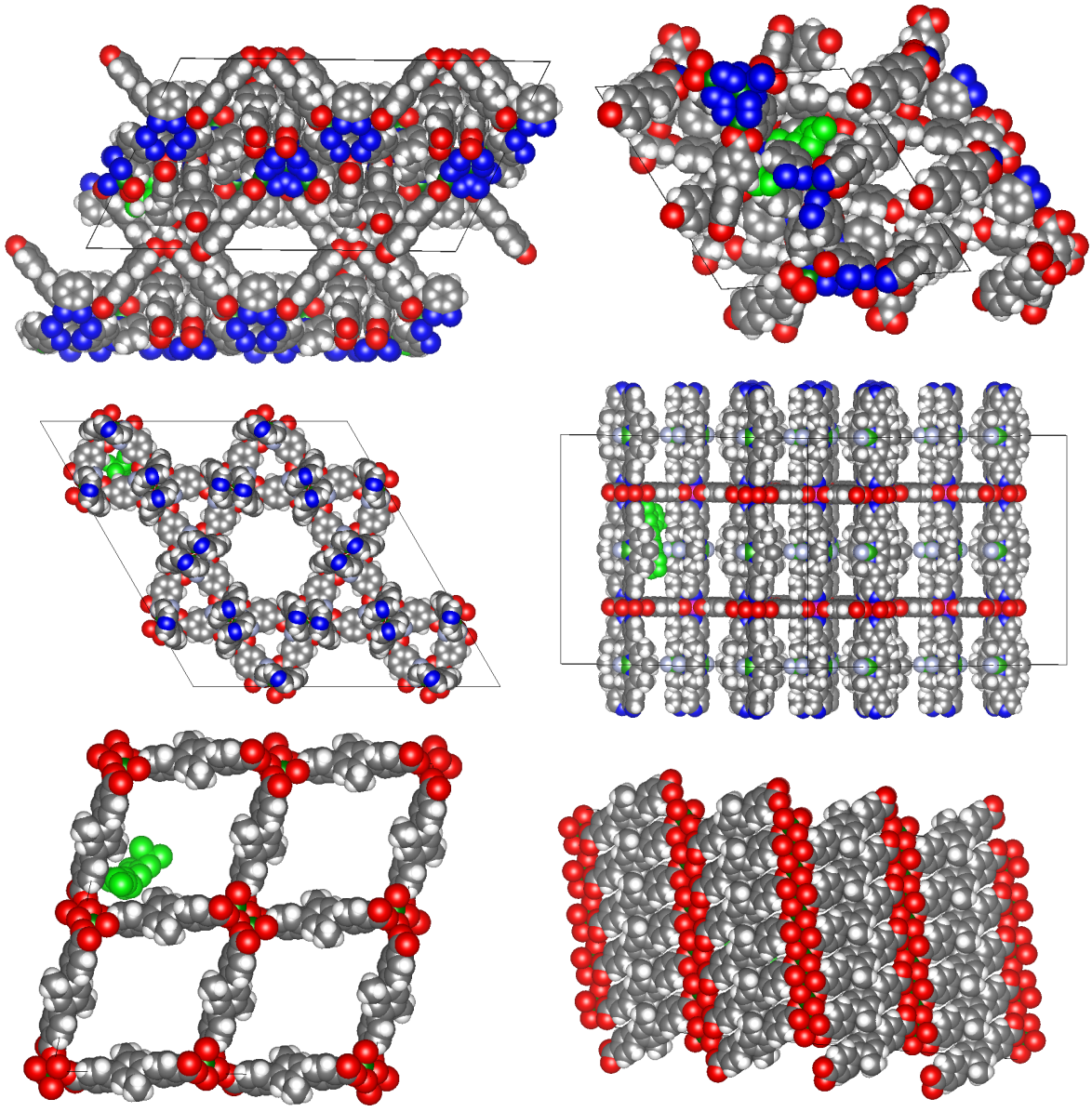

Figure B.4: Top (left) and side (right) views of FAYQUT (upper), FIHHUB (middle) and HIFGIO (lower) MOFs. THC is colored in green.

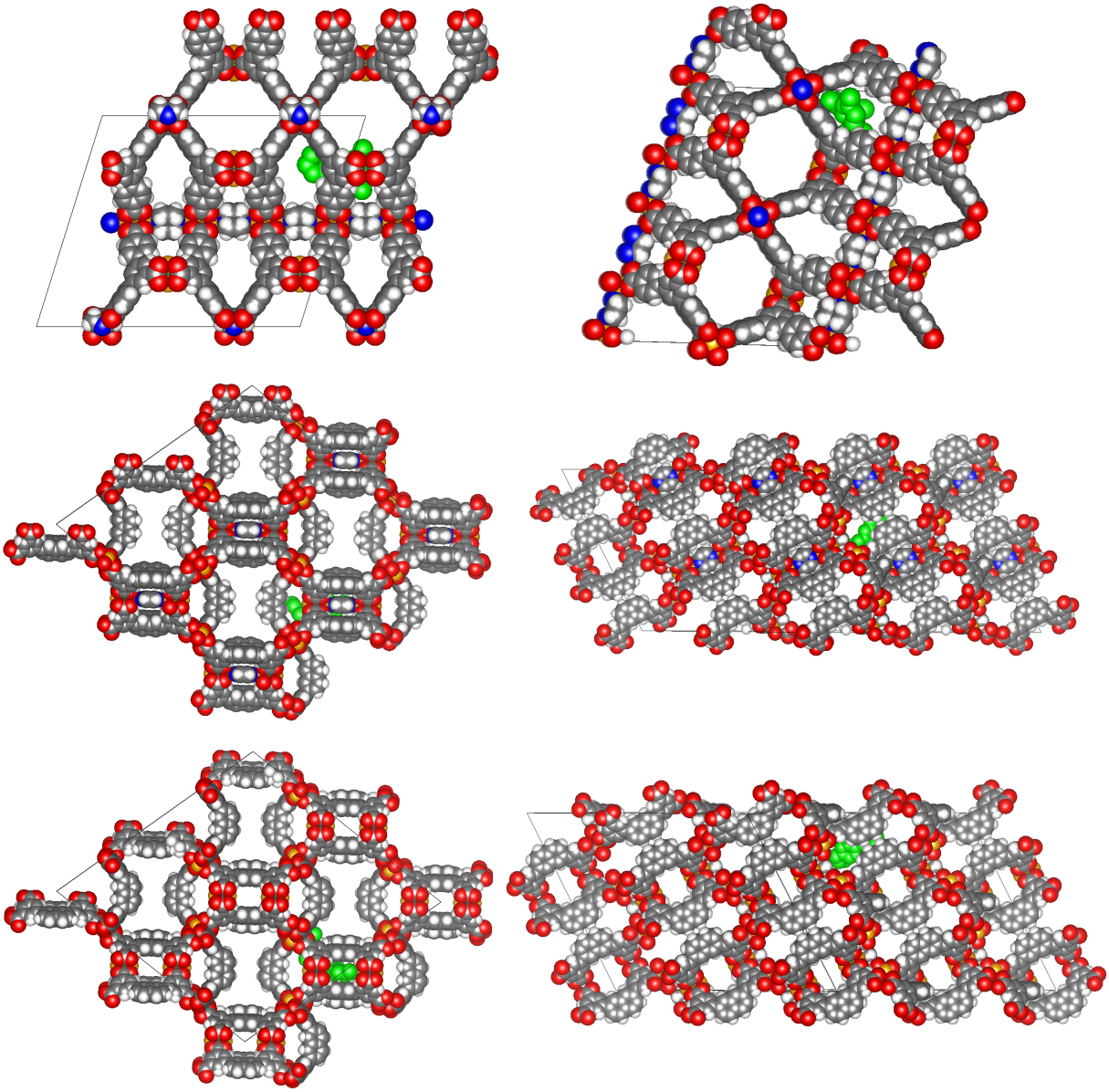

Figure B.5: Top (left) and side (right) views of MAYKOO (upper), NIGDEO (middle) and NIGDIS (lower) MOFs. THC is colored in green.

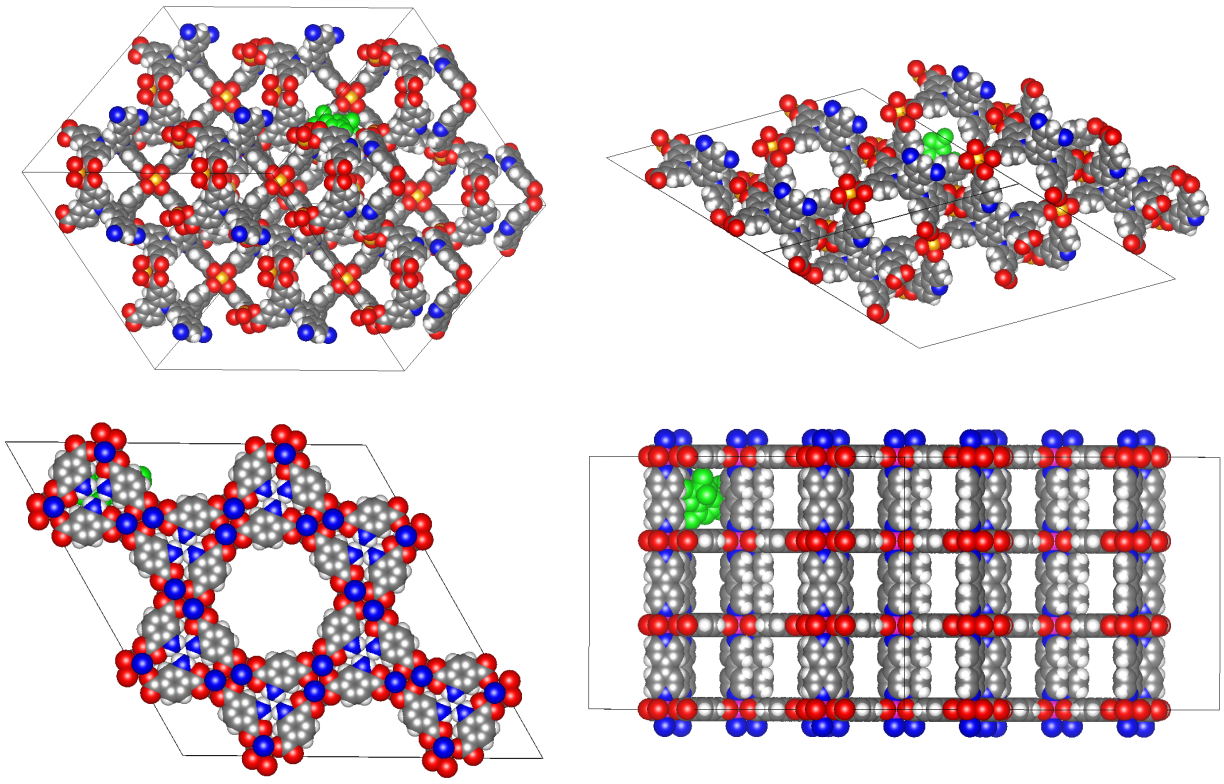

Figure B.6: Top (left) and side (right) views of WAMREJ (upper) and YUXQIS (lower) MOFs. THC is colored in green.

Appendix C

Supporting Information for Zeolite-Templated Carbon EDLCs

C.1 Model and Force Field Parameters

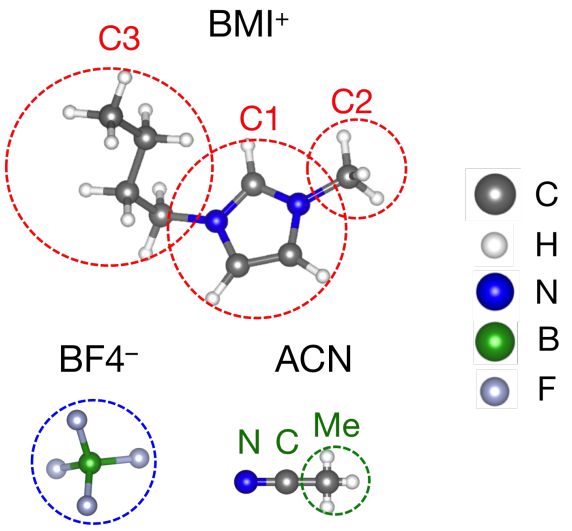

Figure C.1: Definitions of coarse-grained sites of the electrolyte model used in this work. For BMI^+, C1 represented the imidazole, C2 the methyl group, and C3 the butyl tail.

Force field parameters for the electrode carbon atoms: $\sigma = 3.37\,\text{Å}$ and $\varepsilon = 0.23\,\text{kJ mol}^{-1}$.

In the constant-potential method,[163,164] implemented as a LAMMPS package,[173] an applied potential $\Delta\Psi = \Psi^+ - \Psi^-$ was imposed on each atom by solving the following equation (the definition of electric potential) for charge, q_i, on each electrode atom i:

$$\Psi_i = \Psi^{+/-} = \frac{\partial U}{\partial q_i}\,, \tag{C.1}$$

Table C.1: Force field parameters for BMI^+, BF_4^-, and ACN used in this work.[8,159,160]

	C1	C2	C3	BF_4^-	N	C	Me
x (Å)	0.000	0.000	0.000	0.000	0.000	0.000	0.000
y (Å)	-0.527	1.641	0.187	0.000	0.000	0.000	0.000
z (Å)	1.365	2.987	-2.389	0.000	0.000	1.17	2.63
q (e)	0.4374	0.1578	0.1848	-0.78	-0.398	0.129	0.269
M ($\mathrm{g\,mol^{-1}}$)	67.07	15.04	57.12	86.81	14.01	12.01	15.04
σ_i (Å)	4.38	3.41	5.04	4.51	3.30	3.40	3.60
ε_i ($\mathrm{kJ\,mol^{-1}}$)	2.56	0.36	1.83	3.24	0.42	0.42	1.59

where U is the potential energy arising from electrostatic interactions in the system. The potential at electrode atom i, Ψ_i, can be expressed as the sum of short-range and long-range contributions, with correction terms for self-self interactions and the slab geometry of the EDLC cell. The potential at a given electrode atom due to interactions from other electrode atoms j and electrolyte atoms k, with partial charges Q_j and q_k, respectively, can be written as

$$\Psi_i = \sum_i^n a_{ij} Q_j + \sum_k^m b_{ij} q_k \,. \tag{C.2}$$

Equation C.2 is a system of linear equations depending on fixed quantities (electrolyte atomic charges, electrode positions), and variable quantities (electrolyte positions, electrode atomic charges). At each timestep the electrolyte positions are first time-integrated, and then Equation C.1 is solved for the electrode atomic charges.

C.2 ZTC Structures and Pore Properties

The 27 ZTCs presented in this study are listed in Table C.2 below.

Table C.2: Names of ZTCs in our screening library, along with the pore limiting diameter (PLD) and accessible surface area (ASA).

Name (this study)	Name (Braun et al.)[158]	PLD [Å]	ASA [$m^2\,g^{-1}$]
221_2_6	221_2_6	10.34449	741.458
BEA	BEA	6.30436	697.465
BEA_beta	BEA_beta	6.44968	751.289
BEC	BEC	6.74316	399.491
EMT	EMT	9.09042	2269.26
FAU_1	FAU_Si_1	9.22447	6901.53
FAU_2	FAU_Si_2	9.95594	605.043
FAU_3	FAU_3	9.59433	590.964
h18	h8331018	10.82144	1357.28
h29	h8326829	6.2254	775.736
h36	h8326836	8.35197	929.784
h37	h8326837	8.73394	505.004
h49	h8326849	10.33919	694.524
h91	h8327291	8.85173	724.387
h96	h8326896	10.92387	889.733
IRR_2	IRR_2	6.29144	2695.26
IRR_3	IRR_3	7.01787	676.508
IRY	IRY	7.57423	889.26
ISV	ISV	7.52015	786.033
ITT	ITT	4.79864	481.079
IWS_2	IWS_2	5.93863	1457.52
IWS	IWS	7.30105	1633.33
POS	POS	6.21129	707.693
RWY	RWY	3.78258	329.903
SAO	SAO	7.09575	683.74
SBS	SBS	6.3981	1190.58
SBT_2	SBT_2	5.8204	1793.17

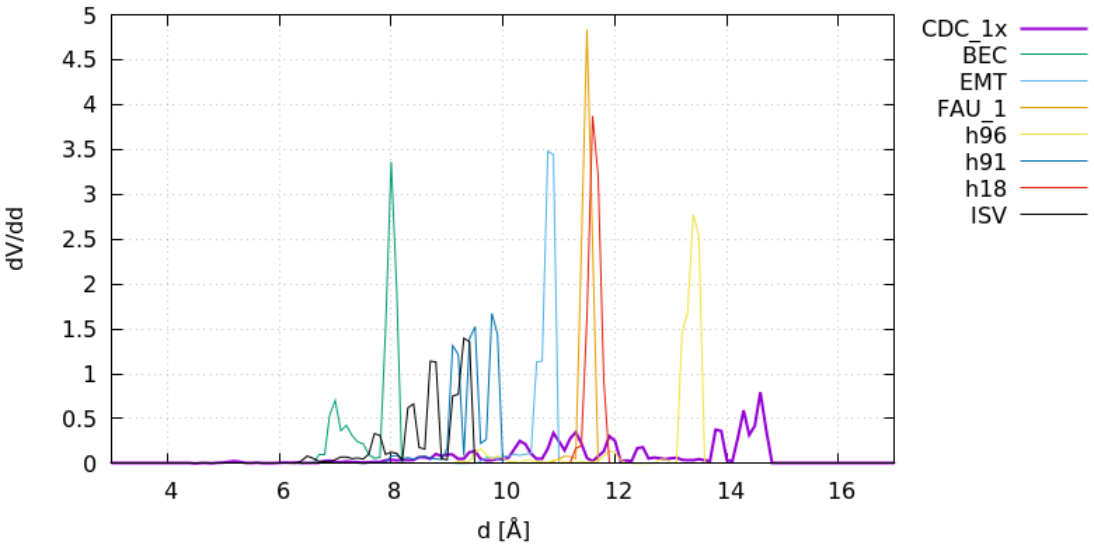

Figure C.2: Pore sizes distributions of selected CDC and ZTC materials.

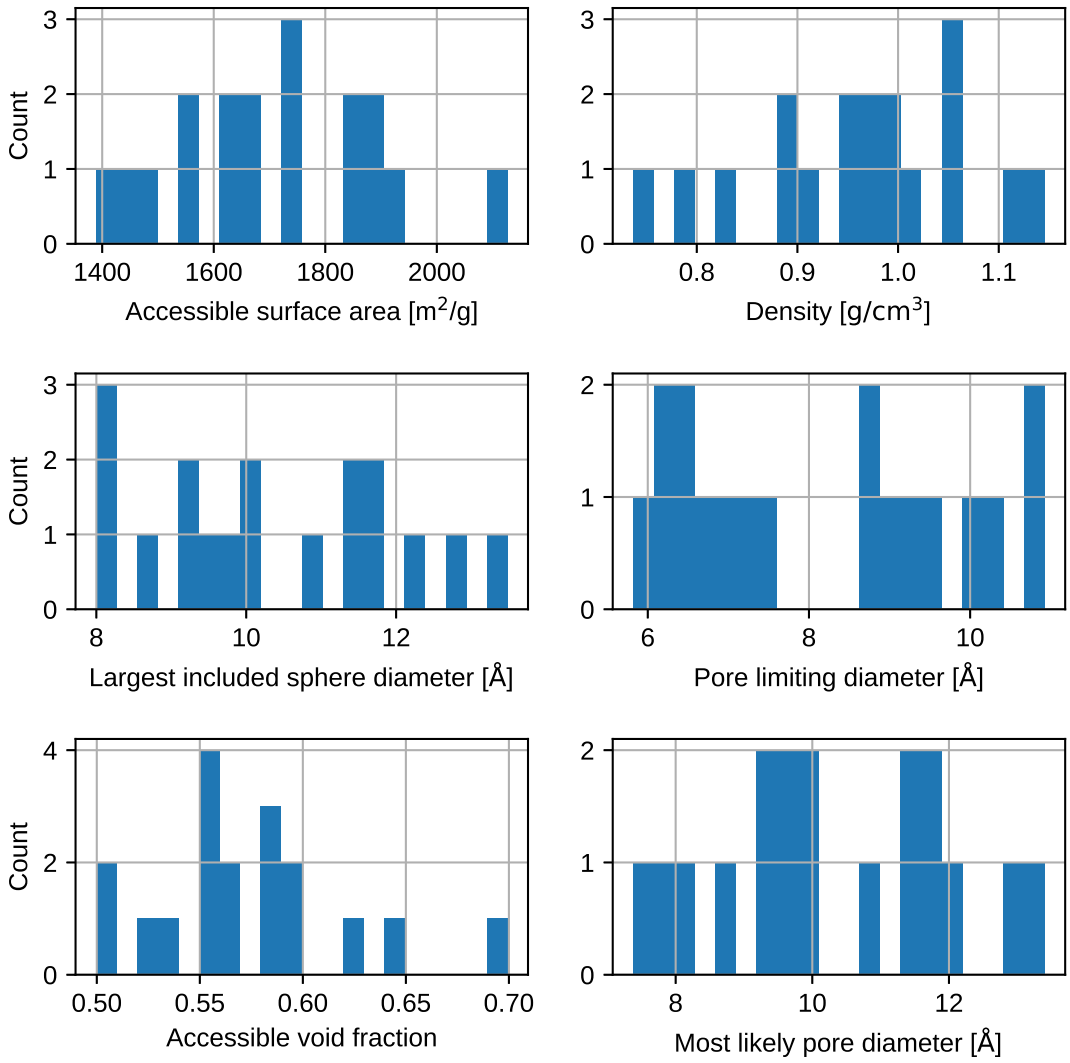

Figure C.3: Histograms of ZTC properties. Most common pore size is defined as the position of the highest peak in the pore size distribution.

C.3 EDLC Simulation Cells

The protocol we used for building simulation cells is as follows:

1. Compute probe-occupiable accessible volume (POAV) of EDLC electrode materials using a 1.86 Å nitrogen probe.[106] We note that this probe radius was chosen, rather than the larger radii of the electrolyte molecules, because it was found to yield electrolyte densities consistent with experimental densities. When the POAV was also computed using a probe size of 2.73 Å, the minimal radius of gyration of the BMI^+, some materials had with a POAV of 0, implying that BMI^+ would not be able to enter the pores at all. However, simulations showed that BMI^+ was, in fact able to enter the pores of these materials.

2. Replicate the unit cell of the ZTC so that it is at least 35 Å in length.*

3. Compute the amount of solvent needed to fill the POAV of both electrodes (using the bulk density of the electrolyte) as well as an inter-electrode spacing of 85 Å or greater in the z direction.†

4. Add graphene caps on both sides of the cell. These caps are 2 Å away from the edge of the electrodes and 1 Å away from the edge of the unit cell. This prevents electrolyte molecules from leaving the simulation cell through the end of the capacitor cell, as the simulation box is non-periodic in the direction perpendicular to the electrodes.

The resulting simulation cells had electrode dimensions of 39.34 Å to 69.80 Å, and bulk phase dimensions of 88.38 Å to 127.15 Å.

C.4 Constant-Charge Pre-Equilibration and Equivalent Constant Potential

For an 8 ns equilibration time, the Poisson potential drop across the cell differed by less than 10% over three runs (Figure C.4a), while a Poisson potential averaged over just 2 ns has an error of 30% compared to the 8 ns Poisson potential (Figure C.4b).

Table C.3 provides 1-D Poisson potential drops computed from an 8 ns simulation at constant charge, with a charge of $0.01\,e$ applied to anode atoms and $-0.01\,e$ to cathode atoms.

*This minimum length was selected to yield EDLC cells which were similar in dimension to those used in Merlet et al.[8], as well as to limit the total number of atoms for less expensive simulations.

†See previous note.

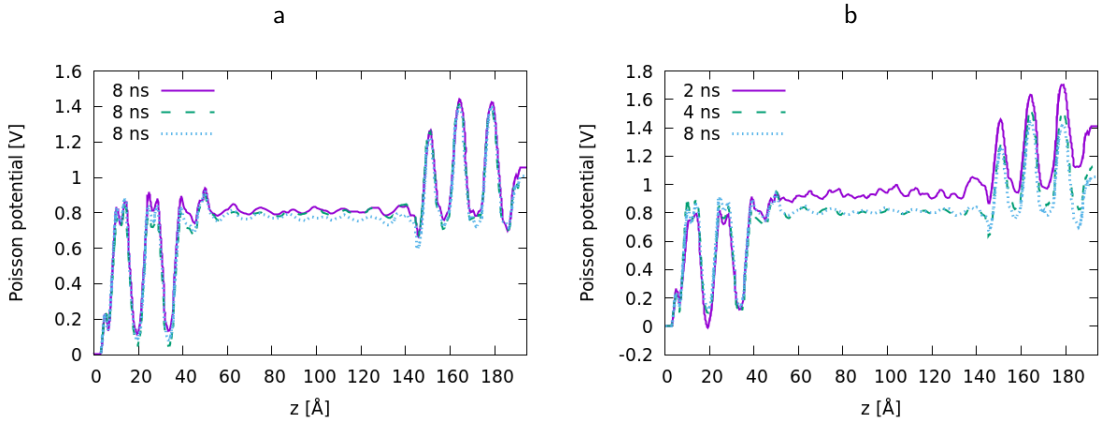

Figure C.4: a, Poisson potential for three independent 8 ns simulations with a constant electrode charge of $\pm 0.01\,e$. b, convergence of Poisson potential in FAU_1 with increasing constant-charge simulation. It is clear that the Poisson potential is not constant throughout the electrodes, making it difficult to determine a reference potential for integration of the charge density.

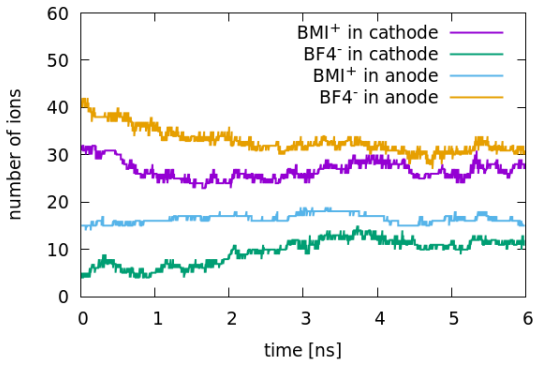

Figure C.5: Time evolution of the number of BMI^+ and BF_4^- electrodes inside the electrodes in the FAU_1 EDLC over 6 ns, simulated with a constant potential of 1.06 V.

Table C.3: Poisson potential drops computed from an 8 ns constant-charge simulation.

Structure	$\Delta\Psi$ [V]
CDC_1x	2.380000
CDC_4x	2.790000
221_2_6	-0.095215
BEA	0.747600
BEA_beta	0.576139
BEC	0.501250
EMT	0.778107
FAU_3	0.849142
FAU_Si_1	1.124562
FAU_Si_2	0.681612
h8326829	0.907328
h8326836	-0.324666
h8326837	0.281436
h8326849	-0.035891
h8326896	-0.079104
h8327291	0.995776
h8331018	0.210162
IRR_2	1.663953
IRR_3	1.485333
IRY	1.017175
ISV	0.083800
ITT	4.339743
IWS	0.463539
IWS_2	1.571766
POS	1.390439
RWY	21.399038
SAO	0.509673
SBS	-0.081316
SBT_2	0.119608

C.5 Computation of Interfacial Properties

The coordination shell of an ion is defined in this work with a cutoff distance of 6.3 Å, the first minimum of the ion-carbon RDF. This was the same distance used in Merlet et al. for the coordination shell.[147]

The degree of confinement (DoC), defined as the fraction of the maximum solid angle around an ion which is occupied by carbon atoms, was computed as in Merlet et al.[147] The charge compensation per carbon (CCpC) is defined as the net charge per carbon in the coordination shell of a counterion. It is therefore only computed for anions within the positive electrode (anode) and for cations within the negative electrode (cathode).

C.6 Density of Electrolyte in Pores

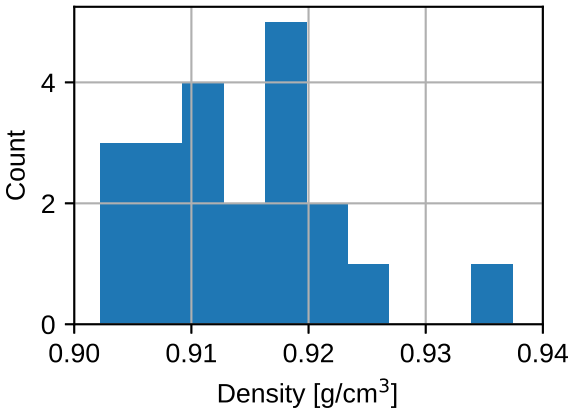

Figure C.6: Densities computed in bulk solvent region of EDLC cell during a constant-potential simulation with an applied voltage difference of 1 V.

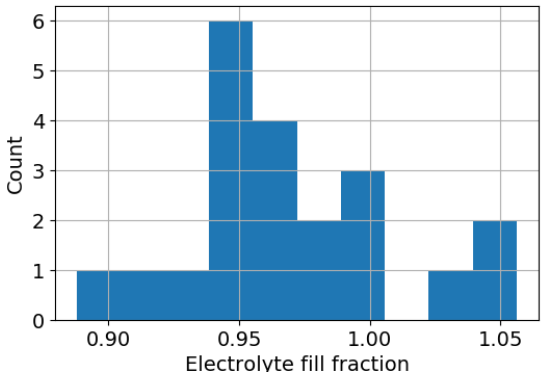

Figure C.7: Fill fraction in electrodes of EDLC cell during a constant-potential simulation with an applied voltage difference of 1 V.

C.7 Charging Dynamics

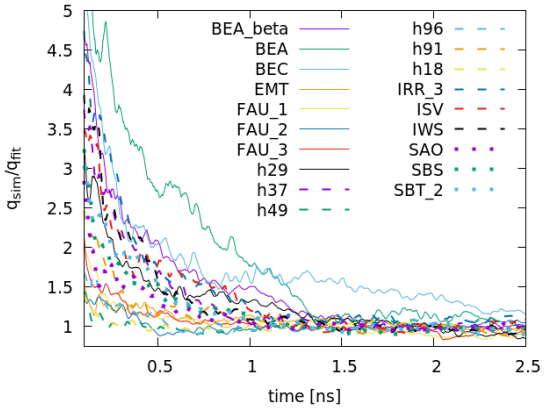

Figure C.8: Ratio between the simulated electrode charge per atom and the exponential fit. The data are filtered using a window of 50 ps to remove noise.

The electrode charging exhibits multiple timescales which are not captured by the single-exponential charging of an ideal RC circuit. Modeling the system with additional RC elements, as in a transmission line model, would better capture charging dynamics, especially since we observe that the electrodes charge progressively, starting from the electrode-bulk interface (outer slice) and moving inward (inner slice) (Figure C.9a). This spatially progressive charging is a key characteristic of the transmission line model, and is more marked in the materials with smaller pores since slower ion diffusion creates a bigger difference between charging times for the outer and inner regions of the electrode.

We observe that in many of the structures, particularly in the outer slice, the total ion occupancy (defined as the sum of anions and cations in the defined region) exhibits a maximum value during charging which is higher than the equilibrated value, suggesting that the electrolyte molecules may encounter kinetic trapping as counter-ions enter the pores (Figure C.9b and C.9c). The increase of counter-ions in the pores allows for faster-than-exponential charging upon initial application of a potential difference, but then the local density increase makes it more difficult for co-ions to diffuse out of the electrode, slowing further charging. This phenomenon is similar to the "overfilling" observed by Kondrat et al., in which the total number of ions inside the pore during the course of charging reaches values higher than the steady-state value.[149]

If the initial charging period after the constant potential is characterized by kinetic trapping, then we should see that the charging profile in this initial period differs between independent charging cycles of the same EDLC. When fit to an exponential, independent runs may have different τ as this is determined by dynamic processes during charging, but they should have similar Q_{inf}. In order to test this we generated independent configurations of the 19 ZTCs from zero-charge runs, and repeated constant-potential simulations to compare the

charging curves of the independent runs. These results, shown in Figure C.10, demonstrate that there is indeed more reproducibility in the maximum charge than in the charging rate between independent runs. While all but four of the maximum charges are within 10% of each other (the shaded region) in independent runs, two-thirds of the materials have time constants that are more than 10% different from each other.

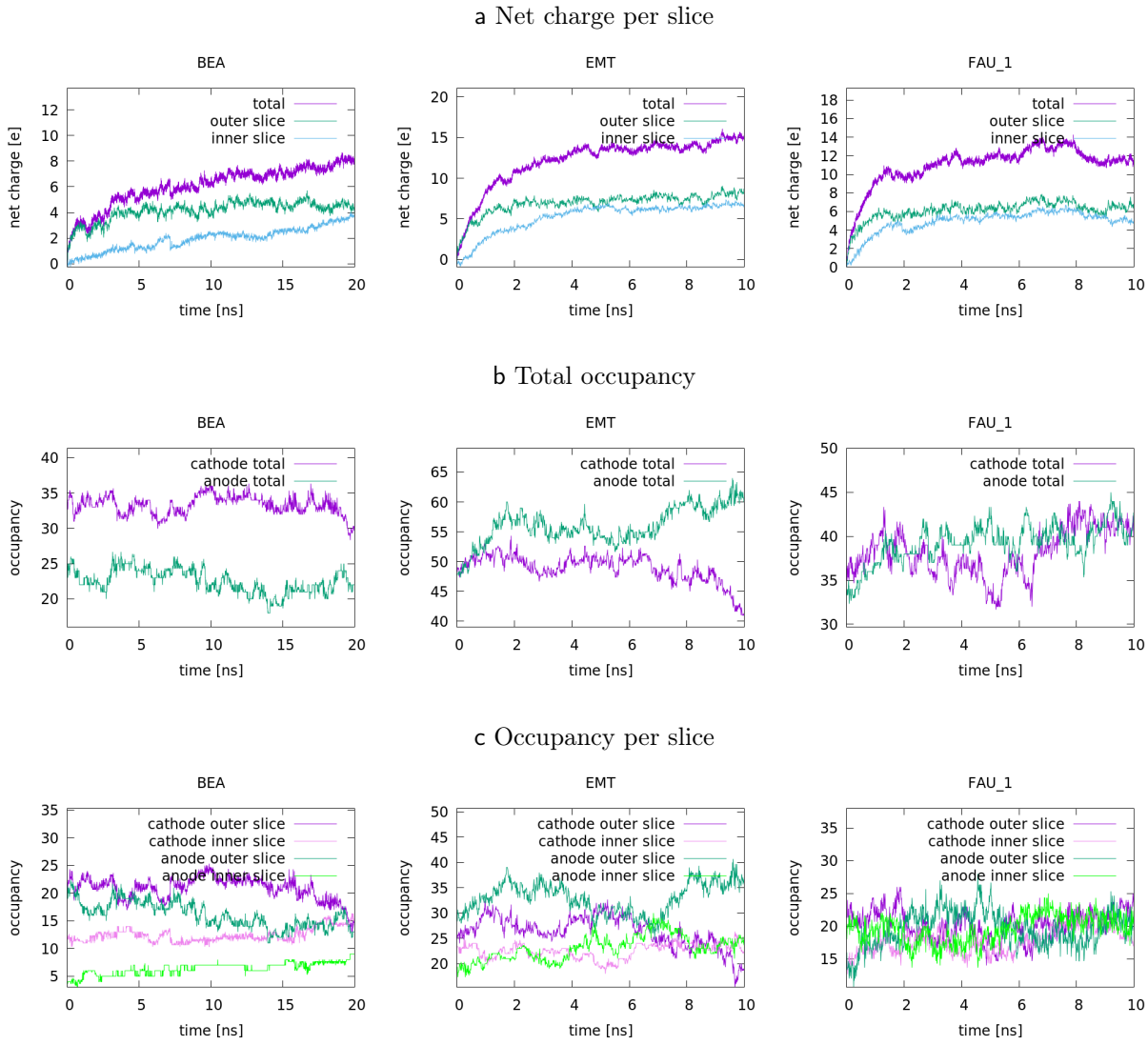

Figure C.9: Net charge and occupancy (total number of ions) during constant-potential charging. Note that the total ion occupancies fluctuate, both in constant-charge and constant-potential simulations; the net charge results from the difference between the numbers of positive and negative ions.

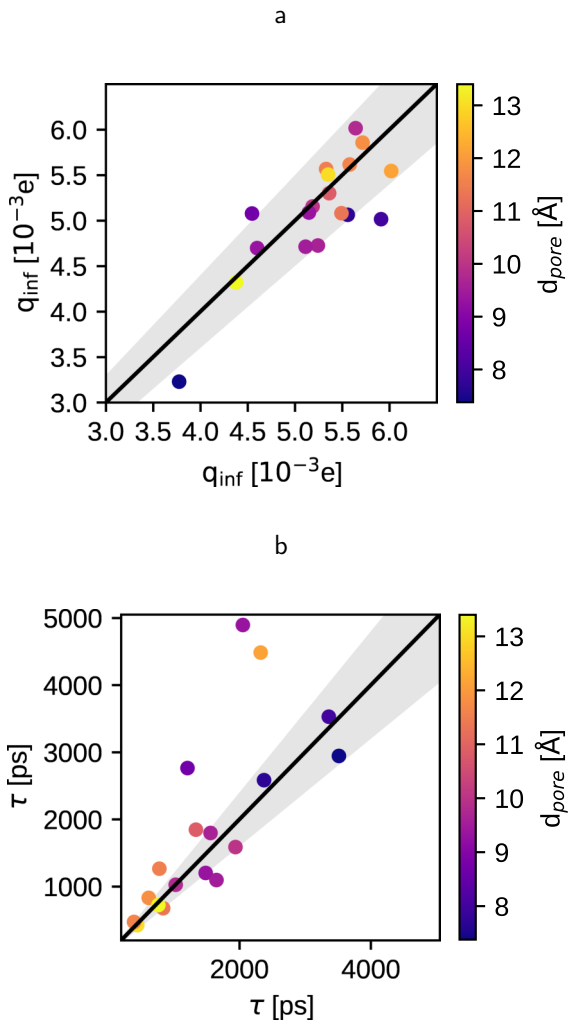

Figure C.10: a, maximum charge q_{inf} and b, time constant τ of EDLC charging between two independent constant-potential runs. The points are colored by the average pore diameter. The gray shaded regions represent a window of 10% and 20% deviation between the independent runs for τ and q_{inf}, respectively.

C.8 Additional Charge Storage and Interfacial Properties Data

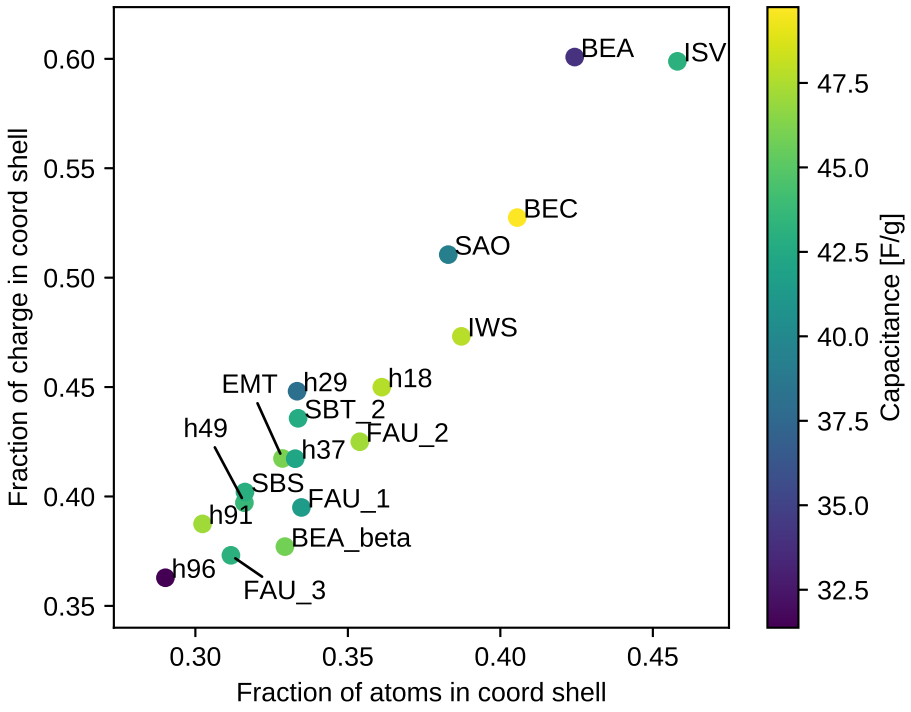

Figure C.11: Fraction of charge vs. fraction of atoms in the coordination shell of counterions in the anode.

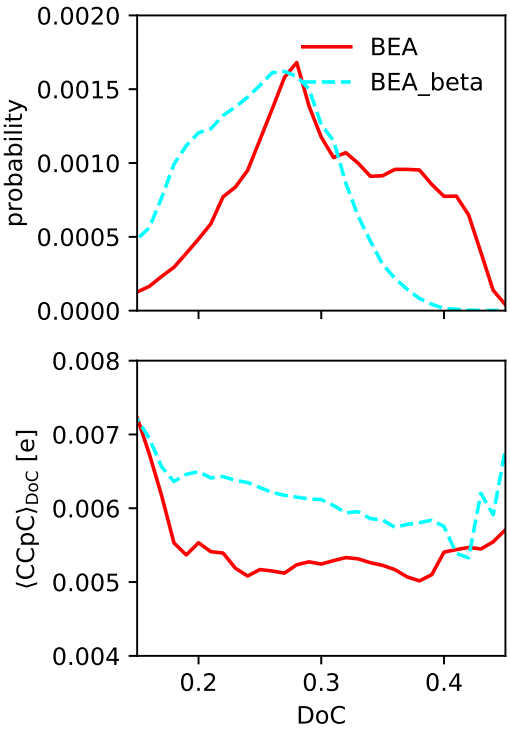

Figure C.12: DoC and CCpC of the cation by the cathode in BEA and BEA_beta.

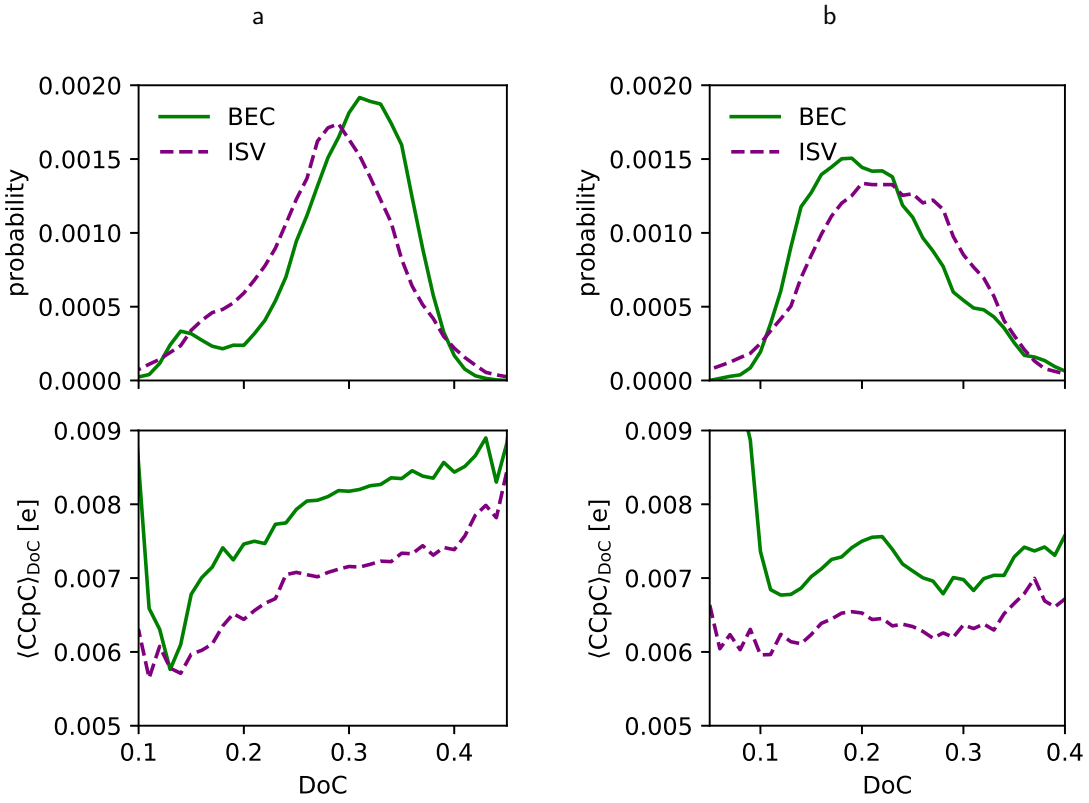

Figure C.13: a, DoC and CCpC of the anion by the anode and, b, of the cation by the cathode in BEC and ISV.

References

1. Krishna, R. & van Baten, J. M. In silico screening of metal-organic frameworks in separation applications. *Phys. Chem. Chem. Phys.* **13,** 10593 (2011).
2. Li, J.-R., Sculley, J. & Zhou, H.-C. Metal-Organic Frameworks for Separations. *Chem. Rev.* **112,** 869–932. http://pubs.acs.org/doi/10.1021/cr200190s (Feb. 2012).
3. Bloch, E. D., Queen, W. L., Krishna, R., Zadrozny, J. M., Brown, C. M. & Long, J. R. Hydrocarbon Separations in a Metal-Organic Framework with Open Iron(II) Coordination Sites. *Science* **335,** 1606–1610. http://www.sciencemag.org/cgi/doi/10.1126/science.1217544 (Mar. 2012).
4. Kim, J., Lin, L.-C., Martin, R. L., Swisher, J. A., Haranczyk, M. & Smit, B. Large-scale computational screening of zeolites for ethane/ethene separation. *Langmuir* **28,** 11914–9. http://www.ncbi.nlm.nih.gov/pubmed/22784373 (Aug. 2012).
5. Liu, J., Chen, L., Cui, H., Zhang, J., Zhang, L. & Su, C.-Y. Applications of metal–organic frameworks in heterogeneous supramolecular catalysis. *Chem. Soc. Rev.* **43,** 6011–6061 (2014).
6. Mlinar, A. N., Keitz, B. K., Gygi, D., Bloch, E. D., Long, J. R. & Bell, A. T. Selective propene oligomerization with nickel(II)-based metal-organic frameworks. *ACS Catal.* **4,** 717–721. arXiv: arXiv:1408.1149 (2014).
7. Nishihara, H. & Kyotani, T. Templated Nanocarbons for Energy Storage. *Adv. Mater.* **24,** 4473–4498. http://doi.wiley.com/10.1002/adma.201201715 (Aug. 2012).
8. Merlet, C., Rotenberg, B., Madden, P. A., Taberna, P.-L., Simon, P., Gogotsi, Y. & Salanne, M. On the molecular origin of supercapacitance in nanoporous carbon electrodes. *Nat. Mater.* **11,** 306–310. http://www.nature.com/doifinder/10.1038/nmat3260 (2012).
9. Salunkhe, R. R., Lee, Y.-H., Chang, K.-H., Li, J.-M., Simon, P., Tang, J., Torad, N. L., Hu, C.-C. & Yamauchi, Y. Nanoarchitectured Graphene-Based Supercapacitors for Next-Generation Energy-Storage Applications. *Chem. - A Eur. J.* **20,** 13838–13852. http://doi.wiley.com/10.1002/chem.201403649 (Oct. 2014).
10. Kondrat, S. & Kornyshev, A. A. Pressing a spring: What does it take to maximize the energy storage in nanoporous supercapacitors? *Nanoscale Horizons* **1,** 45–52 (2016).

11. Wang, H., Zhu, Q.-L., Zou, R. & Xu, Q. Metal-Organic Frameworks for Energy Applications. *Chem* **2,** 52–80. http://linkinghub.elsevier.com/retrieve/pii/S2451929416302674 (2017).

12. Chandra, S., Roy Chowdhury, D., Addicoat, M., Heine, T., Paul, A. & Banerjee, R. Molecular Level Control on the Capacitance of Two-Dimensional Covalent Organic Frameworks: The Role of H-bonding in Energy Storage Materials. *Chem. Mater.* acs.chemmater.6b04178. http://pubs.acs.org/doi/abs/10.1021/acs.chemmater.6b04178 (2017).

13. Cronstedt, A. F. Observation and description of an unknown mineral species, called zeolite (RÖN och BESKRIFNING Om en oberkant barg art, som kallas Zeolites). *Sven. Vetenskaps Akad. Handl. Stock.* **17,** 120 (1756).

14. Flanigen, E. M. in *Stud. Surf. Sci. Catal.* C, 13–34 (1991). https://linkinghub.elsevier.com/retrieve/pii/S0167299108635995.

15. Maesen, T. & Marcus, B. in *Stud. Surf. Sci. Catal.* C, 1–9 (2001). https://linkinghub.elsevier.com/retrieve/pii/S0167299101802421.

16. Baerlocher, C. & McCusker, L. B. *Database of Zeolite Structures* 2007. http://www.iza-structure.org/databases/.

17. Yaghi, O. M., Li, H., Davis, C., Richardson, D. & Groy, T. L. Synthetic Strategies, Structure Patterns, and Emerging Properties in the Chemistry of Modular Porous Solids. *Acc. Chem. Res.* **31,** 474–484. https://pubs.acs.org/doi/10.1021/ar970151f (Aug. 1998).

18. Yaghi, O. M., O'Keeffe, M., Ockwig, N. W., Chae, H. K., Eddaoudi, M. & Kim, J. Reticular synthesis and the design of new materials. *Nature* **423,** 705–714. http://www.nature.com/articles/nature01650 (June 2003).

19. Farha, O. K., Eryazici, I., Jeong, N. C., Hauser, B. G., Wilmer, C. E., Sarjeant, A. A., Snurr, R. Q., Nguyen, S. T., Yazaydın, A. Ö. & Hupp, J. T. Metal-Organic Framework Materials with Ultrahigh Surface Areas: Is the Sky the Limit? *J. Am. Chem. Soc.* **134,** 15016–15021. http://pubs.acs.org/doi/10.1021/ja3055639 (Sept. 2012).

20. Furukawa, H., Cordova, K. E., O'Keeffe, M. & Yaghi, O. M. The chemistry and applications of metal-organic frameworks. *Science* **341,** 1230444 (2013).

21. Uribe-Romo, F. J., Furukawa, H., O'Keeffe, M., Yaghi, O. M., Klöck, C. & Hunt, J. R. A Crystalline Imine-Linked 3-D Porous Covalent Organic Framework. *J. Am. Chem. Soc.* **131,** 4570–4571. https://pubs.acs.org/doi/10.1021/ja8096256 (Apr. 2009).

22. Nishihara, H. & Kyotani, T. in *Nov. Carbon Adsorbents* 295–322 (Elsevier, 2012). https://linkinghub.elsevier.com/retrieve/pii/B9780080977447000107.

23. Moghadam, P. Z., Li, A., Wiggin, S. B., Tao, A., Maloney, A. G. P., Wood, P. A., Ward, S. C. & Fairen-Jimenez, D. Development of a Cambridge Structural Database Subset: A Collection of Metal-Organic Frameworks for Past, Present, and Future. *Chem. Mater.* **29,** 2618–2625. http://pubs.acs.org/doi/abs/10.1021/acs.chemmater.7b00441 (Apr. 2017).

24. Wilmer, C. E., Leaf, M., Lee, C. Y., Farha, O. K., Hauser, B. G., Hupp, J. T. & Snurr, R. Q. Large-scale screening of hypothetical metal-organic frameworks. *Nat. Chem.* **4,** 83–89. http://www.nature.com/articles/nchem.1192 (Feb. 2012).

25. Witman, M., Ling, S., Anderson, S., Tong, L., Stylianou, K. C., Slater, B., Smit, B. & Haranczyk, M. In silico design and screening of hypothetical MOF-74 analogs and their experimental synthesis. *Chem. Sci.* **7,** 6263–6272. http://dx.doi.org/10.1039/C6SC01477A%20http://pubs.rsc.org/en/Content/ArticleLanding/2016/SC/C6SC01477A%7B%5C%%7D5Cnhttp://xlink.rsc.org/?DOI=C6SC01477A%20http://xlink.rsc.org/?DOI=C6SC01477A (2016).

26. Yazaydın, A. Ö., Snurr, R. Q., Park, T.-H., Koh, K., Liu, J., LeVan, M. D., Benin, A. I., Jakubczak, P., Lanuza, M., Galloway, D. B., Low, J. J. & Willis, R. R. Screening of Metal-Organic Frameworks for Carbon Dioxide Capture from Flue Gas Using a Combined Experimental and Modeling Approach. *J. Am. Chem. Soc.* **131,** 18198–18199 (2009).

27. McDonald, T. M., Mason, J. A., Kong, X., Bloch, E. D., Gygi, D., Dani, A., Crocellà, V., Giordanino, F., Odoh, S. O., Drisdell, W. S., Vlaisavljevich, B., Dzubak, A. L., Poloni, R., Schnell, S. K., Planas, N., Lee, K., Pascal, T., Wan, L. F., Prendergast, D., Neaton, J. B., Smit, B., Kortright, J. B., Gagliardi, L., Bordiga, S., Reimer, J. a. & Long, J. R. Cooperative insertion of CO2 in diamine-appended metal-organic frameworks. *Nature.* http://www.nature.com/doifinder/10.1038/nature14327 (2015).

28. Vlaisavljevich, B., Odoh, S. O., Schnell, S. K., Dzubak, A. L., Lee, K., Planas, N., Neaton, J. B., Gagliardi, L. & Smit, B. CO2 induced phase transitions in diamine-appended metal-organic frameworks. *Chem. Sci.* **6,** 5177–5185. http://pubs.rsc.org/en/Content/ArticleLanding/2015/SC/C5SC01828E%20http://xlink.rsc.org/?DOI=C5SC01828E (2015).

29. Mercado, R., Fu, R.-S., Yakutovich, A. V., Talirz, L., Haranczyk, M. & Smit, B. In Silico Design of 2D and 3D Covalent Organic Frameworks for Methane Storage Applications. *Chem. Mater.* **30,** 5069–5086. http://pubs.acs.org/doi/10.1021/acs.chemmater.8b01425 (Aug. 2018).

30. Thornton, A. W., Simon, C. M., Kim, J., Kwon, O., Deeg, K. S., Konstas, K., Pas, S. J., Hill, M. R., Winkler, D. A., Haranczyk, M. & Smit, B. Materials Genome in Action: Identifying the Performance Limits of Physical Hydrogen Storage. *Chem. Mater.* **29,** 2844–2854. http://pubs.acs.org/doi/10.1021/acs.chemmater.6b04933 (Apr. 2017).

31. Conway, B. E. *Electrochemical Supercapacitors: Scientific Fundamentals and Technological Applications* http://link.springer.com/10.1007/978-1-4757-3058-6 (Springer US, Boston, MA, 2013).

32. Salunkhe, R. R., Kaneti, Y. V., Kim, J., Kim, J. H. & Yamauchi, Y. Nanoarchitectures for Metal-Organic Framework-Derived Nanoporous Carbons toward Supercapacitor Applications. *Acc. Chem. Res.* **49,** 2796–2806. http://pubs.acs.org/doi/abs/10.1021/acs.accounts.6b00460%20http://pubs.acs.org/doi/10.1021/acs.accounts.6b00460 (Dec. 2016).

33. Sheberla, D., Bachman, J. C., Elias, J. S., Sun, C.-J., Shao-Horn, Y. & Dincă, M. Conductive MOF electrodes for stable supercapacitors with high areal capacitance. *Nat. Mater.* **1,** 1–6. http://www.nature.com/doifinder/10.1038/nmat4766 (2016).

34. Rappe, A. K., Casewit, C. J., Colwell, K. S., Goddard, W. A. & Skiff, W. M. UFF, a full periodic table force field for molecular mechanics and molecular dynamics simulations. *J. Am. Chem. Soc.* **114,** 10024–10035. http://pubs.acs.org/doi/abs/10.1021/ja00051a040 (Dec. 1992).

35. Allured, V. S., Kelly, C. M. & Landis, C. R. SHAPES empirical force field: new treatment of angular potentials and its application to square-planar transition-metal complexes. *J. Am. Chem. Soc.* **113,** 1–12. http://pubs.acs.org/doi/abs/10.1021/ja00001a001 (Jan. 1991).

36. Lennard-Jones, J. E. On the Determination of Molecular Fields. II. From the Equation of State of a Gas. *Proc. R. Soc. A Math. Phys. Eng. Sci.* **106,** 463–477. http://rspa.royalsocietypublishing.org/cgi/doi/10.1098/rspa.1924.0082 (Oct. 1924).

37. Frenkel, D. & Smit, B. *Understanding Molecular Simulation: From Algorithms to Applications* 2nd ed. (eds Frenkel, D., Klein, M., Parrinello, M. & Smit, B.) 280–282 (Academic Press: San Diego, 2001).

38. Liu, Y. M. & Smit, B. Predicting Product Distribution of Propene Dimerization in Nanoporous Materials. *ACS Catal.* **7,** 3940–3948. http://pubs.acs.org/doi/abs/10.1021/acscatal.7b00712 (June 2017).

39. Alaerts, L., Séguin, E., Poelman, H., Thibault-Starzyk, F., Jacobs, P. A. & De Vos, D. E. Probing the Lewis Acidity and Catalytic Activity of the Metal–Organic Framework [Cu3(BTC)2](BTC= Benzene-1, 3, 5-tricarboxylate). *Chem. - Eur. J.* **12,** 7353–7363 (2006).

40. Lee, J., Farha, O. K., Roberts, J., Scheidt, K. A., Nguyen, S. T. & Hupp, J. T. Metal–organic framework materials as catalysts. *Chem. Soc. Rev.* **38,** 1450–1459 (2009).

41. Dang, G. H., Lam, H. Q., Nguyen, A. T., Le, D. T., Truong, T. & Phan, N. T. S. Synthesis of indolizines through aldehyde–amine–alkyne couplings using metal-organic framework Cu-MOF-74 as an efficient heterogeneous catalyst. *J. Catal.* **337,** 167–176 (2016).

42. O'Connor, C. T. & Kojima, M. Alkene oligomerization. *Catal. Today* **6,** 329–349 (1990).

43. Wilshier, K. G., Smart, P., Western, R., Mole, T. & Behrsing, T. Oligomerization of propene over H-ZSM-5 zeolite. *Appl. Catal.* **31,** 339–359 (1987).

44. Quann, R. J., Green, L. A., Tabak, S. A. & Krambeck, F. J. Chemistry of olefin oligomerization over ZSM-5 catalyst. *Ind. Eng. Chem. Res.* **27,** 565–570 (1988).

45. Mlinar, A. N., Ho, O. C., Bong, G. G. & Bell, A. T. The Effect of Noncatalytic Cations on the Activity and Selectivity of Nickel-Exchanged X Zeolites for Propene Oligomerization. *ChemCatChem* **5,** 3139–3147 (2013).

46. Mlinar, A. N., Keitz, B. K., Gygi, D., Bloch, E. D., Long, J. R. & Bell, A. T. Selective Propene Oligomerization with Nickel (II)-Based Metal–Organic Frameworks. *ACS Catal.* **4,** 717–721 (2014).

47. Smit, B. & Maesen, T. L. M. Towards a molecular understanding of shape selectivity. *Nature* **451,** 671–678 (2008).

48. Smit, B. & Maesen, T. L. M. Molecular simulations of zeolites: adsorption, diffusion, and shape selectivity. *Chem. Rev.* **108,** 4125–4184 (2008).

49. Earl, D. J. & Deem, M. W. Toward a Database of Hypothetical Zeolite Structures. *Ind. Eng. Chem. Res.* **45,** 5449–5454. https://pubs.acs.org/doi/10.1021/ie0510728 (Aug. 2006).

50. Böhme, U., Barth, B., Paula, C., Kuhnt, A., Schwieger, W., Mundstock, A., Caro, J. & Hartmann, M. Ethene/ethane and propene/propane separation via the olefin and paraffin selective metal–organic framework adsorbents CPO-27 and ZIF-8. *Langmuir* **29,** 8592–8600 (2013).

51. Wick, C. D., Martin, M. G. & Siepmann, J. I. Transferable potentials for phase equilibria. 4. United-atom description of linear and branched alkenes and alkylbenzenes. *J. Phys. Chem. B* **104,** 8008–8016 (2000).

52. Mayo, S. L., Olafson, B. D. & Goddard III, W. A. DREIDING: a generic force field for molecular simulations. *J. Phys. Chem.* **94,** 8897–8909 (1990).

53. Rappé, A. K., Casewit, C. J., Colwell, K. S., Goddard III, W. A. & Skiff, W. M. UFF, a full periodic table force field for molecular mechanics and molecular dynamics simulations. *J. Am. Chem. Soc.* **114,** 10024–10035 (1992).

54. Campaná, C., Mussard, B. & Woo, T. K. Electrostatic potential derived atomic charges for periodic systems using a modified error functional. *J. Chem. Theory Comput.* **5,** 2866–2878 (2009).

55. Mercado, R., Vlaisavljevich, B., Lin, L.-C., Lee, K., Lee, Y., Mason, J. A., Xiao, D. J., Gonzalez, M. I., Kapelewski, M. T., Neaton, J. B. & Smit, B. Force Field Development from Periodic Density Functional Theory Calculations for Gas Separation Applications Using Metal–Organic Frameworks. *J. Phys. Chem. C* **120,** 12590–12604 (2016).

56. Liu, B., Smit, B., Rey, F., Valencia, S. & Calero, S. A new united atom force field for adsorption of alkenes in zeolites. *J. Phys. Chem. C* **112,** 2492–2498 (2008).

57. Weitz, S. L. & Potoff, J. J. Effect of quadrupole moment on the phase behavior of binary mixtures containing ethene. *Fluid Phase Equilib.* **234,** 144–150 (2005).

58. Wang, S., Yang, Q. & Zhong, C. Adsorption and separation of binary mixtures in a metal-organic framework Cu-BTC: A computational study. *Sep. Purif. Technol.* **60,** 30–35 (2008).

59. Evans, M. G. & Polanyi, M. Further considerations on the thermodynamics of chemical equilibria and reaction rates. *Trans. Faraday Soc.* **32,** 1333–1360 (1936).

60. Dubbeldam, D., Calero, S., Ellis, D. E. & Snurr, R. Q. RASPA: molecular simulation software for adsorption and diffusion in flexible nanoporous materials. *Mol. Simul.* **42,** 81–101 (2016).

61. Childs, H., Brugger, E., Whitlock, B., Meredith, J., Ahern, S., Pugmire, D., Biagas, K., Miller, M., Harrison, C., Weber, G., Krishnan, H., Fogal, T., Sanderson, A., Garth, C., Bethel, E., Camp, D., Rubel, O., Durant, M., Favre, J. & Navratil, P. in *High Perform. Vis. Extrem. Sci. Insight* 357–372 (Chapman and Hall/CRC, Nov. 2012).

62. Rosi, N. L., Kim, J., Eddaoudi, M., Chen, B., O'Keeffe, M. & Yaghi, O. M. Rod Packings and Metal-Organic Frameworks Constructed from Rod-Shaped Secondary Building Units. *J. Am. Chem. Soc.* **127,** 1504–1518. http://pubs.acs.org/doi/abs/10.1021/ja045123o (Feb. 2005).

63. McDonald, T. M., Lee, W. R., Mason, J. A., Wiers, B. M., Hong, C. S. & Long, J. R. Capture of Carbon Dioxide from Air and Flue Gas in the Alkylamine-Appended Metal-Organic Framework mmen-Mg 2 (dobpdc). *J. Am. Chem. Soc.* **134,** 7056–7065. http://pubs.acs.org/doi/abs/10.1021/ja300034j (Apr. 2012).

64. Witman, M., Ling, S., Gladysiak, A., Stylianou, K. C., Smit, B., Slater, B. & Haranczyk, M. Rational Design of a Low-Cost, High-Performance Metal-Organic Framework for Hydrogen Storage and Carbon Capture. *J. Phys. Chem. C* **121,** 1171–1181 (Jan. 2017).

65. Yaghi, O. M., Li, H. & Groy, T. L. Construction of porous solids from hydrogen-bonded metal complexes of 1, 3, 5-benzenetricarboxylic acid. *J. Am. Chem. Soc.* **118,** 9096–9101 (1996).

66. Ongari, D., Liu, Y. M. & Smit, B. Can MOFs Be Used for THC Breathalyzers? *Submitted* (2019).

67. Hall, W. & Lynskey, M. Evaluating the public health impacts of legalizing recreational cannabis use in the United States. *Addiction* **111,** 1764–1773. arXiv: arXiv:1011.1669v3 (2016).

68. Hasin, D. S. US Epidemiology of Cannabis Use and Associated Problems. *Neuropsychopharmacology* **43,** 195–212. arXiv: 1304.6299. http://dx.doi.org/10.1038/npp.2017.198 (2018).

69. Rogeberg, O. & Elvik, R. The effects of cannabis intoxication on motor vehicle collision revisited and revised. *Addiction* **111,** 1348–1359. http://doi.wiley.com/10.1111/add.13347 (Aug. 2016).

70. Ramaekers, J., Berghaus, G., van Laar, M. & Drummer, O. Dose related risk of motor vehicle crashes after cannabis use. *Drug Alcohol Depend.* **73,** 109–119. https://linkinghub.elsevier.com/retrieve/pii/S0376871603002849 (Feb. 2004).

71. Hartman, R. L. & Huestis, M. A. Cannabis effects on driving skills. *Clin. Chem.* **59,** 478–492 (2013).

72. Couper, F. J. & Logan, B. K. *Drugs and human performance fact sheets.* tech. rep. (Washington State Patrol Forensic Laboratory Services Bureau, Seattle, WA, 2014). https://rosap.ntl.bts.gov/view/dot/2003.

73. Himes, S. K., Scheidweiler, K. B., Beck, O., Gorelick, D. A., Desrosiers, N. A. & Huestis, M. A. Cannabinoids in Exhaled Breath following Controlled Administration of Smoked Cannabis. *Clin. Chem.* **59,** 1780–1789. http://www.clinchem.org/cgi/doi/10.1373/clinchem.2013.207407 (Dec. 2013).

74. Marsot, A., Audebert, C., Attolini, L., Lacarelle, B., Micallef, J. & Blin, O. Comparison of cannabinoid concentrations in plasma, oral fluid and urine in occasional cannabis smokers after smoking cannabis cigarette. *J. Pharm. Pharm. Sci.* **19,** 411–422 (2016).

75. Kretschmer, C. B. & Wiebe, R. Liquid-Vapor Equilibrium of Ethanol–Toluene Solutions. *J. Am. Chem. Soc.* **71,** 1793–1797. http://pubs.acs.org/doi/abs/10.1021/ja01173a076 (May 1949).

76. Scatchard, G. & Raymond, C. L. Vapor–Liquid Equilibrium. II. Chloroform–Ethanol Mixtures at 35, 45 and 55°. *J. Am. Chem. Soc.* **60,** 1278–1287. http://pubs.acs.org/doi/abs/10.1021/ja01273a002 (June 1938).

77. Lovestead, T. M. & Bruno, T. J. Determination of cannabinoid vapor pressures to aid in vapor phase detection of intoxication. *Forensic Chem.* **5,** 79–85 (2017).

78. Beck, O., Sandqvist, S., Dubbelboer, I. & Franck, J. Detection of Δ9 -Tetrahydrocannabinol in Exhaled Breath Collected from Cannabis Users. **35,** 541–544. http://jat.oxfordjournals.org/content/35/8/541.full.pdf (2011).

79. Gordon, M. J., Jones, L. C. & Lynn, M. S. *Devices for target substance detection and measurement* 2017. https://patentimages.storage.googleapis.com/91/63/24/09f87f7df6b382/US9709581.pdf.

80. Chong, X., Kim, K. J., Ohodnicki, P. R., Li, E., Chang, C. H. & Wang, A. X. Ultrashort Near-Infrared Fiber-Optic Sensors for Carbon Dioxide Detection. *IEEE Sens. J.* **15,** 5327–5332 (2015).

81. Chong, X., Kim, K. J., Li, E., Zhang, Y., Ohodnicki, P. R., Chang, C. H. & Wang, A. X. Near-infrared absorption gas sensing with metal–organic framework on optical fibers. *Sensors Actuators, B Chem.* **232,** 43–51. http://dx.doi.org/10.1016/j.snb.2016.03.135 (2016).

82. Kim, K.-J., Lu, P., Culp, J. T. & Ohodnicki, P. R. Metal–Organic Framework Thin Film Coated Optical Fiber Sensors: A Novel Waveguide-Based Chemical Sensing Platform. *ACS Sensors* **3,** 386–394. http://pubs.acs.org/doi/10.1021/acssensors.7b00808 (Feb. 2018).

83. Dronova, M., Smolianitski, E. & Lev, O. Electrooxidation of New Synthetic Cannabinoids: Voltammetric Determination of Drugs in Seized Street Samples and Artificial Saliva. *Anal. Chem.* **88,** 4487–4494 (2016).

84. Zhou, H.-C., Long, J. R. & Yaghi, O. M. Introduction to Metal-Organic Frameworks. *Chem. Rev.* **112,** 673–674. http://pubs.acs.org/doi/10.1021/cr300014x (Feb. 2012).

85. Kitagawa, S., Kitaura, R. & Noro, S.-i. Functional Porous Coordination Polymers. *Angew. Chemie Int. Ed.* **43,** 2334–2375. http://doi.wiley.com/10.1002/anie.200300610 (Apr. 2004).

86. Eddaoudi, M. Systematic Design of Pore Size and Functionality in Isoreticular MOFs and Their Application in Methane Storage. *Science* **295,** 469–472. http://www.sciencemag.org/cgi/doi/10.1126/science.1067208 (Jan. 2002).

87. Bobbitt, N. S., Mendonca, M. L., Howarth, A. J., Islamoglu, T., Hupp, J. T., Farha, O. K. & Snurr, R. Q. Metal–organic frameworks for the removal of toxic industrial chemicals and chemical warfare agents. *Chem. Soc. Rev.* **46,** 3357–3385. http://xlink.rsc.org/?DOI=C7CS00108H (2017).

88. Matito-Martos, I., Moghadam, P. Z., Li, A., Colombo, V., Navarro, J. A., Calero, S. & Fairen-Jimenez, D. Discovery of an Optimal Porous Crystalline Material for the Capture of Chemical Warfare Agents. *Chem. Mater.* **30,** 4571–4579 (2018).

89. Chung, Y. G., Camp, J., Haranczyk, M., Sikora, B. J., Bury, W., Krungleviciute, V., Yildirim, T., Farha, O. K., Sholl, D. S. & Snurr, R. Q. Computation-ready, experimental metal-organic frameworks: A tool to enable high-throughput screening of nanoporous crystals. *Chem. Mater.* **26,** 6185–6192 (2014).

90. Willems, T. F., Rycroft, C. H., Kazi, M., Meza, J. C. & Haranczyk, M. Algorithms and tools for high-throughput geometry-based analysis of crystalline porous materials. *Microporous Mesoporous Mater.* **149,** 134–141. https://linkinghub.elsevier.com/retrieve/pii/S1387181111003738 (Feb. 2012).

91. VandeVondele, J., Krack, M., Mohamed, F., Parrinello, M., Chassaing, T. & Hutter, J. Quickstep: Fast and accurate density functional calculations using a mixed Gaussian and plane waves approach. *Comput. Phys. Commun.* **167,** 103–128. http://linkinghub.elsevier.com/retrieve/pii/S0010465505000615 (Apr. 2005).

92. Perdew, J. P., Burke, K. & Ernzerhof, M. Generalized Gradient Approximation Made Simple. *Phys. Rev. Lett.* **77,** 3865–3868. https://link.aps.org/doi/10.1103/PhysRevLett.77.3865 (Oct. 1996).

93. Goedecker, S., Teter, M. & Hutter, J. Separable dual-space Gaussian pseudopotentials. *Phys. Rev. B* **54,** 1703–1710. https://link.aps.org/doi/10.1103/PhysRevB.54.1703 (July 1996).

94. VandeVondele, J. & Hutter, J. Gaussian basis sets for accurate calculations on molecular systems in gas and condensed phases. *J. Chem. Phys.* **127,** 114105. http://aip.scitation.org/doi/10.1063/1.2770708 (Sept. 2007).

95. Manz, T. A. & Limas, N. G. Introducing DDEC6 atomic population analysis: part 1. Charge partitioning theory and methodology. *RSC Adv.* **6,** 47771–47801. http://xlink.rsc.org/?DOI=C6RA04656H (2016).

96. Martin, M. G. & Siepmann, J. I. Transferable Potentials for Phase Equilibria. 1. United-Atom Description of n-Alkanes. *J. Phys. Chem. B* **103,** 5370–5379. https://pubs.acs.org/doi/abs/10.1021/jp972543%7B%5C%%7D2B (2002).

97. Siepmann, J. I. & Frenkel, D. Configurational bias Monte Carlo: a new sampling scheme for flexible chains. *Mol. Phys.* **75,** 59–70. http://www.tandfonline.com/doi/abs/10.1080/00268979200100061 (Jan. 1992).

98. Dubbeldam, D., Calero, S., Ellis, D. E. & Snurr, R. Q. RASPA: molecular simulation software for adsorption and diffusion in flexible nanoporous materials. *Mol. Simul.* **42,** 81–101. http://www.tandfonline.com/doi/full/10.1080/08927022.2015.1010082 (Jan. 2016).

99. Dzubak, A. L., Lin, L.-C., Kim, J., Swisher, J. A., Poloni, R., Maximoff, S. N., Smit, B. & Gagliardi, L. Ab initio carbon capture in open-site metal-organic frameworks. *Nat. Chem.* **4,** 810–816. http://www.nature.com/doifinder/10.1038/nchem.1432 (Aug. 2012).

100. Geier, S. J., Mason, J. A., Bloch, E. D., Queen, W. L., Hudson, M. R., Brown, C. M. & Long, J. R. Selective adsorption of ethylene over ethane and propylene over propane in the metal-organic frameworks M2(dobdc) (M = Mg, Mn, Fe, Co, Ni, Zn). *Chem. Sci.* **4,** 2054. http://xlink.rsc.org/?DOI=c3sc00032j (2013).

101. Kapelewski, M. T., Geier, S. J., Hudson, M. R., Stück, D., Mason, J. A., Nelson, J. N., Xiao, D. J., Hulvey, Z., Gilmour, E., FitzGerald, S. A., Head-Gordon, M., Brown, C. M. & Long, J. R. M2(m-dobdc) (M = Mg, Mn, Fe, Co, Ni) Metal-Organic Frameworks Exhibiting Increased Charge Density and Enhanced H 2 Binding at the Open Metal Sites. *J. Am. Chem. Soc.* **136,** 12119–12129. http://pubs.acs.org/doi/10.1021/ja506230r (Aug. 2014).

102. Moghadam, P. Z., Fairen-Jimenez, D. & Snurr, R. Q. Efficient identification of hydrophobic MOFs: Application in the capture of toxic industrial chemicals. *J. Mater. Chem. A* **4,** 529–536 (2015).

103. Ongari, D., Boyd, P. G., Kadioglu, O., Mace, A. K., Keskin, S. & Smit, B. Evaluating Charge Equilibration Methods To Generate Electrostatic Fields in Nanoporous Materials. *J. Chem. Theory Comput.* **15,** 382–401. http://pubs.acs.org/doi/10.1021/acs.jctc.8b00669 (Jan. 2019).

104. Jorgensen, W. L., Chandrasekhar, J., Madura, J. D., Impey, R. W. & Klein, M. L. Comparison of simple potential functions for simulating liquid water. *J. Chem. Phys.* **79,** 926–935. http://aip.scitation.org/doi/10.1063/1.445869 (July 1983).

105. Mercado, R., Vlaisavljevich, B., Lin, L.-C., Lee, K., Lee, Y., Mason, J. A., Xiao, D. J., Gonzalez, M. I., Kapelewski, M. T., Neaton, J. B. & Smit, B. Force Field Development from Periodic Density Functional Theory Calculations for Gas Separation Applications Using Metal–Organic Frameworks. *J. Phys. Chem. C* **120,** 12590–12604. http://pubs.acs.org/doi/abs/10.1021/acs.jpcc.6b03393%20http://pubs.acs.org/doi/10.1021/acs.jpcc.6b03393 (June 2016).

106. Ongari, D., Boyd, P. G., Barthel, S., Witman, M., Haranczyk, M. & Smit, B. Accurate characterization of the pore volume in microporous crystalline materials. *Langmuir* (2017).

107. Wilmer, C. E., Farha, O. K., Bae, Y.-S., Hupp, J. T. & Snurr, R. Q. Structure–property relationships of porous materials for carbon dioxide separation and capture. *Energy Environ. Sci.* **5,** 9849. http://xlink.rsc.org/?DOI=c2ee23201d (2012).

108. Li, W.-H., Ding, K., Tian, H.-R., Yao, M.-S., Nath, B., Deng, W.-H., Wang, Y. & Xu, G. Conductive Metal-Organic Framework Nanowire Array Electrodes for High-Performance Solid-State Supercapacitors. *Adv. Funct. Mater.* **27,** 1702067. http://doi.wiley.com/10.1002/adfm.201702067 (July 2017).

109. Liu, Y. M. *michelleliu/zeoplusplus: "Modified extended output" version* 2019. https://zenodo.org/record/3247355.

110. Liu, Y. M. *michelleliu/geometric-overlap: Geometric Overlap method for accessibility of porous material to a nonspherical probe* 2019. https://zenodo.org/record/3247347.

111. Garrett, E. R. & Hunt, C. Physicochemical Properties, Solubility, and Protein Binding of Δ9-Tetrahydrocannabinol. *J. Pharm. Sci.* **63,** 1056–1064. https://linkinghub.elsevier.com/retrieve/pii/S0022354915417356 (July 1974).

112. *HSDB: Δ9-Tetrahydrocannabinol CASRN: 1972-08-3* Bethesda, MD, 2018. https://toxnet.nlm.nih.gov/cgi-bin/sis/search/r?dbs+hsdb:@term+@rn+@rel+1972-08-3 (2019).

113. Xu, J., Blaakmeer, E. S. M., Lipton, A. S., McDonald, T. M., Liu, Y. M., Smit, B., Long, J. R., Kentgens, A. P. M. & Reimer, J. A. Uncovering the Local Magnesium Environment in the Metal-Organic Framework Mg2(dobpdc) Using 25Mg NMR Spectroscopy. *J. Phys. Chem. C* **121,** 19938–19945. http://pubs.acs.org/doi/abs/10.1021/acs.jpcc.7b07809 (2017).

114. Xu, J., Liu, Y. M., Lipton, A. S., Ye, J., Milner, P. J., McDonald, T. M., Siegelman, R. L., Forse, A. C., Smit, B., Long, J. R. & Reimer, J. A. Amine Dynamics in Diamine-Appended Mg2(dobpdc) Metal-Organic Frameworks. *Submitted* (2018).

115. Cole, S. *2018 fourth warmest year in continued warming trend, according to NASA, NOAA* 2019. https://climate.nasa.gov/news/2841/2018-fourth-warmest-year-in-continued-warming-trend-according-to-nasa-noaa/.

116. Smit, B., Reimer, J. A., Oldenburg, C. M. & Bourg, I. C. *Introduction to Carbon Capture and Sequestration* (World Scientific, 2014).

117. Ciferno, J. P., Fout, T. E., Jones, A. P., Murphy, J. T., *et al.* Capturing carbon from existing coal-fired power plants. *Chem. Eng. Prog.* **105,** 33 (2009).

118. *Where Greenhouse Gases Come From - Energy Explained, Your Guide To Understanding Energy - Energy Information Administration* 2018. https://www.eia.gov/energyexplained/index.php?page=environment%7B%5C_%7Dwhere%7B%5C_%7Dghg%7B%5C_%7Dcome%7B%5C_%7Dfrom (2019).

119. Sumida, K., Rogow, D. L., Mason, J. A., McDonald, T. M., Bloch, E. D., Herm, Z. R., Bae, T.-H. & Long, J. R. Carbon dioxide capture in metal–organic frameworks. *Chem. Rev.* **112,** 724–781 (2011).

120. Huck, J. M., Lin, L.-C., Berger, A. H., Shahrak, M. N., Martin, R. L., Bhown, A. S., Haranczyk, M., Reuter, K. & Smit, B. Evaluating different classes of porous materials for carbon capture. *Energy Environ. Sci.* **7,** 4132–4146 (2014).

121. Yaghi, O. M., O'Keeffe, M., Ockwig, N. W., Chae, H. K., Eddaoudi, M. & Kim, J. Reticular synthesis and the design of new materials. *Nature* **423,** 705–714 (2003).

122. McDonald, T. M., Lee, W. R., Mason, J. A., Wiers, B. M., Hong, C. S. & Long, J. R. Capture of Carbon Dioxide from Air and Flue Gas in the Alkylamine-Appended Metal-Organic Framework mmen-Mg2(dobpdc). *J. Am. Chem. Soc.* **134.** PMID: 22475173, 7056–7065 (2012).

123. McDonald, T. M., Mason, J. A., Kong, X., Bloch, E. D., Gygi, D., Dani, A., Crocellà, V., Giordanino, F., Odoh, S. O., Drisdell, W. S., *et al.* Cooperative insertion of CO2 in diamine-appended metal-organic frameworks. *Nature* **519,** 303–308 (2015).

124. Van Duin, A. C., Dasgupta, S., Lorant, F. & Goddard, W. A. ReaxFF: A reactive force field for hydrocarbons. *J. Phys. Chem. A* **105,** 9396–9409. arXiv: arXiv:1011.1669v3 (2001).

125. Huang, L., Joshi, K., Duin, A., Bandosz, T. & Gubbins, K. ReaxFF molecular dynamics simulation of thermal stability of a Cu3(BTC)2 metal-organic framework. *Phys. Chem. Chem. Phys.* **14** (2012).

126. Brenner, D. W., Shenderova, O. A., Harrison, J. A., Stuart, S. J., Ni, B. & Sinnott, S. B. A second-generation reactive empirical bond order (REBO) potential energy expression for hydrocarbons. *J. Phys. Condens. Matter* **14,** 783–802. http://stacks.iop.org/0953-8984/14/i=4/a=312?key=crossref.563ba867ec801ce55fc736b3f8968942 (Feb. 2002).

127. Stuart, S. J., Tutein, A. B. & Harrison, J. A. A reactive potential for hydrocarbons with intermolecular interactions. *J. Chem. Phys.* **112,** 6472–6486. http://aip.scitation.org/doi/10.1063/1.481208 (Apr. 2000).

128. Rappe, A. K. & Goddard III, W. A. Charge equilibration for molecular dynamics simulations. *J. Phys. Chem.* **95,** 3358–3363 (1991).

129. Jaramillo-Botero, A., Naserifar, S. & Goddard III, W. A. General multiobjective force field optimization framework, with application to reactive force fields for silicon carbide. *J. Chem. Theory Comput.* **10,** 1426–1439 (2014).

130. Eyring, H. The Activated Complex in Chemical Reactions. *J. Chem. Phys.* **3,** 107–115. http://aip.scitation.org/doi/10.1063/1.1749604 (Feb. 1935).

131. Evans, M. G. & Polanyi, M. Some applications of the transition state method to the calculation of reaction velocities, especially in solution. *Trans. Faraday Soc.* **31,** 875. http://xlink.rsc.org/?DOI=tf9353100875 (1935).

132. Drisdell, W. S., Poloni, R., McDonald, T. M., Pascal, T. A., Wan, L. F., Pemmaraju, C. D., Vlaisavljevich, B., Odoh, S. O., Neaton, J. B., Long, J. R., Prendergast, D. & Kortright, J. B. Probing the mechanism of CO2 capture in diamine-appended metal-organic frameworks using measured and simulated X-ray spectroscopy. *Phys. Chem. Chem. Phys.* **17,** 21448–21457. http://xlink.rsc.org/?DOI=C5CP02951A (2015).

133. Jaramillo-Botero, A., Naserifar, S. & Goddard, W. A. General Multiobjective Force Field Optimization Framework, with Application to Reactive Force Fields for Silicon Carbide. *J. Chem. Theory Comput.* **10,** 1426–1439. http://pubs.acs.org/doi/10.1021/ct5001044 (Apr. 2014).

134. Liu, Y. M., Merlet, C. & Smit, B. Mechanisms of Charge Storage in Zeolite-Templated Carbon Supercapacitors. *Submitted* (2019).

135. Ragone, D. V. *Review of Battery Systems for Electrically Powered Vehicles* in (Feb. 1968). http://papers.sae.org/680453/.

136. Christen, T. & Carlen, M. W. Theory of Ragone plots. *J. Power Sources* **91,** 210–216. http://linkinghub.elsevier.com/retrieve/pii/S0378775300004742 (Dec. 2000).

137. *General Description of Aluminum Electrolytic Capacitors* tech. rep. (Nichicon Corporation, 2014), 1–27.

138. Helmholtz, H. Ueber einige Gesetze der Vertheilung elektrischer Ströme in körperlichen Leitern mit Anwendung auf die thierisch-elektrischen Versuche. *Ann. der Phys. und Chemie* **165,** 211–233. http://doi.wiley.com/10.1002/andp.18531650603 (1853).

139. Helmholtz, H. Studien über electrische Grenzschichten. *Ann. der Phys. und Chemie* **243,** 337–382. http://doi.wiley.com/10.1002/andp.18792430702 (1879).

140. Gouy, M. Sur la constitution de la charge électrique à la surface d'un électrolyte. *J. Phys. Théorique Appliquée* **9,** 457–468. http://www.edpsciences.org/10.1051/jphystap:019100090045700 (1910).

141. Chapman, D. L. LI. A contribution to the theory of electrocapillarity. *London, Edinburgh, Dublin Philos. Mag. J. Sci.* **25,** 475–481. https://www.tandfonline.com/doi/full/10.1080/14786440408634187 (Apr. 1913).

142. Stern, O. Zur theorie der elektrolytischen doppelschicht. *Zeitschrift für Elektrochemie Angew. Phys. Chemie* (1924).

143. Chmiola, J. Anomalous Increase in Carbon Capacitance at Pore Sizes Less Than 1 Nanometer. *Science* **313,** 1760–1763. arXiv: caps18. http://www.sciencemag.org/cgi/doi/10.1126/science.1132195 (Sept. 2006).

144. Raymundo-Piñero, E., Kierzek, K., Machnikowski, J. & Béguin, F. Relationship between the nanoporous texture of activated carbons and their capacitance properties in different electrolytes. *Carbon* **44,** 2498–2507. http://www.sciencedirect.com/science/article/pii/S0008622306002880 (2006).

145. Huang, J., Sumpter, B. G. & Meunier, V. A Universal Model for Nanoporous Carbon Supercapacitors Applicable to Diverse Pore Regimes, Carbon Materials, and Electrolytes. *Chem. - A Eur. J.* **14,** 6614–6626. http://doi.wiley.com/10.1002/chem.200800639 (July 2008).

146. Kondrat, S., Georgi, N., Fedorov, M. V. & Kornyshev, A. A. A superionic state in nanoporous double-layer capacitors: insights from Monte Carlo simulations. *Phys. Chem. Chem. Phys.* **13,** 11359–11366. http://www.ncbi.nlm.nih.gov/pubmed/21566824 (2011).

147. Merlet, C., Péan, C., Rotenberg, B., Madden, P. A., Daffos, B., Taberna, P.-L., Simon, P. & Salanne, M. Highly confined ions store charge more efficiently in supercapacitors. *Nat. Commun.* **4,** 2701. http://www.nature.com/articles/ncomms3701 (Dec. 2013).

148. Feng, G., Li, S., Presser, V. & Cummings, P. T. Molecular Insights into Carbon Supercapacitors Based on Room-Temperature Ionic Liquids. *J. Phys. Chem. Lett.* **4,** 3367–3376. http://dx.doi.org/10.1021/jz4014163 (2013).

149. Kondrat, S., Wu, P., Qiao, R. & Kornyshev, A. A. Accelerating charging dynamics in subnanometre pores. *Nat. Mater.* **13,** 387–393 (2014).

150. Prehal, C., Koczwara, C., Jäckel, N., Schreiber, A., Burian, M., Amenitsch, H., Hartmann, M. A., Presser, V. & Paris, O. Quantification of ion confinement and desolvation in nanoporous carbon supercapacitors with modelling and in situ X-ray scattering. *Nat. Energy* **2,** 16215. http://dx.doi.org/10.1038/nenergy.2016.215 (2017).

151. Gogotsi, Y., Nikitin, A., Ye, H., Zhou, W., Fischer, J. E., Yi, B., Foley, H. C. & Barsoum, M. W. Nanoporous carbide-derived carbon with tunable pore size. *Nat. Mater.* **2,** 591–594. http://www.nature.com/articles/nmat957 (Sept. 2003).

152. Pech, D., Brunet, M., Durou, H., Huang, P., Mochalin, V., Gogotsi, Y., Taberna, P.-L. & Simon, P. Ultrahigh-power micrometre-sized supercapacitors based on onion-like carbon. *Nat. Nanotechnol.* **5,** 651–654. http://www.nature.com/articles/nnano.2010.162 (Sept. 2010).

153. Noked, M., Okashy, S., Zimrin, T. & Aurbach, D. Composite Carbon Nanotube/Carbon Electrodes for Electrical Double-Layer Super Capacitors. *Angew. Chemie Int. Ed.* **51,** 1568–1571. http://doi.wiley.com/10.1002/anie.201104334 (Feb. 2012).

154. Salanne, M., Rotenberg, B., Naoi, K., Kaneko, K., Taberna, P.-L., Grey, C. P., Dunn, B. & Simon, P. Efficient storage mechanisms for building better supercapacitors. *Nat. Energy* **1,** 16070. http://www.nature.com/articles/nenergy201670 (2016).

155. Forse, A. C., Merlet, C., Griffin, J. M. & Grey, C. P. New perspectives on the charging mechanisms of supercapacitors. *J. Am. Chem. Soc.* **138,** 5731–5744 (2016).

156. Nishihara, H., Itoi, H., Kogure, T., Hou, P.-X., Touhara, H., Okino, F. & Kyotani, T. Investigation of the Ion Storage/Transfer Behavior in an Electrical Double-Layer Capacitor by Using Ordered Microporous Carbons as Model Materials. *Chem. - A Eur. J.* **15,** 5355–5363. http://doi.wiley.com/10.1002/chem.200802406 (May 2009).

157. Itoi, H., Nishihara, H., Kogure, T. & Kyotani, T. Three-dimensionally arrayed and mutually connected 1.2-nm nanopores for high-performance electric double layer capacitor. *J. Am. Chem. Soc.* **133,** 1165–1167. arXiv: arXiv:1011.1669v3 (2011).

158. Braun, E., Lee, Y., Moosavi, S. M., Barthel, S., Mercado, R., Baburin, I. A., Proserpio, D. M. & Smit, B. Generating carbon schwarzites via zeolite-templating. *Proc. Natl. Acad. Sci.* **115,** 201805062. arXiv: arXiv:1408.1149. http://www.pnas.org/lookup/doi/10.1073/pnas.1805062115 (2018).

159. Roy, D. & Maroncelli, M. An Improved Four-Site Ionic Liquid Model. *J. Phys. Chem. B* **114,** 12629–12631. http://pubs.acs.org/doi/abs/10.1021/jp108179n (Oct. 2010).

160. Edwards, D. M., Madden, P. A. & McDonald, I. R. A computer simulation study of the dielectric properties of a model of methyl cyanide. *Mol. Phys.* **51,** 1141–1161. http://www.tandfonline.com/doi/abs/10.1080/00268978400100731 (1984).

161. Ryckaert, J.-P., Ciccotti, G. & Berendsen, H. J. Numerical integration of the cartesian equations of motion of a system with constraints: molecular dynamics of n-alkanes. *J. Comput. Phys.* **23,** 327–341. https://linkinghub.elsevier.com/retrieve/pii/0021999177900985 (Mar. 1977).

162. Andersen, H. C. Rattle: A "velocity" version of the shake algorithm for molecular dynamics calculations. *J. Comput. Phys.* **52,** 24–34. https://linkinghub.elsevier.com/retrieve/pii/0021999183900141 (Oct. 1983).

163. Siepmann, J. I. & Sprik, M. Influence of surface topology and electrostatic potential on water/electrode systems. *J. Chem. Phys.* **102,** 511–524. http://link.aip.org/link/?JCP/102/511/1 (1995).

164. Reed, S. K., Lanning, O. J. & Madden, P. A. Electrochemical interface between an ionic liquid and a model metallic electrode. *J. Chem. Phys.* **126** (2007).

165. Merlet, C., Salanne, M., Rotenberg, B. & Madden, P. A. Influence of solvation on the structural and capacitive properties of electrical double layer capacitors. *Electrochim. Acta* **101,** 262–271. arXiv: 1308.5495. https://ac.els-cdn.com/S0013468612020816/1-s2.0-S0013468612020816-main.pdf?%7B%5C_%7Dtid=224a7b46-c410-11e7-9fd9-00000aab0f26%7B%5C&%7Dacdnat=1510096104%7B%5C_%7D4532dc808f9b385a49facdbe6f0f636a (2013).

166. Palmer, J. C., Llobet, A., Yeon, S. H., Fischer, J. E., Shi, Y., Gogotsi, Y. & Gubbins, K. E. Modeling the structural evolution of carbide-derived carbons using quenched molecular dynamics. *Carbon N. Y.* **48,** 1116–1123. http://dx.doi.org/10.1016/j.carbon.2009.11.033 (2010).

167. Humphrey, W., Dalke, A. & Schulten, K. VMD: Visual molecular dynamics. *J. Mol. Graph.* **14,** 33–38. http://linkinghub.elsevier.com/retrieve/pii/0263785596000185 (Feb. 1996).

168. Kohlmeyer, A. & Vermaas, J. *akohlmey/topotools: Release 1.7* 2017. https://doi.org/10.5281/zenodo.545655.

169. Plimpton, S. Fast Parallel Algorithms for Short-Range Molecular Dynamics. *J. Comput. Phys.* **117,** 1–19. http://lammps.sandia.gov%20http://linkinghub.elsevier.com/retrieve/pii/S002199918571039X (Mar. 1995).

170. Martyna, G. J., Klein, M. L. & Tuckerman, M. Nosé–Hoover chains: The canonical ensemble via continuous dynamics. *J. Chem. Phys.* **97,** 2635–2643. http://aip.scitation.org/doi/10.1063/1.463940 (Aug. 1992).

171. Péan, C., Merlet, C., Rotenberg, B., Madden, P. A., Taberna, P.-L., Daffos, B., Salanne, M. & Simon, P. On the dynamics of charging in nanoporous carbon-based supercapacitors. *ACS Nano* **8,** 1576–1583 (2014).

172. Merlet, C., Péan, C., Rotenberg, B., Madden, P. A., Simon, P. & Salanne, M. Simulating Supercapacitors: Can We Model Electrodes As Constant Charge Surfaces? *J. Phys. Chem. Lett.* **4,** 264–268. http://pubs.acs.org/doi/10.1021/jz3019226 (Jan. 2013).

173. Wang, Z., Yang, Y., Olmsted, D. L., Asta, M. & Laird, B. B. Evaluation of the constant potential method in simulating electric double-layer capacitors. *J. Chem. Phys.* **141,** 184102. arXiv: 1408.0839. http://scitation.aip.org/content/aip/journal/jcp/141/18/10.1063/1.4899176 (2014).

174. Liu, Y. M. *michelleliu/ASTrA: Atomistic Supercapacitor Trajectory Analysis* 2019. https://zenodo.org/record/3247357.

175. Péan, C., Daffos, B., Merlet, C., Rotenberg, B., Taberna, P.-L., Simon, P. & Salanne, M. Single Electrode Capacitances of Porous Carbons in Neat Ionic Liquid Electrolyte at 100 C: A Combined Experimental and Modeling Approach. *J. Electrochem. Soc.* **162,** A5091–A5095. http://jes.ecsdl.org/cgi/doi/10.1149/2.0151505jes (Feb. 2015).

176. Wang, Z., Olmsted, D. L., Asta, M. & Laird, B. B. Electric potential calculation in molecular simulation of electric double layer capacitors. *J. Phys. Condens. Matter* **28,** 464006. http://stacks.iop.org/0953-8984/28/i=46/a=464006?key=crossref.c14cf3cb02969254409fa5d946413610 (Nov. 2016).

177. Conway, B., Birss, V. & Wojtowicz, J. The role and utilization of pseudocapacitance for energy storage by supercapacitors. *J. Power Sources* **66,** 1–14. https://ac.els-cdn.com/S0378775396024743/1-s2.0-S0378775396024743-main.pdf?%7B%5C_%7Dtid=5e55ce1c-aeb5-11e7-9776-00000aab0f02%7B%5C&%7Dacdnat=1507748145%7B%5C_%7D5d174280dcc1c2fa08f334b50afef055%20http://linkinghub.elsevier.com/retrieve/pii/S0378775396024743 (1997).

178. Serway, R. A. & Jewett, J. W. *Physics for Scientists and Engineers with Modern Physics* Ninth (Brooks/Cole Cengage Learning, Boston, MA, 2013).

179. Breitsprecher, K., Holm, C. & Kondrat, S. Charge Me Slowly, I Am in a Hurry: Optimizing Charge–Discharge Cycles in Nanoporous Supercapacitors. *ACS Nano* **12,** 9733–9741. http://pubs.acs.org/doi/10.1021/acsnano.8b04785 (Oct. 2018).

180. Largeot, C., Portet, C., Chmiola, J., Taberna, P.-L., Gogotsi, Y. & Simon, P. Relation between the Ion Size and Pore Size for an Electric Double-Layer Capacitor. *J. Am. Chem. Soc.* **130,** 2730–2731. https://pubs.acs.org/doi/10.1021/ja7106178 (Mar. 2008).

181. Jäckel, N., Rodner, M., Schreiber, A., Jeongwook, J., Zeiger, M., Aslan, M., Weingarth, D. & Presser, V. Anomalous or regular capacitance? The influence of pore size dispersity on double-layer formation. *J. Power Sources* **326,** 660–671. https://linkinghub.elsevier.com/retrieve/pii/S0378775316302166 (Sept. 2016).

182. Jiang, D., Jin, Z. & Wu, J. Oscillation of Capacitance inside Nanopores. *Nano Lett.* **11,** 5373–5377 (2011).

183. Wu, P., Huang, J., Meunier, V., Sumpter, B. G. & Qiao, R. Complex Capacitance Scaling in Ionic Liquids-Filled Nanopores. *ACS Nano* **5,** 9044–9051. http://pubs.acs.org/doi/10.1021/nn203260w (Nov. 2011).

184. Feng, G. & Cummings, P. T. Supercapacitor Capacitance Exhibits Oscillatory Behavior as a Function of Nanopore Size. *J. Phys. Chem. Lett.* **2,** 2859–2864 (2011).

185. Newsam, J. M., Treacy, M. M. J., Koetsier, W. T. & Gruyter, C. B. D. Structural Characterization of Zeolite Beta. *Proc. R. Soc. A Math. Phys. Eng. Sci.* **420,** 375–405. http://rspa.royalsocietypublishing.org/cgi/doi/10.1098/rspa.1988.0131 (Dec. 1988).

186. Kahraman, A., Morris, R. J., Laskowski, R. A. & Thornton, J. M. Shape variation in protein binding pockets and their ligands. *J. Mol. Biol.* **368,** 283–301 (2007).

187. Stank, A., Kokh, D. B., Fuller, J. C. & Wade, R. C. Protein binding pocket dynamics. *Acc. Chem. Res.* **49,** 809–815 (2016).

188. Smit, B. & Maesen, T. L. M. Towards a molecular understanding of shape selectivity. *Nature* **451,** 671–678 (2008).

189. Smit, B. & Maesen, T. L. M. Molecular simulations of zeolites: Adsorption, diffusion, and shape selectivity. *Chem. Rev.* **108,** 4125–4184 (2008).

190. Nazarian, D., Camp, J. S. & Sholl, D. S. A Comprehensive Set of High-Quality Point Charges for Simulations of Metal–Organic Frameworks. *Chem. Mater.* **28,** 785–793. http://pubs.acs.org/doi/10.1021/acs.chemmater.5b03836 (Feb. 2016).